GEOLOGICA ULTRAIECTINA

Mededeling van de
Faculteit Geowetenschappen
Universiteit Utrecht

No. 298

Constraints on thermo-chemical convection from numerical modelling and geophysical data

Joost van Summeren

Promotor: Prof. dr. R. D. van der Hilst
Earth, Atmospheric, and Planetary Sciences (EAPS)
Massachusetts Institute of Technology (MIT)
Cambridge, U.S.A.

Co-promotor: Dr. A. P. van den Berg
Faculty of Geosciences
Utrecht University
The Netherlands

Members of the dissertation committee:

Dr. H. Čížková	Faculty of Mathematics and Physics Charles University, Prague Czech Republic
Prof. dr. W. Spakman	Faculty of Geosciences Utrecht University The Netherlands
Prof. dr. J. Trampert	Faculty of Geosciences Utrecht University The Netherlands
Dr. W. van Westrenen	Faculty of Earth and Life Sciences Vrije Universiteit, Amsterdam The Netherlands
Prof. dr. D. A. Yuen	Minnesota Supercomputing Institute & Department of Geology and Geophysics University of Minnesota U.S.A.

The research described in this thesis has been supported by the
Dutch National Science Foundation (NWO) under grant VICI 865.03.001.
It was carried out at:
Faculty of Geosciences
Utrecht University
Budapestlaan 4
3584 CD Utrecht
The Netherlands
`http://www.geo.uu.nl`

Printed by Wöhrmann Print Service, Zutphen
ISBN: 978-90-5744-162-2

Constraints on thermo-chemical convection from numerical modelling and geophysical data

Begrenzingen van thermo-chemische convectie opgelegd door numerieke modellering en geofysische data

(met een samenvatting in het Nederlands)

PROEFSCHRIFT

TER VERKRIJGING VAN DE GRAAD VAN DOCTOR
AAN DE UNIVERSITEIT UTRECHT
OP GEZAG VAN DE RECTOR MAGNIFICUS, PROF. DR. J.C. STOOF,
INGEVOLGE HET BESLUIT VAN HET COLLEGE VOOR PROMOTIES
IN HET OPENBAAR TE VERDEDIGEN OP
MAANDAG 17 NOVEMBER 2008 DES OCHTENDS TE 10.30 UUR

DOOR

Johannes Rudolph Gerrit (Joost) van Summeren

GEBOREN OP 9 AUGUSTUS 1978 TE OSS

Promotor: Prof. dr. R. D. van der Hilst
Co-promotor: Dr. A. P. van den Berg

Contents

Chapter 1

Introduction

1.1 Thermo-chemical mantle convection: overview of current understanding

In modern geoscience, the debate on the style and evolution of mantle convection has been fueled by mounting evidence in support of large-scale lateral variations in the composition of Earth's deep mantle. Seismological data supports the view that material transport across the mantle transition zone is significant (Van der Hilst et al. (1997); Fukao et al. (1999); Replumaz et al. (2004)), suggesting that the upper and lower mantle are not completely isolated reservoirs. On the other hand, complete homogenisation of the entire mantle by convective overturn is argued against by geochemical data suggestive of long-lived compositionally distinct domains (e.g. Hofmann (1997); Boyet and Carlson (2005)) and seismological evidence for large-scale lateral variations in the composition of the lowermost mantle (Kennett et al. (1998); Van der Hilst and Kárason (1999); Saltzer et al. (2001); Trampert et al. (2004)). It has become increasingly difficult to integrate these observational data with models of "layered convection" and "whole mantle convection", which are end-member models characterised by (piece-wise) iso-chemical layers that are well-mixed internally by convective overturn. More successful in reconciling the observational constraints is a model of thermo-chemical convection, with large-scale lateral variation in the deep mantle imposed by compositionally distinct reservoirs (e.g. Tackley (1998); Kellogg et al. (1999)). Nevertheless, validation of the model is difficult because of uncertainties in the parameters that determine deep mantle convection.

Of several different thermo-chemical models proposed, a model with large-scale piles of heterogeneous material residing on top of the core-mantle boundary (CMB) agrees perhaps best with seismological evidence for large-scale deep mantle heterogeneity. Of particular interest are two regions in the lowermost 1000 km of the mantle below Southern Africa and the central Pacific, referred to as large low shear velocity

provinces (LLSVP). For these regions seismic tomography studies infer anomalously low shear wave velocity and high bulk sound velocity –a combination that is difficult to reconcile with a purely thermal origin (e.g. Kennett et al. (1998); Van der Hilst and Kárason (1999); Saltzer et al. (2001)). Furthermore, a positive density anomaly in these regions derived from normal mode data is suggestive of an origin other than purely thermal, perhaps compositional (Ishii and Tromp (1999, 2004)). The unsuccessful search for seismic reflections (e.g. Castle and Van der Hilst (2003)) argues against models with a globally continuous sharp interface (Wen and Anderson (1997); Anderson (2006)). However, sharp-sided, nearly vertical "walls", inferred from seismic wave travel-time offset and waveform complexity (Ni et al. (2002)) are consistent with the compositional interface of a pile-shaped structure above the CMB.

Apparant conflicts in istope systematics can be resolved by storing compositionally distinct material in the mantle. A fraction of the distinct material can entrain in convective upwellings and ascends towards the surface where it can contribute to the chemical signature of ocean island basalts (OIB), which are markedly more heterogeneous than mid oceanic ridge basalts (MORB) (Christensen and Hofmann (1994); Samuel and Farnetani (2003); Xie and Tackley (2004a)). Mass-balance estimates for the volume of a distinct domain vary between studies of different isotope systems: domain volumes as high as 50% of the entire mantle have been predicted but are not undisputed (see Lyubetskaya and Korenaga (2007) for a recent overview). Alternative mechanisms to resolve the MORB-OIB chemical systematics are more controversial. According to the transition zone water filter theory (Bercovici and Karato (2003)), incompatible elements are filtered from (MORB-source) material that slowly ascends into the low water-solubility upper mantle above 410 km by dehydration-induced partial melting, and surpressed filtering for hot upwellings explains a more enriched source for OIB. The presence of a residual melt layer gravitationally trapped at the 410 boundary predicted by the water filter theory (Leahy and Bercovici (2007)) remains controversial (Vinnik and Farra (2007)). Furthermore, depending (mainly) on the ascent velocity, upwelling material experiences different conditions of partial melting, which is expressed in the chemical signature of surface basalts. Differences in melting conditions have been proposed as a mechanism to explain the characteristic chemical signatures of MORB and OIB, but they do not replace the need for compositional source heterogeneity entirely (Ito and Mahony (2005); Standish et al. (2008)).

A deep mantle reservoir, possibly enriched in heat-producing elements, has been suggested as a way to complement Earth's heat budget (Tackley (1998); Kellogg et al. (1999); Albarède and Van der Hilst (1999)). Heat budget calculations are hampered by uncertainties in surface heat flux estimates, crustal and core radiogenic heat productivity (Pollack et al. (1993); Hofmeister and Criss (2005); Murthy et al. (2003)), and uncertainties in the composition of planetesimals that formed the proto-Earth (McDonough and Sun (1995)). Despite these uncertainties, a lower mantle composed entirely of MORB-source material depleted in heat-producing elements is unlikely,

because this would imply a high rate of secular cooling and unacceptably high temperatures in the Archaean (O'Nions and Oxburgh (1983)).

While there is increasing consensus on the presence of compositional heterogeneity in the deep mantle, many questions remain about its origin and evolution over geological time and on the amount and mode of mass transport between deep and shallow parts of the mantle. Any transport of deep mantle material to the surface must, in some form, be modulated at the mantle transition zone between around 410 and 660 *km* depth, due to solid-state phase transitions and a rheological transition (e.g. Steinbach et al. (1993); Solheim and Peltier (1993)). Seismic evidence suggests a partial degree of convective layering at the mantle transition zone ((Van der Hilst et al. (1991); Fukao et al. (1999)) which is perhaps associated with an intermittent and episodic style of material transport between the upper and lower mantle (Machetel and Weber (1991)), consistent with episodic plate tectonic reorganisation and episodic continent formation (Wilson (1966); Condie (1999); O'Neill et al. (2007)). Likewise, convective upwellings can become deflected and focused when reaching the upper mantle (e.g. Cserepes and Yuen (2000)). An indicator of deflection of compositionally heterogeneous upwellings might be large-scale compositional heterogeneity below the mantle transition zone, consistent with recent seismological data (Trampert et al. (2004)).

Clearly, knowing the degree of convective layering is essential for understanding the style of mantle convection and the way the deep mantle convective structure is expressed in the surface observables. Unfortunately, seismic imaging is difficult because of uneven data coverage (and, consequently, uneven spatial resolution by the data) and claims for a deep mantle origin of hotspots are not undisputed (Bijwaard and Spakman (1999); Nolet et al. (2007); Li et al. (2008)). Petrological evidence for a lower mantle origin of surface rocks is not conclusive either (McCammon (2001); Spengler et al. (2006)). Important information is contained in the chemical signature of basalts at spreading ridges and hotspots because it serves as a petrologic thermometer: from the chemical composition of basalts the temperature of upwellings at the depth of melting (extrapolated adiabatically to the surface) can be estimated (e.g. Green et al. (2001)). Recently, a $\sim 150-300K$ excess temperature was inferred petrologically for OIB relative to MORB (Putirka et al. (2007); Herzberg et al. (2007)). This confirms previous estimates based on the surface topography of hotspot swells (Schilling (1991)). The excess temperature of OIB is surprisingly low (when assuming a deep mantle origin) considering the high temperature contrast between the Earth's core and the surface and this requires an explanation. Several candidate mechanisms have been proposed that systematically decrease the excess temperature of convective mantle upwellings (Farnetani (1997); Bunge (2005)). However, the influence of the mantle transition zone on excess temperature has received little attention so far.

The presence of a deep mantle reservoir is also linked with the thermal evolution of the core. An outward directed CMB heat flux is required to power the geodynamo

that has existed for 3.5 *Gyr* or longer (e.g. Christensen and Tilgner (2004); Biggin et al. (2008)). On the other hand, CMB heat flux is bounded on the high side by unrealistically high core temperatures in the Archaean that correspond with fast core cooling (see Lay et al. (2008) for an overview). Reasonable scenarios for thermal core evolution favour thermal blanketing of the core, in order to decrease the CMB heat flux and slow down core cooling. An obvious way to provide thermal blanketing of the core is by a deep mantle reservoir, possibly enriched in heat producing elements (Kellogg et al. (1999); Nakagawa and Tackley (2004b)).

In connection with the thermo-chemical mantle convection models the question arises how large-scale compositionally distinct, intrinsically dense domains may have formed in the deep mantle. Several formation processes have previously been proposed and below we discuss how the processes can have operated during mantle evolution and changed the structure of mantle convection.

At present, compositionally heterogeneous material is injected in the mantle by means of subduction of oceanic basaltic crust at convergent margins (e.g. Reymer and Schubert (1984)). High-pressure experiments have shown that basaltic material is denser than the average mantle throughout the entire lower mantle, except perhaps for a restricted region just below the mantle transition zone (Irifune and Ringwood (1993); Ono et al. (2005); Perrillat et al. (2006)). Therefore, it is not unlikely that the basaltic crust sinks to the deep mantle to form a compositionally distinct reservoir (e.g. Christensen and Hofmann (1994); Van Thienen et al. (2005)). Geochemical isotope dating suggests that large-scale differentiation of the mantle occured from an early stage of mantle evolution (Smith and Ludden (1989); Blichert-Toft et al. (1999); Caro et al. (2004)). For the hot early Earth, mechanisms to return basaltic crust to the deep mantle were likely different from the present-day style of subduction, but nevertheless possible, for example through delamination of eclogite from a thick basaltic crust (Vlaar et al. (1994)) or episodic rapid sinking of large (1000 *km* scale) segments of crust (Van Thienen et al. (2005)). Addressing geochemical complexity, it has been proposed that prior to subduction early-formed basaltic crust was impregnated by accretional debris from a near-Earth orbit chemically altered by solar wind irradiation (Tolstikhin and Hofmann (2005)). Former crust is enriched in both iron and perovskite (e.g. Green and Falloon (1998)) and its seismic expression predicted from mineral physics studies roughly agrees with the results from seismic inversion studies (Trampert et al. (2004)).

Another proposed formation mechanism is chemical differentiation in the solidifying magma ocean in the early hot mantle. Isotope geochemistry data shows the possibility of early formation of basalt-rich material near the surface that has subsequently sunken to the deep mantle where it has remained largely isolated throughout Earth's evolution (e.g. Boyet and Carlson (2005)). The basalt-rich reservoir formed this way occupies an estimated 5-30% of the entire mantle volume. Early formation of a compositionally distinct reservoir in the deep Earth is also possible as shown

by recent high-pressure experiments in combination with mass balance calculations (e.g. Walter et al. (2004)). The suggested isolated reservoir occupies 10-15% of the mantle volume and is enriched in perovskite and depleted in periclase. Iron enrichment may be required to match the seismological signature and to keep the reservoir gravitationally stable. The seismic signature and the graviational stability condition of the deep mantle can also be affected by enrichment of iron from the core which is possible by chemical exchange (Knittle and Jeanloz (1991)) or material transport processes such as percolation (Poirier et al. (1998)). Because the above processes are very slow it is not likely that they can account for compositional heterogeneity on a 1000 *km* length-scale (e.g. Buffett (2000); Kanda and Stevenson (2006)).

It is not unlikely that different formation mechanisms have operated simultaneously or in substitution. The plausibility of long-term survival of an intrinsically dense reservoir in the deep lower mantle, subsequent to its formation, has been demonstrated by numerical and laboratory experiments (Kellogg et al. (1999); Davaille (1999)). Different configurations have been suggested for a compositionally distinct mantle reservoir including a global semi-continuous layer in the lowermost mantle (e.g. Kellogg et al. (1999)), large-scale piles on top of the CMB (e.g. Tackley (1998); Hansen and Yuen (2000)), isolated blobs of material dispersed throughout the lower mantle (e.g. Becker et al. (1999)), and a gradual increase with depth of the concentration of compositionally distinct material in the deep mantle (Albarède and Van der Hilst (2002)). To understand the formation processes and subsequent evolution of the Earth's mantle with the available observational data is a very challenging but, nonetheless, exciting problem in present-day Earth science.

1.2 Objectives

The objective of this thesis, in a most general sense, is to understand how the mantle has evolved as a compositionally heterogeneous entity on a time scale of the age of the Earth. We address the main objective by posing several relevant sub-questions. These questions are stated below and are associated with the present-day state of mantle convection, its evolution, and the formation processes involved, respectively.

- Can the existence of compositionally distinct domains in the present-day deep mantle be reconciled with relevant observational data such as the excess temperatures in and chemical heterogeneity of the upper mantle, the long wavelength gravity signals, and the distribution of lateral variations in seismic wave velocity? In this light, how do thermo-chemical mantle convection models compare with iso-chemical models?

- What convection parameters determine the survival of a distinct reservoir subject to convective overturn, and what are the time-scales and length-scales in-

volved with the evolution of compositional heterogeneities? What are the implications of thermo-chemical mantle convection for the predicted variability of surface basalt production and the thermal evolution of the core, which is constrained by Earth's magnetic field? How is the evolution of a deep mantle reservoir affected by the degree of convective layering at the upper-lower mantle boundary and how is this expressed in surface observables?

- Is it possible to distinguish, on the basis of seismological data, between several previously proposed processes for the formation of large-scale compositionally distinct reservoirs in the deep mantle?

The above questions will be addressed in the remainder of this thesis. The methodology of each chapter is described in more detail in the thesis outline that follows below.

1.3 Thesis outline

In Chapter 2, we explain the main physical concepts and model equations that describe thermo-chemical convection of the Earth's mantle. To study the long-term evolution of thermo-chemical mantle convection we solve the model equations numerically and perform a series of numerical modelling studies. In view of the substantial uncertainties in observational data on the deep mantle, we examine a broad range of mantle convection parameters and compare the thermo-chemical models with isochemical models throughout the thesis. For comparison with available observational data we extract synthetic data from the numerical modelling results, The main results are presented in Chapter 3, 4, and 5, in which different synthetic "observables" are addresses catagorically.

Chapter 3 deals with transport of heat and compositionally distinct material in mantle convection models. The long-term survival of a distinct reservoir in the deep mantle is investigated systematically. We account for the 660 *km* post-spinel phase transition to examine the influence of transition zone layering on reservoir survival and transport of heat and material between the deep mantle and the surface. The modelling results are compared with available observations on excess temperatures and compositional heterogeneity of ocean island basalts.

In Chapter 4, the hypothesis of a chemically heterogeneous mantle is tested by calculating synthetic gravity signals from the convection models. Long wave-length geoid anomalies are compared with available observational data.

In Chapter 5, the seismic expression is investigated of compositional anomalies of various petrological origin. To this end, the seismic properties of petrological anomalies that are inferred from the convection results are calculated by extrapolation of mineral physics data to high temperature and pressure conditions. This allows a

comparison of the seismic expression for previously proposed processes of formation of large-scale heterogeneity in the deep mantle. Synthetic shear wave and bulk sound velocity anomalies for different convection models are compared with global seismic tomography data. We account for the seismic expression associated with solid-state phase transitions near 660 *km* depth to calculate the seismic signature in the shallow lower mantle. The modelling results are also put in context with thermal evolution of the core, which is directly related to the long-term evolution of the Earth's magnetic field.

In Chapter 6, we discuss the main modelling results of this thesis, formulate the conclusions, and give recommendations for future research.

Chapter 2

General theory and numerical solution methods

In this thesis we investigate thermo-chemical mantle convection using a mathematical formulation of the fluid dynamics laws that describe material and heat transport. The governing equations are presented in Section 2.1. To solve the convection equations we use numerical techniques that are described in Section 2.2.

2.1 Physical laws governing thermo-chemical convection

The Extended-Boussinesq formulation We describe the mantle as an incompressible Newtonian fluid at infinite Prandtl number and we use the Extended-Boussinesq formulation, which allows for depth-dependent properties (e.g. Christensen and Yuen (1985); Steinbach et al. (1989); Ita and King (1994); De Smet et al. (2000)). All symbols used are listed in Table 2.1.

For the conservation of mass in an incompressible medium a divergence-free velocity field, $\vec{u}$, is described by the continuity equations. We have

$$\nabla \cdot \vec{u} = 0. \tag{2.1}$$

The conservation equation of momentum describes the convective flow velocity that depends on variations in the dynamic pressure and buoyancy forces. Because of the high mantle viscosity, inertial forces can be neglected ($Pr \rightarrow \infty$) and convective flow is laminar ($Re \ll 1$). With these assumptions, conservation of momentum is described by the Stokes equation, expressed as

$$-\nabla \Delta P + \nabla \cdot \tau = \Delta \rho \vec{g}, \tag{2.2}$$

with $\tau = \eta e = \eta \left(\nabla \vec{u} + (\nabla \vec{u})^T \right)$.

Symbol	Parameter	Value	Dimension
γ	Clapeyron slope		PaK^{-1}
$\Gamma_{ph} = \frac{1}{2}(1+\sin(\pi\frac{z-z_{ph}}{2d_{ph}}))$	Phase parameter		$-$
	$(z \in [z_{ph}-d_{ph}, z_{ph}+d_{ph}])$		
$\Gamma_{ph} = H(z-z_{ph})$	Phase parameter		$-$
	$(z \notin [z_{ph}-d_{ph}, z_{ph}+d_{ph}])$		$-$
H	Heaviside function		$-$
d_{ph}	Half-width phase transition	50	km
ΔS	Latent heat		JK^{-1}
T_{ph}	Reference temperature phase trans.	2073	K
P_{ph}	Reference pressure phase trans.	2.5×10^{10}	Pa
ΔT	Temperature scale	4000	K
$T = T_S + T'\Delta T$	Temperature		K
T_S	Surface temperature	273	K
T_c	Core temperature		K
ΔP	Dynamic pressure		Pa
t	Model time		s
ρ	Density		kgm^{-3}
ρ_0	Density scale	4500	kgm^{-3}
$\Delta\rho$	Mass density perturbation		kgm^{-3}
C	Composition parameter		$-$
c_P	Specific heat	1.25×10^{3}	$Jkg^{-1}K^{-1}$
g	Gravitational acceleration	10	ms^{-2}
g_0	Gravitational acceleration scale	10	ms^{-2}
z	Depth coordinate		m
h	Mantle depth	2.885×10^{6}	m
k	Thermal conductivity	5	$Wm^{-1}K^{-1}$
$\kappa = \frac{k}{\rho c_P}$	Thermal diffusivity	8.889×10^{-7}	m^2s^{-1}
$\Phi = \eta e^2$	Viscous dissipation function		$-$
$e_{ij} = \partial_i u_j + \partial_j u_i$	Second invariant strain rate tensor		s^{-1}
u	Convective flow velocity		ms^{-1}
$\tau_{ij} = \eta e_{ij}$	Viscous stress tensor		Pa
H_0	Initial internal heat production	17.411×10^{-12}	Wkg^{-1}
$\tau_{1/2}$	Radioactive half-life time	2.5×10^{9}	yr
$\alpha(z) = \frac{\alpha_0\Delta\alpha}{((\Delta\alpha^{1/3}-1)(1-z)+1)^3}$	Thermal expansivity		K^{-1}
α_0	Thermal expansivity scale	2×10^{-5}	K^{-1}
$\Delta\alpha$	Layer contrast thermal expansivity	0.2	$-$
$\eta(T,z) = \eta_0\exp[\ln(\Delta\eta_P)z' -$ $-\ln(\Delta\eta_T)T']$	Dynamic viscosity		Pas
η_0	Viscosity scale	5×10^{23}	Pas
$\Delta\eta_P$	Pressure related visc. contrast	20	$-$
$\Delta\eta_T$	Temperature related visc. contrast	100	$-$
Subscript	Quantity		
S	Surface		
c	Core		
CMB	Core mantle boundary		
T	Temperature		
C	Compostion		
ph	Mineral phase transition		

Table 2.1: Symbol definitions. Parameter values used in thermo-chemical modelling. Values refer to model R10 described in Chapter 4.

For heat transport we apply the following energy equation:

$$\rho_0 c_P \left(\frac{\partial T}{\partial t} + \vec{u} \cdot \nabla T \right) = \alpha(z) T \frac{dP}{dt} + \nabla \cdot (k \nabla T) + \tau : \nabla \vec{u} + \\ + \sum_{k=1}^{n_{ph}} \rho_0 T \Delta S_{L,k} \frac{d\Gamma_{ph,k}}{dt} + \rho_0 H(t). \tag{2.3}$$

Temperature changes with time (first left-hand side term) due to advection of heat (second left-hand side term) and processes described by the subsequent right-hand side terms for adiabatic heating, heat diffusion, mechanical friction, latent heat release associated with solid-state phase transitions, and radiogenic heat production.

We assume purely advective material transport, because material diffusion rates are insignificant for solid mantle rock. Consequently, we use the divergence-free conservation equation for material composition, given by

$$\frac{\partial C}{\partial t} + \vec{u} \cdot \nabla C = 0. \tag{2.4}$$

Equation of State An equation of state relates the thermodynamic properties of a material mass density, temperature, and pressure (e.g. Stacey (1992)). We use the following linearised functional expression for density variations around a thermodynamic average:

$$\rho(T,P,C) = \rho_0 + \Delta\rho \\ = \rho_0 \left[1 - \alpha(z)(T - T_S) + C \frac{\delta\rho_c}{\rho_0} + \sum_{k=1}^{n_{ph}} \Gamma_{ph,k}(T,P) \frac{\delta\rho_{ph,k}}{\rho_0} \right]. \tag{2.5}$$

The above equations illustrate that anomalies in temperature, composition, and mineral phase stability all contribute to density variations, which are the driving force behind the process of mantle convection. We use a reference density representative for the lower mantle ($\rho_0 = 4500 kgm^{-3}$).

A set of non-dimensional equations For the purpose of clarity, equations (2.1) to (2.5) are scaled to their non-dimensional form. We use scaling relations described in (Van den Berg et al. (1993))

$$\vec{x} = \vec{x}' h, \quad t = t' h^2/\kappa, \quad T - T_S = \Delta T T', \quad \Delta P = \Delta P' \frac{\eta_0 \kappa}{h^2}, \\ \tau = \tau' \frac{\eta_0 \kappa}{h^2}, \quad \vec{u} = \vec{u}' \frac{\kappa}{h}, \quad \eta = \eta' \eta_0, \quad H = H' H_0, \quad \alpha = \alpha' \alpha_0, \tag{2.6}$$

to obtain the following set of coupled PDEs (dropping the accents introduced in equation (2.6)):

$$\nabla \cdot \vec{u} = 0 \tag{2.7}$$

$$-\nabla \Delta P + \nabla \cdot \tau = \left(Ra_T \alpha(z) T - Ra_c C - Ra_{ph} \sum_{k=1}^{n_{ph}} \Gamma_{ph,k} \right) \hat{z} \tag{2.8}$$

$$\frac{\partial T}{\partial t} + \vec{u} \cdot \nabla T = Di \alpha(z) u_z (T + T_0) + \nabla^2 T + \frac{Di}{Ra_T} \Phi + \tag{2.9}$$

$$+ \sum_{k=1}^{n_{ph}} \gamma_k \frac{Ra_{ph,k}}{Ra_T} Di (T + T_0) \frac{d\Gamma_{ph,k}}{dt} + RH(t)$$

$$\frac{\partial C}{\partial t} + (\vec{u} \cdot \nabla) C = 0. \tag{2.10}$$

Expressions for the non-dimensional numbers are given in Table 2.2.

Solid state phase transitions Solid-state phase transitions can have a large influence on mantle convective flow (see also equation (2.5)). Particular assumptions on mantle petrology associated with these phase transitions are explained in Chapters 3 and 5. The influence of the phase transition on convective flow is represented by the phase buoyancy number $P = \frac{\gamma \delta \rho_{ph}}{\rho^2 \alpha_0 g_0 h}$ (Christensen and Yuen (1985); Tackley (1995); Bunge et al. (1997)). Phase transformations in our model are descibed by the phase parameter function, Γ_{ph}, as follows

$$\Gamma_{ph}(T,P) = \begin{cases} \frac{1}{2}\left[1 + \sin(\pi \frac{z - z_{ph}(T,P)}{2 d_{ph}})\right], & z \in \left[z_{ph} - d_{ph}, z_{ph} + d_{ph}\right] \\ H(z - z_{ph}), & z \notin \left[z_{ph} - d_{ph}, z_{ph} + d_{ph}\right] \end{cases} \tag{2.11}$$

with H the Heaviside function. The phase transforms over a depth interval of finite half-width, $d_{ph} = 50\ km$. The applied transition width is finite for numerical reasons, with the sharpness limited by the numerical mesh resolution. The phase transformation is further described by the Clapeyron slope, $\gamma = \frac{dP}{dT}$, which is fixed at a reference temperature and pressure T_{0ph}, P_{0ph}. Exothermic phase transitions ($\gamma < 0$) induce convective layering while endothermic phase transitions ($\gamma > 0$) enhance the convective flow (e.g. Christensen and Yuen (1985)). The depth of the phase transition, z_{ph}, is located at the crossing point of the geotherm and the Clapeyron curve.

Symbol	Parameter	Value	Dimension
$Ra_T = \frac{\rho_0 \alpha_0 g \Delta T h^3}{\kappa_0 \eta_0}$	Rayleigh number		–
$Ra_C = \frac{\delta \rho_C g h^3}{\eta_0 \kappa_0}$	Compositional Rayleigh number		–
$Ra_{ph} = \frac{\delta \rho_{ph} g h^3}{\eta_0 \kappa_0}$	Phase Rayleigh number	2.47×10^8	–
$Di = \frac{\alpha_0 g h}{c_P}$	Dissipation number	0.46	–
$R = \frac{H_0 h^2}{c_P \kappa_0 \Delta T}$	Internal heating number	30.89	–
$H(t) = H_0 \exp(\frac{-t \ln 2}{\tau_{1/2}})$	Time-dependent internal heating		Wkg^{-1}
H_0	Initial internal heat production	17.411×10^{-12}	Wkg^{-1}
$\tau_{1/2}$	Radioactive half-life time	2.5×10^9	yr

Table 2.2: Definition of dimensionless parameters. Values are reference initial conditions (model R10, Chapter 4).

Thermal expansivity Based on mineral physics data (e.g. Chopelas and Boehler (1992)) we use a parameterisation of the thermal expansivity that decreases with increasing pressure (see equation (2.5)). Temperature-dependence of the thermal expansivity is not included because it has a weak influence on deep mantle convection processes (Schmeling et al. (2003)). We use the following third-order parameterisation

$$\alpha(z) = \frac{\alpha_0 \Delta\alpha}{\left[(\Delta\alpha^{1/3} - 1)(1-z) + 1\right]^3} \tag{2.12}$$

with the thermal expansivity decreasing with depth by a factor of 5 across the mantle ($\alpha_0 = 2 \times 10^{-5}$, $\Delta\alpha = 0.2$). Figure 2.1e shows the depth profile for this parameterisation, which is used throughout this thesis.

Rheological model We assume viscous flow in the mantle to be governed by diffusion creep, which is the predominant process at relatively low stress levels in the hot lower mantle (e.g. Van den Berg and Yuen (1996); Ranalli (2001)).

Elasticity is neglected, because it affects only the uppermost part of the crust and is insignificant for large-scale convection processes. We use the following exponential function for temperature and pressure:

$$\eta(T,z) = \eta_0 \exp\left[-\ln\Delta(\eta_T)T + \ln\Delta(\eta_P)z\right]. \tag{2.13}$$

Figure 2.1f shows the viscosity profile ($\Delta\eta_T = 100$, $\Delta\eta_P = 20$, $\Delta\eta_C = 0$) for a typical initial temperature distribution shown in frame b. The combination of cold, high viscous surface plates overlying a low-viscosity zone mimics the rigid lithospheric plates at Earth's surface on top of a weak athenosphere.

Model domain We solve the convection equations on a 2-D model domain of cylindrical geometry with a 180^o opening angle. Although 3-D spherical models represent mantle geometry best, the demands on computation time and data storage limits the complexity of the problems that can be solved (Tackley (1998); Bunge (2005); Zhong (2006)).

In models of cylindrical geometry problems are avoided concerning unphysical effects at the poles of the domain that affect models of 2.5-D axi-symmetric geometry (Zebib et al. (1983)). In contrast to models of cartesian geometry, models of cylindrical geometry can approximate 3-D spherical heat flux and stress distribution, provided the inner and outer boundary surface radii are scaled appropriately (Jarvis (1995)).

To mimic the surface-volume characteristics of a 3-D sphere, which controls the thermal evolution, we adopt a geometrical scaling. Scaling of the inner-to-outer surface ratio is required to calculate the heat production and heat flow appropriately in a mantle that is heated from below (Van Keken (2001)). To this end, we rescale the mantle by applying non-dimensional values of 0.43 and 1.43 for the inner and outer mantle radii, respectively (see Chapter 3 for a slightly different parameterisation).

Boundary and initial conditions To investigate the transient character of mantle convection, we use a $4.5 Gyr$ time window, similar to the time span of the Earth since its formation. Thus, initial conditions in the forward model concern the Hadean mantle, after solidification of the magma ocean. We acknowledge the large uncertainties for early mantle conditions (e.g. Abe (1996)). Initial model conditions are, therefore, chosen pragmatically, in such a way that the mantle and core temperature and heat flux after a model time of 4.5 *Gyr* fall within the range of uncertainties for present-day values (e.g. Van Thienen et al. (2004); Hofmeister and Criss (2005)).

For mechanical boundary conditions we prescribe free slip, impermeable conditions on all boundaries. To the side boundaries we apply reflecting temperature conditions. The surface temperature is kept constant at $273K$ and the core temperature is initially put to $T_c = 4273K$ in most models. For the initial temperature we apply an adiabatic depth profile of potential temperature, T_P, truncated at the top and bottom boundary layers (see Figure 2.1b).

Heat exchange with the core is described by a thermal core coupling model as described in Van den Berg et al. (2005)). This allows for the monitoring of the evolution of core temperature and CMB heat flux. In this model, the mantle exchanges heat with an isothermal heat reservoir of the core. The uniform core temperature, T_c, is updated at every time-step of the finite element calculation to obtain a time-dependent boundary condition for the bottom boundary of the mantle. The core temperature is controlled by the average heat-flow from the core-mantle boundary, q_{CMB}, described

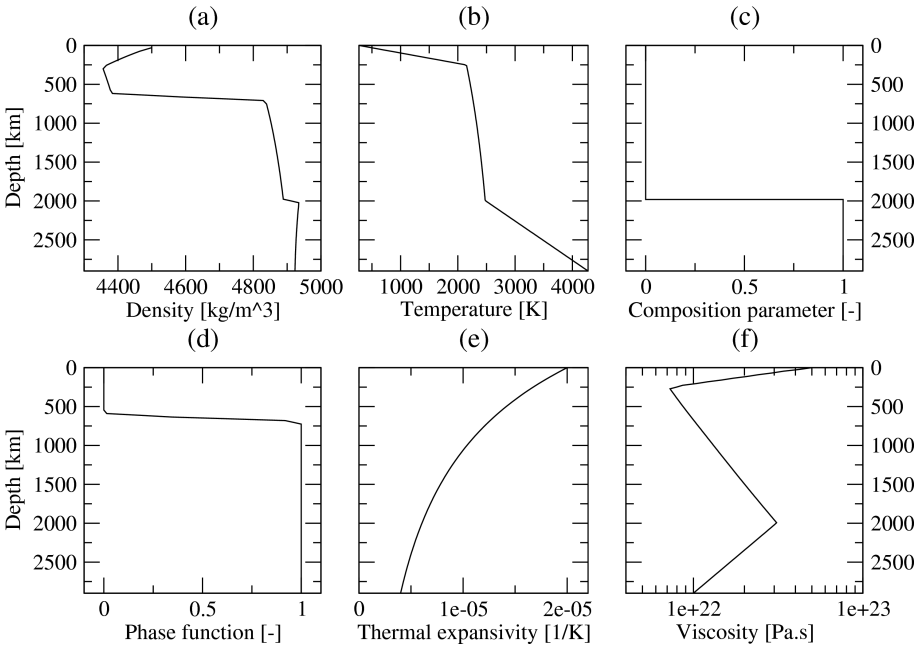

Figure 2.1: Initial condition fields. Shown are radial profiles for (a) mass density, ρ, (b) temperature, T, showing a truncated mantle adiabat, (c) compostion parameter, C, showing the placement of a deep mantle reservoir, (d) phase function, Γ_{ph}, showing the mineral phase transition near 660 *km* depth, (e) thermal expansivity, α, and (f) viscosity, η.

by (e.g. Steinbach et al. (1993)):

$$\frac{dT_c}{dt} = \frac{-A_{CMB}}{\rho_c c_{Pc} V_c} q_{CMB}(t), \tag{2.14}$$

with A_{CMB} the CMB boundary surface area, and $C_c = \rho_c c_{Pc} V_c$ the total heat capacity of the core. The core heat capacity is expressed as a fraction X of the mantle heat capacity $C_m = \rho c_P V_m$ so that equation (2.14) becomes:

$$\frac{dT_c}{dt} = \frac{-1}{X \rho c_P h} q_{CMB}(t), \tag{2.15}$$

with ρ and c_P the mantle values of density and heat capacity.

Typical initial conditions are shown in Figure 2.1. A compositionally distinct reservoir is initially placed at the bottom 20 vol% of the mantle in most cases (frame c). Compared to the overlying (background) mantle, this reservoir is characterised by an anomalous (excess) density $\delta\rho_C/\rho_0$ which is 1% in Figure 2.1c. Frame a shows the density profile that is prescribed by equation (2.5). Gradual density changes with

depth are associated with changes in temperature as shown by the profile in frame b. A sharp density increase is associated with the phase transformation at 660 *km* depth (frame d). A value of $\frac{\delta\rho_{ph}}{\rho_0} = 10\%$ is consistent with seismological and mineral physics data (e.g. Dziewonski and Anderson (1981); Hirose (2002)). The density increases by $\frac{\delta\rho_C}{\rho_0} = 1\%$ at the compositional interface near 2000 *km* depth (frame c). Mantle viscosity (frame f) sharply decreases between 0 to 300 *km* which reflects the thermal boundary layer at the surface (frame b). Below $\sim$ 2000 *km* the viscosity decreases with depth because of the temperature increase in the deep mantle (frame b). Between $\sim$ 300 - 2000 *km* pressure effects dominate and the viscosity gradually increases with depth.

2.2 Numerical solution techniques

2.2.1 The Finite Element Method

The equations 2.7 to 2.10 form a coupled set of non-linear partial differential equations (PDEs). Although analytical solution of the equations is possible for very simple convection problems, more complex problems require numerical solution techniques. To solve the advection-diffusion equations (2.7)-(2.9) we use the Finite Element Method (FEM) (e.g. Cuvelier et al. (1986); Hughes (1987); Vreugdenhil and Koren (1993)). An important advantage of the FEM over other numerical solution techniques (finite difference, spectral) is the flexibility in modelling domains of arbitrary shape. Our convection code is based on the general purpose finite element package SEPRAN (Segal and Praagman (2000)).

The finite element mesh on which we solve the convection equations is an 2-D cylindrical shell of opening angle 180^o. The mesh is equidistant in the angular and radial coordinates with a lateral-radial resolution of 256 x 64 quadrilateral cells. Each cell is divided into two quadratic six-node Crouzeix-Raviart elements for solving the velocity field (Cuvelier et al. (1986)). Temperature calculation (equation 2.16) is performed on three-node linear elements –subdivided from the above quadratic elements and defined on the same set of nodal points (Van den Berg et al. (1993)). The resulting nodal point resolution is between 5 and 23 *km*, with a higher resolution in the bottom region of the mantle.

To calculate the temperature field, we discretise the energy equation (2.9) using the standard Galerkin approach, which is based on the weak formulation of diffusion-advection equations (Segal (1993)). The resulting set of discrete ordinary differential equations (ODEs) are assembled in a matrix-vector system, written as

$$M\dot{\vec{T}} + S\vec{T} = \vec{R}, \tag{2.16}$$

with mass matrix M, stifness matrix S, and right-hand side vector $\vec{R}$ (see Cuvelier et al. (1986); Hughes (1987) for a detailed description). The temperature values defined at

discrete finite element nodal points are contained in vector $\vec{T}$, and time derivative of the temperature values are in vector $\dot{\vec{T}}$.

Equations for conservation of mass (2.7) and momentum (2.8) are solved simultaneously. To avoid numerical problems in the direct solution of the coupled equations, a perturbation term containing the pressure is added to the continuity equation (2.8). This so-called penalty function formulation (Cuvelier et al. (1986); Hughes (1987)) results in a set of algebraic equations that in matrix-vector notation is written as

$$S\vec{U} - L^T\vec{P} = \vec{F} \qquad \text{Conservation of momentum} \tag{2.17}$$

$$\vec{P} = \frac{-1}{\varepsilon} M_P^{-1} L\vec{U} \qquad \text{Conservation of mass} \tag{2.18}$$

M_P is the pressure mass matrix, and $\varepsilon = 10^{-9}$ is the penalty function parameter. The above equation (2.17) is solved using a direct linear algebraic equation solver (Van den Berg et al. (1993)).

We calculate the time-dependent fields by solution of the coupled equations (2.16) and (2.17), using a Predictor-Corrector scheme described in Van den Berg et al. (1993), i.e. a first order accurate, implicit Euler predictor and second order accurate, Crank-Nicolson corrector. Time-steps in the integration are calculated using a Courant-Friedrichs-Levy criterion (Vreugdenhil and Koren (1993)). Time steps are multiplied by a factor 0.01-0.5.

2.2.2 The particle tracer method

To solve for diffusion-free material transport (equation 2.10) an approximate version containing a small diffusion term to suppress non-physical oscillations is sometimes used in a so-called field approach (Van Keken et al. (1997); Hansen and Yuen (2000); Čížková and Matyska (2004)). However, this method becomes impractical for long integration times and small-scale structure of the composition field because of the accumulating effects of artificial diffusion. Material transport is more efficiently solved using a Langrangian framework. Best suited for our purpose is the Particle-in-Cell (PiC) tracer method (e.g. Hockney and Eastwood (1988)). With PiC interpolation, the particle tracer field is interpolated to the finite element mesh, which involves two steps: (i) projection of particle tracer field values to the grid points of an equidistant structured mesh, and (ii) interpolation from the 4 surrounding grid points of the structured mesh to a finite element Gauss point. In both steps we use area-weighted interpolation. The PiC method can resolve compositional contrasts narrower than the finite element grid spacing. Furthermore, it solves without problem for topologically complex compositional interfaces that are typical for long-term convection models. For complex compositional interfaces, the alternative Lagrangian method of marker chains becomes unfeasible (e.g. Van Keken et al. (1997); Ten et al. (1997)).

Particle tracers are randomly distributed over the model domain in the initial condition. As a compromise between resolution and numerical demands we use 1.2 million particle tracers on which the composition field is defined. Particle tracers are advected with the convective flow using a 4th order Runge-Kutta scheme. In this thesis, physical quantities that depend on composition (Eq. 2.5) are density and the internal heating rate (Section 3.3.1). To monitor solution fields in the Lagrangian framework, we use monitor particle tracers that are advected passively with the convective flow. This way, field values such as temperature, velocity components, and spatial coordinates are evaluated and stored at the monitor tracer positions at every integration time step.

Chapter 3

Upwellings from a deep mantle reservoir filtered at the 660 km phase transition in thermo-chemical convection models and implications for intra-plate volcanism[1]

Abstract

With numerical modelling experiments we examine the influence of the 660 *km* post-spinel phase transition on the excess temperatures in and transport of compositional heterogeneity by deep mantle upwellings. We test our results against available observations on ocean island basalts (OIB). The endothermic post-spinel transition can cause localised, transient layering of convective flow in the upper mantle transition zone. Upwellings from the lower mantle, in our models the passive (mechanically-driven) return flow from active (buoyancy-driven) downwellings, can transport heterogeneous material from deep mantle reservoirs across the transition zone into the upper mantle, but the phase transition can act as a chemical filter that can (locally) retain intrinsically denser elements in the lower mantle. A compositionally hetero-

[1]The material presented in this chapter has been accepted for publication in the journal Physics of the Earth and Planetary Interiors as: Van Summeren, J. R. G., Van den Berg, A. P., and Van der Hilst, R. D., Upwellings from a deep mantle reservoir filtered at the 660 km phase transition in thermo-chemical convection models and implications for intra-plate volcanism, *Phys. Earth Planet. Int.* (2008), doi:10.1016/j.pepi.2008.09.011

geneous signature in upwellings from the lower mantle (e.g. Hofmann, A.W., 1997. Mantle geochemistry: the message from oceanic volcanism. Nature 385, 219-229) that is consistent with chemical diversity in OIB can be produced for a wide range of mantle evolution scenarios and stability conditions of compositional heterogeneity in the lower mantle. We demonstrate that the excess temperature in upwellings crossing the phase boundary increases with the background temperature contrast across the endothermic phase transformation, which itself increases with the degree of convective layering. For cases with a low degree of layering at the transition zone, the combination of upwellings of mid-mantle origin and intrinsically hot, deep-seated upwellings produce model results consistent with the formation of hotspots and large igneous provinces (LIP) at the surface. For high degrees of convective layering, however, lower mantle upwellings of high excess temperature would generate (with high frequency) massive flood basalt events. In view of the strong influence of transition zone convective layering on excess temperatures, the observed intra-plate volcanism in modern Earth suggests that on a global scale the degree of layering at the transition zone is low. This requires a low Clapeyron slope magnitude of the post-spinel phase transition. Because hot intrinsically dense material residing below the phase transition favours a high degree of convective layering, the Clapeyron slope magnitude must be even lower for this case in order to produce results consistent with inferences from mantle petrology.

3.1 Introduction

The scale and nature of convective upwelling relates to two long-standing, unresolved questions in mantle dynamics: the origin of intra-plate volcanism and the degree of convective layering at the transition zone. There is no consensus on whether intra-plate volcanism, such as large igneous provinces (LIP), hotspots, and seamounts have their origin in the upper or lower mantle (e.g. Campbell (2007)). Seismological evidence for the origin of mantle upwellings underneath hotspots is still ambiguous (e.g. Bijwaard and Spakman (1999); Nataf (2000); Nolet et al. (2006); Anderson (2006)).

If upwellings rising from the lower mantle are responsible for intra-plate volcanism, they must be consistent with surface observables. Isotope and trace-element geochemistry shows a heterogeneous chemical signature in ocean island basalts (OIB) compared to the more homogeneous mid-oceanic ridge basalts (MORB) (e.g. Hofmann (1997)). Thermo-chemical mantle convection (e.g. Christensen and Hofmann (1994); Kellogg et al. (1999); Samuel and Farnetani (2003); Xie and Tackley (2004a); Tan and Gurnis (2007)) provides a mechanism for producing OIB-like chemical signatures by assuming entrainment of chemically distinct material from largely isolated lower mantle reservoirs. Apart from geochemical arguments, the existence of compositionally distinct reservoirs in the deep mantle is supported by seismological evi-

dence (e.g. Van der Hilst and Kárason (1999); Ishii and Tromp (1999); Saltzer et al. (2001, 2004); Trampert and van der Hilst (2005); Deschamps et al. (2007); Kellogg et al. (2007)). Furthermore, the precence of a significant percentage of Earth's heat-producing elements in compositionally distinct material stored in a deep reservoir can resolve apparant conflicts in Earth's heat budget and istope systematics (e.g. Kellogg et al. (1999); Tolstikhin and Hofmann (2005); Tolstikhin et al. (2006)). An increase of the radiogenic heat production rate is expected when basaltic material associated with former subducted crust is concentrated in a compositionally distinct reservoir (e.g. Christensen and Hofmann (1994); Kellogg et al. (1999); Nakagawa and Tackley (2004c); Van Thienen et al. (2005)).

Upwellings that cause intra-plate volcanism also put constraints on excess temperature. The potential mantle temperatures (i.e. the temperature extrapolated to the surface along a mantle adiabat) can be inferred from the melting conditions of intra-plate volcanism caused by upwellings, which –in turn– are constrained by basalt geochemistry. An excess of 150-300K of the potential temperature is estimated for intra-plate volcanism in comparison to MORB (e.g. Schilling (1991); Putirka et al. (2007); Herzberg et al. (2007)). Much larger excess temperatures would be expected, however, in upwellings originating from the core mantle boundary (CMB), for which a temperature contrast exceeding $1000K$ is inferred (e.g. Boehler (2000); Van der Hilst et al. (2007)). It has been argued that a relatively small amount of cooling of mantle upwellings results from heat diffusion, adiabatic decompression, and thermal entrainment of surrounding (colder) mantle material (see e.g. Farnetani (1997)). Therefore, mechanisms must exist to lower the excess temperatures to sufficiently small values. Candidate mechanisms are upwellings originating at the top of a thermo-chemical boundary layer (Farnetani (1997)) and a sub-adiabatic temperature profile related to internal heating (Jeanloz and Morris (1987); Bunge (2005); Zhong (2006)).

The thermal evolution of mantle upwellings is influenced by the degree of mantle flow layering at the mantle transition zone between 410 and 660 km depth. Important dynamical implications are expected from the spinel→perovskite + magnesiowüstite transition around 660 km depth, which is associated with a density increase of around 8-10% (Dziewonski and Anderson (1981); Hirose (2002)) and a Clapeyron slope γ around -1 to $-3MPaK^{-1}$ (e.g. Ito and Takahashi (1989); Weidner and Wang (1998); Hirose (2002); Fei et al. (2004); Jacobs and de Jong (2007)). The endothermic phase transition acts as a barrier to convective flow (Olson and Yuen (1982)). The conditions for convective layering at the endothermic phase transition are expressed by the critical value for the dimensionless phase buoyancy parameter P, which depends linearly on the Clapeyron slope γ (see Table 3.1 for definition). Christensen and Yuen (1984, 1985) and Nakakuki et al. (1994) determined a critical value of around $P_{crit} = -0.25$, which corresponds to a Clapeyron slope of $-3MPaK^{-1}$ in our models. Around the critical value, local intermittent mixing between the upper and the lower mantle emerges, with alternating periods of layered and whole mantle convection (e.g.

Machetel and Weber (1991)).

A partial barrier is compatible with seismological evidence showing that some subducting slabs and mantle upwellings cross the transition zone seemingly undisturbed, but perhaps with advective thickening (Fischer et al. (1988); Ribe et al. (2007)), whereas others are deflected at this boundary (e.g. Van der Hilst et al. (1991, 1997); Fukao et al. (1999); Nolet et al. (2006)). Although the resolution of structure associated with mantle upwelling is lower than for downwellings, a similar partial layering of upwellings is in agreement with seismological data. Recent studies suggest a large global variation in the connectivity of seismic velocity anomalies across the mantle transition zone, where a deep mantle origin has been suggested for only a part of the hotspot regions (e.g. Bijwaard and Spakman (1999); Nolet et al. (2006, 2007); Zhao (2007)).

Weinstein (1992) demonstrated that the endothermic phase transition can filter mantle upwellings chemically, by preferentially restricting intrinsically dense material to the lower mantle, thereby inducing a compositional contrast across the phase transition. Similar chemical filtering affects downwellings, e.g. by separating the harzburgitic and basaltic fractions of a subducting slab (e.g. Mambole and Fleitout (2002)). For a pyrolite composition a density cross-over is inferred at the base of the mantle transition zone (Irifune and Ringwood (1993); Ono et al. (2001)), which induces chemical stratification –with harzburgite underlying MORB material– that contributes to convective layering at the phase transition (Irifune and Ringwood (1993); Van Keken et al. (1996); Xie and Tackley (2004a); Nakagawa and Buffett (2005)). Without the effects of phase transitions, the critical density contrast for two-layer flow is estimated at 1-3% between the upper and lower mantle (Christensen (1989); Kellogg (1991); Nakakuki et al. (1994)).

Clearly, the post-spinel phase transition is critical in controlling material exchange between the upper and lower mantle. Unfortunately however, the degree of convective layering is not fully constrained. The emphasis of previous work has been on investigating conditions for convective layering in relation to the endothermic post-spinel phase boundary and the influence of a compositional density contrast. In the present study the objective is to constrain the conditions under which upwellings from the deep mantle show Earth-like characteristics. We investigate the transport characteristics of thermo-chemical upwellings associated with a compositionally distinct reservoir in the lower mantle, and we test model predictions against observed intra-plate volcanism (notably ocean-island basalts). Specifically, we analyse the thermal and compositional expression of material entering the upper mantle from below along with constraints from mantle petrology. We focus on models that exhibit weak layering due to the 660 km phase boundary, in line with observational evidence and include Clapeyron slope values ranging from -1.25 to -2.5 $MPaK^{-1}$, in line with current petrological uncertainties. As far as we are aware, the influence of the post-spinel phase transition on increasing the excess temperature of upwellings has not been systemat-

ically investigated before. We show that upwellings of lower mantle origin are compositionally heterogeneous for a large range of possible thermo-chemical convection scenarios (e.g. Kellogg et al. (1999); Becker et al. (1999); Hansen and Yuen (2000); Tackley (2002)) and that excess temperatures in upwellings correpond to petrological estimates for specific degrees of convective layering and stability of a compositionally distinct deep mantle reservoir.

3.2 Methods used in numerical modelling

We examine thermo-chemical mantle convection through numerical experiments that simulate an incompressible linearly viscous fluid at infinite Prandtl number. For the numerical convection model, we use the following extended-Boussinesq formulation (e.g. Christensen and Yuen (1985); Steinbach et al. (1989); Ita and King (1994)):

$$\partial_j u_j = 0 \tag{3.1}$$

$$-\partial_i \Delta P + \partial_j \tau_{ij} = \left(\alpha(z) Ra T - Rb_{ph}\Gamma_{ph} - Rb_C C\right)\delta_{i3} \tag{3.2}$$

$$\tau_{ij} = \eta(T,P)\left(\partial_j u_i + \partial_i u_j\right) \tag{3.3}$$

$$\frac{DT}{Dt} = \partial_j\partial_j T + \alpha(z) Di u_z (T+T_0) + \tag{3.4}$$

$$+\gamma \frac{Rb_{ph}}{Ra} Di \frac{D\Gamma_{ph}}{Dt}(T+T_0) + \frac{Di}{Ra}\Phi + RH(t)$$

$$\frac{DC}{Dt} = \frac{\partial C}{\partial t} + u_j \partial_j C = 0. \tag{3.5}$$

Symbols used are explained in Table 3.1. Mass conservation of the incompressible fluid model is expressed in the continuity equation (3.1). The Stokes equation (3.2) describes the conservation of momentum, assuming an infinite Prandtl number. The constitutive equation (3.3) defines a linear viscous rheology dependent on temperature and pressure. The energy equation (3.4) describes heat transport, where the right-hand side terms are for heat diffusion, adiabatic heating, latent heat of the phase transition, viscous dissipation, and radiogenic internal heating, respectively. The advection equation for composition (3.5) describes transport of compositional heterogeneities by means of convective flow –diffusion of material is excluded. In our models, thermal expansion decreases with increasing pressure, which stabilises dense heterogeneous material at the bottom of the mantle and which reduces the critical density contrast for stability of such heterogeneities (Hansen and Yuen (2000)).

Symbol	Property	Value	Dimension
γ	Clapeyron slope		$MPaK^{-1}$
Γ_{ph}	Phase parameter		$-$
d_{ph}	Phase transition halfwidth	50	km
$\frac{\delta\rho_{ph}}{\rho_0}$	Phase density contrast	0.1	$-$
T_{ph}	Reference temperature phase transition	2073	K
P_{ph}	Reference pressure phase transition	2.97×10^{10}	Pa
C	Composition parameter		$-$
$\frac{\delta\rho_C}{\rho_0}$	Compositional density contrast		$-$
ΔT	Temperature scale	3727	K
T	In situ temperature		K
T_S	Surface temperature	273	K
T^0_{CMB}	Initial core temperature	4000	K
T_{bg}	Background temperature		K
$T_{ex} = T - T_{bg}$	Excess temperature		K
t	Model time		s
ρ	Density		kgm^{-3}
ρ_0	Density scale	4500	kgm^{-3}
ΔP	Dynamic pressure		Pa
c_P	Specific heat	1.25×10^3	$Jkg^{-1}K^{-1}$
g	Gravitational acceleration	10	ms^{-2}
h	Mantle depth	2.9×10^6	m
k	Thermal conductivity	5	$Wm^{-1}K^{-1}$
$\kappa = \frac{k}{\rho c_P}$	Thermal diffusivity		m^2s^{-1}
$\Phi = \eta e^2$	Viscous dissipation function		$-$
$e = (\frac{1}{2}e_{ij}e_{ij})^{1/2}$	Second invariant strain rate tensor		s^{-1}
u	Convective flow velocity		ms^{-1}
$\tau = \eta e_{ij}$	Viscous stress tensor		Pa
$Ra = \frac{\rho_0\alpha_0 g\Delta T h^3}{\kappa_0\eta_0}$	Rayleigh number	1.9×10^8	$-$
$Rb_C = \frac{\delta\rho_C g h^3}{\eta_0\kappa_0}$	Compositional Rayleigh number		$-$
$Rb_{ph} = \frac{\delta\rho_{ph} g h^3}{\eta_0\kappa_0}$	Phase Rayleigh number	2.47×10^8	$-$
$Di = \frac{\alpha_0 g h}{c_P}$	Dissipation number	0.46	$-$
$R = \frac{H_0 h^2}{c_P\kappa_0\Delta T}$	Internal heating number	32.9	$-$
$H(t) = H_0 exp(\frac{-\ln(2)t}{\tau_{1/2}})$	Time-dependent internal heating		Wkg^{-1}
H_0	Initial internal heat production	17.411×10^{-12}	Wkg^{-1}
$\tau_{1/2}$	Radioactive half-life time	2.5×10^9	yr
$P = \frac{\gamma\delta\rho_{ph}}{\rho_0^2\alpha_0 g_0 h}$	Phase boundary buoyancy parameter		$-$
$B = \frac{\delta\rho_C}{\rho_0\alpha_0\Delta T}$	Compositional buoyancy number		$-$
$\alpha(z)$	Thermal expansivity		K^{-1}
α_0	Thermal expansivity scale	2×10^{-5}	K^{-1}
$\Delta\alpha$	Thermal expansivity contrast	0.2	$-$
$\eta(T,z)$	Dynamic viscosity		Pas
η_0	Viscosity scale	5×10^{20}	Pas
$\Delta\eta_P$	Pressure related viscosity contrast	20	$-$
$\Delta\eta_T$	Temperature related viscosity contrast	100	$-$
M_{tot}	Total mass transport rate		s^{-1}
M_{het}	Heterogeneous mass transport rate		s^{-1}
f_{het}	Fractional heterogeneity of mass transport		$-$

Table 3.1: Symbol definitions and parameter values.

In our models, buoyancy variations that drive convection depend on variations in temperature, mineral phase, and chemical composition, as described by the following equation of state:

$$\rho = \rho_0 \left(1 - \alpha(z)(T - T_S) + \Gamma_{ph} \frac{\delta\rho_{ph}}{\rho_0} + C \frac{\delta\rho_C}{\rho_0} \right). \tag{3.6}$$

The convection equations 3.1-3.6 are solved using the SEPRAN finite element package (Van den Berg et al. (1993); Segal and Praagman (2000)). In order to model the non-diffusive composition field, 1.2 million active particle tracers are advected with the convective flow using a 4^{th}-order Runge-Kutta scheme. The tracers are used in a particle-in-cell interpolation (Hockney and Eastwood (1988)) in the evaluation of composition-dependent quantities, such as compositional density contrasts. We use a two-dimensional cylindrical shell of 180 degrees opening angle with a nodal point resolution between 5 and 23 km. A geometrical scaling of the mantle domain mimics the surface-volume characteristics of a 3-D sphere that control the thermal evolution. Van Keken (2001) demonstrated that scaling of the inner-to-outer surface ratio is required to calculate the heat production and heat flow appropriately in a mantle that is heated from below. Because the mantle model that we consider is primarily heated from within, it is appropriate to rescale the volume-to-surface ratio for the cylindrical model, such that it approximates that of the spherical Earth. To this end, the inner and outer radii of the mantle are given the dimensionless values 0.3 and 1.3, respectively. A time window of $4.5Gyr$ allows us to study the long-term evolution of Earth's mantle. We use time-dependent radio-active internal heating that decays with a half-life time of $2.5Gyr$ to an approximately chondritic value of $5 \times 10^{-12} Wkg^{-1}$ at the end of the model time of $4.5Gyr$. Internal heating is uniformly distributed across the mantle in all cases except for model H10 in which heat production is concentrated in the compositionally distinct mantle.

Free slip, impermeable boundary conditions are prescribed on all sides, and reflecting temperature conditions are applied to the side boundaries. For the initial temperature we apply an adiabatic depth profile of potential temperature $T_P = 1960K$, truncated at the top and bottom boundary layers. The surface temperature is kept constant at $273K$ and the core temperature is put to $4000K$ initially, and varies in time as a result of thermal coupling with a heat reservoir representing the core, as described in Van den Berg et al. (2005). A chemically dense reservoir is initially placed at the bottom 35 vol% of the mantle. Within this initial layer configuration the excess density varies linearly with the composition parameter C from zero at the top to a maximum value $\delta\rho_C/\rho_0$ at the bottom.

To model the solid-state post-spinel phase transition we use a negative Clapeyron slope γ and a density contrast of $\delta\rho_{ph}/\rho_0 = 10\%$; both parameters promote convective layering at the phase transition (e.g. Turcotte and Schubert (2002)). For numerical reasons the halfwidth of the phase transformation is set to 50 km. We focus on

the influence of the post-spinel phase transition and disregarded other phase transformations in the mantle. Numerical modelling (e.g. Solheim and Peltier (1993)) has demonstrated, however, that convective layering at the endothermic phase transition and the corresponding development of a thermal boundary reduces as a results of nearby exothermic phase changes (e.g. olivine→ spinel near 410 *km* depth, ilmenite→perovskite near 660 *km*, and garnet-majorite to perovskite near 700 *km* in a mantle of pyrolite composition (e.g. Weidner and Wang (1998))).

Viscosity varies exponentially with temperature and pressure by a factor of 100 and 20, respectively, in our model. Temperature-dependent viscosity tends to increase the propensity to layering and to focus upwellings in a low-viscosity zone underneath the phase transition (Steinbach and Yuen (1995)). A viscosity increasing with depth tends to stagnate and broaden the convective flow in the deep mantle (e.g. Hansen et al. (1993)). The thermal expansivity across the mantle's depth range decreases by a factor of 5 across the mantle (Chopelas and Boehler (1992); Steinbach and Yuen (1994)), which reduces the (positive) thermal buoyancy for a given temperature anomaly. A list of model parameters is given in Table 3.1 and 3.2 including values for γ and $\delta\rho_C/\rho_0$ that are used as control parameters in the experiments. Effective dimensionless parameters for the phase buoyancy $P_e = \gamma\delta\rho_{ph}/\left(\rho_0^2\langle\alpha\rangle g_0 h\right)$ and compositional buoyancy $B_e = \delta\rho_C/\left(\rho_0\langle\alpha\rangle\Delta T\right)$ are given for the initial condition, where the terms between $\langle\rangle$-brackets are average mantle values. The initial effective Rayleigh number is $Ra_e = 4\times10^6$.

3.2.1 Description of mass transport and excess temperature diagnostic

In order to monitor the thermal and chemical characteristics of upwellings at the post-spinel phase transition we use diagnostics based on passive particle tracers that are defined in addition to the set of active particle tracers mentioned above. A total of $2,000$ randomly distributed passive monitor tracers were used to monitor the local space coordinates, composition, and temperature at every integration time step of the model equations. The monitor data were used to analyse the impact of several model parameters on the transport of compositionally distinct reservoir material from the lower mantle into the upper mantle. Monitor tracers are diagnosed at 18 *km* above and below the phase transition. Within this depth range the phase parameter changes value from $\Gamma_{ph} = .05$ to $.95$. Monitor tracers in mantle upwellings that cross the observation depths above and below the phase transition are labeled with the superscripts 'um' and 'lm', respectively.

Using the monitor data, we calculate the rate of total mass transport across the two interfaces enclosing the phase transition, denoted M_{tot}^{um} and M_{tot}^{lm}. The statistical stability of the total mass transport was demonstrated by the convergence of M_{tot}^{lm} for an increasing number of monitor tracers, with a difference smaller than 1% between results calculated using 1000 and 2000 monitor tracers. The composition parameter

C is evaluated for the n_{bin} monitor tracers that cross the interface during a time bin of length Δt. The mass transport rate –in mantle masses per billion years– is defined as $M_{tot} = (1/n_{pt}\Delta t)\sum_{i=1}^{n_{bin}}(1 + C_i(\delta\rho_c/\rho_0))$. n_{pt} is the total number of monitor tracers in the mantle domain. The injection rate for the excess mass of compositionally distinct material is calculated in a similar way by $M_{het} = (1/n_{pt}\Delta t)\sum_{i=1}^{n_{bin}} C_i(\delta\rho_c/\rho_0)$. The ratio $f_{het} = (M_{het}/M_{tot})$ measures the mass fraction of heterogeneous material injected into the upper mantle.

To calculate the excess temperature T_{ex} at the monitor tracers, the background temperature T_{bg}, based on the horizontally averaged geotherm, is subtracted from the absolute temperature: $T_{ex} = T - T_{bg}$. Hereinafter, the temperatures are 'in situ' values, unless mentioned otherwise (e.g. potential temperatures). Geochemically inferred excess temperatures of hotspots are relative to potential temperatures inferred underneath ridges, which lie outside cold regions of slab subduction. For a proper comparison to the observations we, therefore, exclude lower-than-average temperatures that are associated with downwellings in calculating T_{bg}. The excess temperature in upwellings is examined near the phase transition as defined above. Tracers that cross the upper and lower observation depths near the phase transition are labeled 'um' and 'lm', respectively. A change in T during phase boundary crossing is defined as $\delta T = T^{um} - T^{lm}$. In addition to monitoring at phase transition depth, excess temperatures are calculated at 300 km depth, for comparison with geochemically inferred excess temperatures. Using a 'sub-lithospheric' depth of 300 km ensures that thermal effects of the surface thermal boundary layer are excluded. Because the geochemical estimates are derived from surface potential temperatures, it is important to understand how the excess temperatures are affected when extrapolated to 300 km depth. For the applied mantle parameterisation, the excess of in situ temperatures is 4% larger at 300 km than at the surface. Thus, when compared to an excess of potential temperatures, typical values for T_{ex} of 250K calculated from our models, are overestimated by a value of around 10K. This small difference allows for a comparison between calculated excess temperatures in the numerical modelling experiments and petrological estimates of the excess temperatures.

3.3 Results

3.3.1 Evolution of thermo-chemical convection models

The behaviour of upwellings of lower mantle origin is determined by the parameterisation used in the mantle convection models. Key parameters are the maximum density contrast of the thermo-chemical reservoir ($\delta\rho_C/\rho_0$ and the Clapeyron slope γ of the endothermic phase transition. Values for different models are listed in Table 3.2.

The effect of $\delta\rho_C/\rho_0$ on the thermo-chemical reservoir configuration in the con-

Model	$\gamma[MPaK^{-1}]$	$\frac{\delta\rho_C}{\rho_0}[\%]$	Figure	$\bar{\delta}T_{ex}$	$\bar{\delta}T_{bg}$	$\bar{\delta}T$	P_e	B_e
S00	-2.50	0.	-	55 ± 40	-68 ± 36	-13 ± 24	-0.178	0.
S09	-2.50	0.9	Fig.1a, b	61 ± 38	-74 ± 28	-13 ± 26	-0.178	0.225
S14	-2.50	1.4	Fig.1c, d	82 ± 54	-97 ± 48	-16 ± 27	-0.178	0.349
S20	-2.50	2.	Fig.1e, f	98 ± 67	-109 ± 52	-11 ± 33	-0.178	0.497
H10	-2.50	1.4	-	96 ± 44	-110 ± 22	-14 ± 33	-0.178	0.349
W09	-1.25	0.9	Fig.2a, b	19 ± 27	-29 ± 23	-9 ± 17	-0.0889	0.225
W14	-1.25	1.4	Fig.2c, d	2 ± 16	-8 ± 8	-7 ± 13	-0.0889	0.349
W20	-1.25	2.	Fig.2e, f	23 ± 30	-32 ± 25	-9 ± 16	-0.0889	0.497

Table 3.2: Key parameters for the models investigated and temperature changes during phase crossing. See Section 3.2.1 and 3.3.3 for explanation of symbols. The average temperature values and variance is given for the tracers that have crossed the phase transition boundary during the model time interval $3.6-4.5Gyr$.

vecting mantle through time is investigated for models with a constant Clapeyron slope $\gamma = -2.5MPaK^{-1}$. In Figure 3.1, the composition and temperature field is shown after a model time of $t = 4.2Gyr$. Figure 3.1a and b shows a thermo-chemical reservoir that is configured as stretched-out blobs dispersed throughout the mantle, which results from a low excess density contrast of $\delta\rho_C/\rho_0 = 0.9\%$ (model S09). Shown in Figure 3.1c and d is a reservoir that has evolved as isolated piles of dense material on top of the CMB, for $\delta\rho_C/\rho_0 = 1.4\%$ in model S14. Figure 3.1e and f shows a thermo-chemical layer enclosing the CMB for $\delta\rho_C/\rho_0 = 2.0\%$ in model S20. Topography on the layer's interface is induced by overlying convective motion. Thus, progressively more stable reservoir configurations are observed for increasing values of the density contrast $\delta\rho_C/\rho_0$ –a results that is consistent with other modelling studies (e.g. Kellogg et al. (1999); Becker et al. (1999); Tackley (2002); Van Thienen et al. (2005)).

The endothermic phase transition acts as a partial barrier to the convective flow and has important dynamical consequences. Figure 3.1e shows an instant of largely layered mantle convection when slabs pond at the phase transition. These periods contrast with vigourous whole mantle convection that occur when the ponded material breaks through the phase boundary after reaching critical mass and sinks into the lower mantle, as shown in Figure 3.1d. As a consequence of the temporary deflection of subducting slabs at the phase transition –prior to sinking into the lower mantle– an intermittent style of mantle convection results (e.g. Machetel and Weber (1991)). Consistent with the results in e.g. Steinbach et al. (1993) and Tackley (1995), the intermittent style of convection in our models gradually weakens due to secular cooling of the upper mantle; downwellings are becoming larger and, thereby, less sensitive to deflection at the phase barrier.

The dynamics in our models is to a large extent controlled by active (buoyancy-

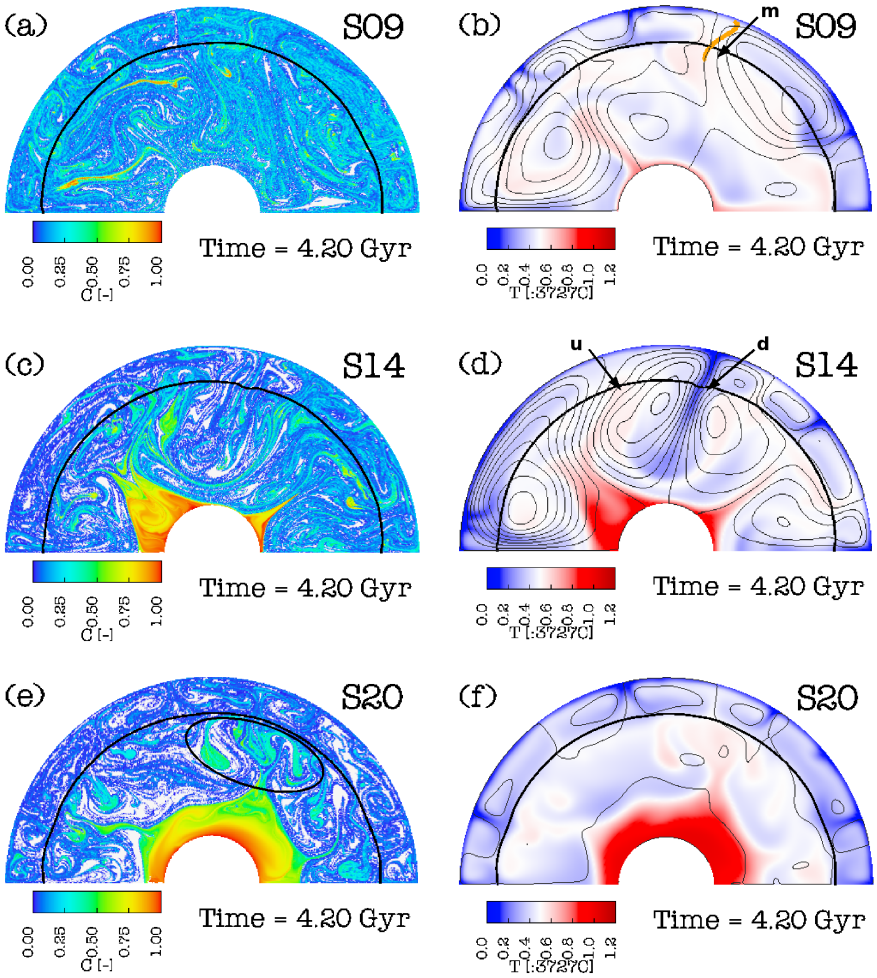

Figure 3.1: The composition field is shown in frames a, c, and e. Frames b, d, and f show the temperature field and stream lines (thin black lines). Models shown are (a and b) S09 ($\delta\rho_C/\rho_0 = 0.9\%$), (c and d) S14 ($\delta\rho_C/\rho_0 = 1.4\%$), and (e and f) S20 ($\delta\rho_C/\rho_0 = 2.0\%$). The thick black line indicates the endothermic phase transition. The Clapeyron slope in the models is $\gamma = -2.5 MPaK^{-1}$. The arrow labeled 'm' in frame (b) shows a mid-mantle upwelling. The arrows labeled 'd' and 'u' in frame (d) show examples of an active, localised mantle downwelling, and a passive broad-scale mantle upwelling, respectively. The elliptic region in frame (e) shows an example of compositionally distinct material residing underneath the phase transition. The orange line in frame (b) indicates the monitor tracer path for which the monitored temperature is shown in Figure 3.8a.

driven[2]), high-velocity, localised convective downwellings, of which an example is shown in Figure 3.1d (arrow labeled 'd'). In general, downwellings induce a passive (mechanically-driven[3]) return flow across the phase transition in the form of low-velocity, broad-scale upwellings (arrow labeled 'u' in Figure 3.1d). Absent in our models are active mantle upwellings (plumes), caused by a boundary layer instability, often considered an important ingredient of mantle dynamics (e.g. Morgan (1971); Campbell (2007)). Internal heating, depth-decreasing thermal expansivity, depth-increasing viscosity, and the presence of compositional anomalies tend to reduce the vigour of convection in the lowermost mantle (e.g. Davies (1986); Hansen et al. (1993); Hansen and Yuen (2000)). As a consequence of the resistance to deep mantle convective flow, many downwellings are being recycled at intermediate mantle depths in our models. This is shown in Figure 3.1b, d, and f, where the cold temperature anomalies suggest that downwellings stagnate at progressively shallower depths in the lower mantle. A variable depth of subduction was proposed by Albarède and Van der Hilst (2002) as a mechanism to maintain a vertical concentration gradient in the mantle, which supports the preservation of chemically distinct reservoirs, without inducing seismic reflections or scattering at mid-lower mantle depths, for which seismological evidence is lacking (e.g. Castle and Van der Hilst (2003)). Figure 3.1e shows a clear example of a reservoir with a radial compositional concentration gradient, that is maintained on a long time scale.

Figure 3.1c and d illustrate how cold downwellings destabilise a heterogeneous reservoir in the deep mantle. The upwellings that are triggered by this process do not rise towards the surface undisturbed, however. Deflection of these upwellings underneath the phase transition results in lateral material transport in the shallow lower mantle. As a result, passive upwellings have a source-region in the shallow lower mantle (see e.g. Figure 3.1b, arrow labeled 'm'). Cserepes and Yuen (2000) demonstrated that such upwellings can occur when the phase transition acts as a strong, but not complete barrier to the convective flow. Strong lateral variations in the composition field that form underneath the phase transition (see the elliptic region in Figure 3.1e) can reach the upper mantle by means of these passive mid-mantle upwellings. This way, the lower mantle is leaking heterogeneous material into the upper mantle, triggered by cold downwellings breaking through the phase boundary in a top-down dynamical setting.

Figure 3.2 shows the results of similar experiments, but for a weaker phase boundary with a Clapeyron slope of $\gamma = -1.25 MPaK^{-1}$. Similar to the previous models, the configuration of the distinct reservoir is controlled by the excess compositional density, with dispersed blobs, thermo-chemical piles, and thermo-chemical

[2]Active convective flow of material is caused by (intrinsic) buoyancy forces that result for example from density anomalies of the material relative to its surroundings.

[3]Passive convective flow of material has an external cause, for example distant pressure anomalies from which fluid motion propagate.

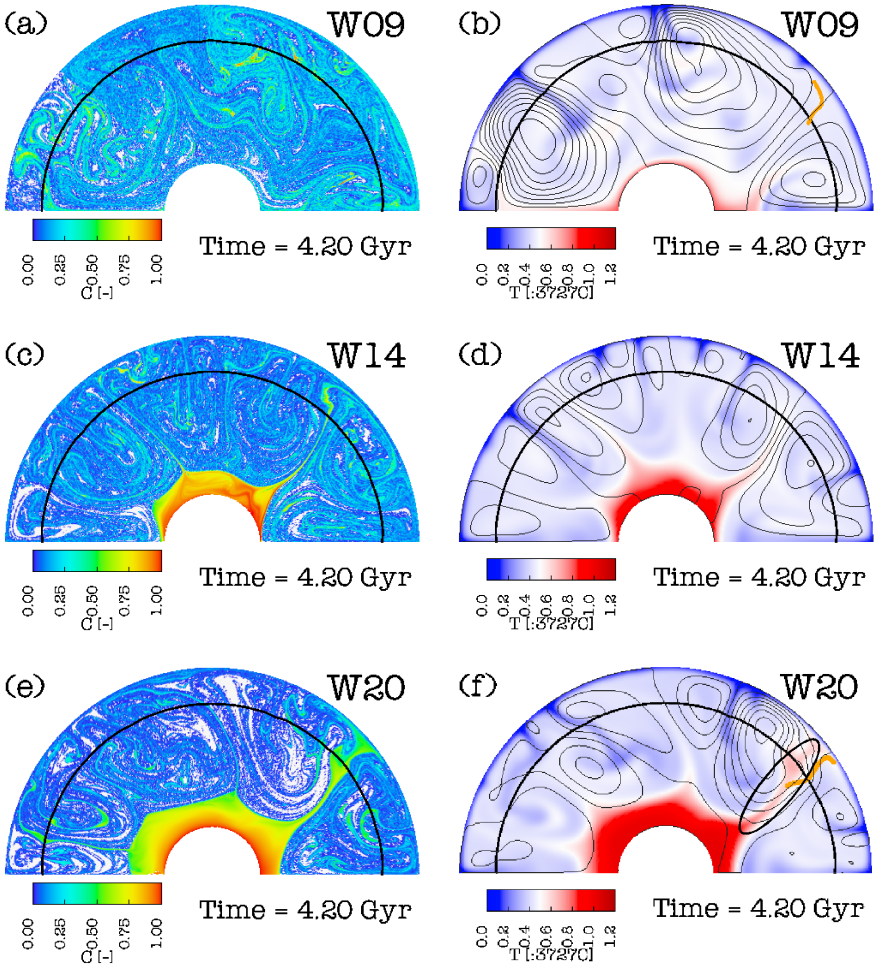

Figure 3.2: Similar as Figure 1 for models (a and b) W09 ($\delta\rho_C/\rho_0 = 0.9\%$), (c and d) W14 ($\delta\rho_C/\rho_0 = 1.4\%$), and (e and f) W20 ($\delta\rho_C/\rho_0 = 2.0\%$). The Clapeyron slope equals $\gamma = -1.25 MPaK^{-1}$. The elliptic region in frame (f) indicates a deep-seated upwelling that is crossing the phase boundary. The orange line in frames (b) and (f) indicate the monitor tracer paths for which the monitored temperature is shown in Figure 3.8b and c, respectively.

layering occurring for subsequently larger values of $\delta\rho_C/\rho_0$, as shown in Figure 3.2a, c, and e. Compared to Figure 3.1, these models are characterised by a significant reduction in the deflection of up- and downwellings at the phase transition, due to the reduced magnitude of γ. As a consequence of the reduction in slab ponding at the transition zone, the convective vigour of downwellings that sink into the lower mantle is reduced. Associated to this are relatively low mantle flow velocities at downwelling events. This is further illustrated in Figure 3.3, which shows time series of the root-mean-square mantle flow velocities (v_{RMS}). Regular v_{RMS} maxima in the left-hand frames correspond to flushing events (Machetel and Weber (1991)), where material ponding at the phase boundary has reached critical mass and breaks through the boundary. Peak velocities are lower and less localised in time in the models with a reduced Clapeyron slope (right-hand column). Another consequence of the smaller Clapeyron slope is that direct ascent of deep-seated upwellings into the upper mantle is promoted. An example of such an upwelling is shown in Figure 3.2f (elliptic region).

Characteristic time and length-scales for passive mid-mantle upwellings and active deep-seated upwellings are depicted for model W20 in Figure 3.4. The in situ temperature is depicted as a function of the angular coordinate and model time at a depth of 300 and 1000 *km*. For the deep-seated upwelling, indicated by the arrow labeled 'ds', typical time-scale and length-scales are approximately 100 *Myr* and approximately 100 *km*, respectively. A high temperature anomaly is present at both depth levels, corresponding to a single upwelling originating from the deep mantle. Passive upwellings persist on a *Gyr* time-scale and extend over 1000s of *km* in lateral direction (located in between the blue regions that indicate cold downwellings). The thermal anomaly of these passive upwellings is much smaller and the connectivity to a depth of 1000 *km* is weaker than for the deep-seated upwellings.

The degree of decoupling of the convective flow across the endothermic phase transition is illustrated by the time-averaged depth profiles of the radial flow velocity, background temperature, and the composition parameter in Figure 3.5. For the models with the larger Clapeyron slope magnitude, increased convective layering is indicated by the drop in radial flow velocity (frame a and d). As a result, a temperature contrast of several hundred degree between the upper and lower mantle evolves, in line with previous modelling studies of e.g. Tackley et al. (1993). For the models with a smaller Clapeyron slope magnitude the temperature contrast is less than 100 *K* (frame e). The curves in frame b and e show an increase of the temperature constrast across the phase transition associated with convective layering for larger values of the compositional excess density, because intrinsically dense material is more likely to be filtered from the upwelling convective flow (Weinstein (1992)). In line with the above, the contrast of the composition parameter near 660 *km* depth (frames c and f) increases for models with increasing excess density of the compositionally distinct material.

In model H10 the radiogenic heat productivity is increased by a factor 10 in

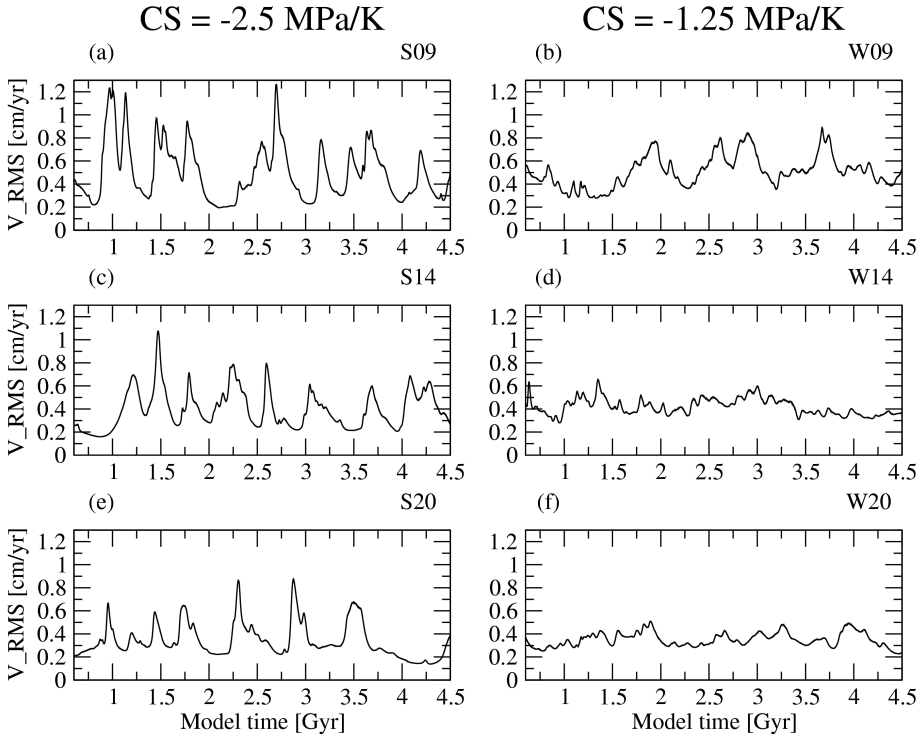

Figure 3.3: Time series of the RMS convective flow velocity V_{RMS} for models (a) S09, (b) W09, (c) S14, (d) W14, (e) S20, and (f) W20.

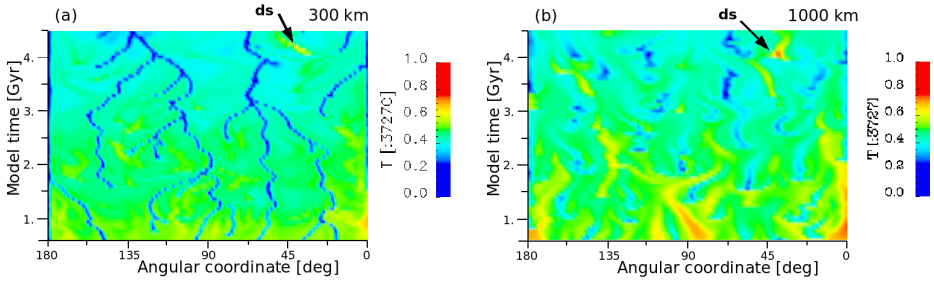

Figure 3.4: Dimensionless in situ temperature for model W20 as a function of the angular coordinate (horizontal axis) and model time (vertical axis). The cross-section depth is at (a) 300 *km* and (b) 1000 *km*. The arrows labeled 'ds' indicate a deep-seated upwelling.

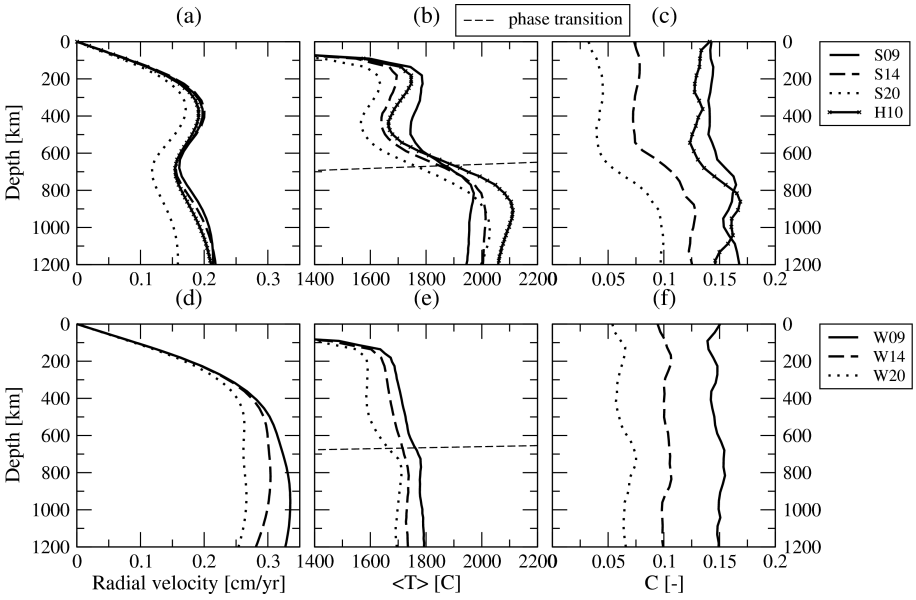

Figure 3.5: Depth-profiles averaged over model time $3.0 < t < 4.5 Gyr$ for (a and d) radial convective flow velocity, (b and e) in situ temperature, and (c and f) the composition parameter. Results are shown for models with Clapeyron slope $\gamma = -2.5 MPaK^{-1}$ (top row), and Clapeyron slope $\gamma = -1.25 MPaK^{-1}$ (bottom row), as indicated by the legend. The thin dashed line indicates the Clapeyron slope in our model.

the compositionally distinct material, but it is otherwise similar to model S14 (see Table 3.2). The increased heat productivity results in higher temperatures in the deep reservoir, which decreases its stability. We quantified the trade-off between excess heat productivity and excess density using results from previous numerical modelling experiments (Van Thienen et al. (2005)). Since viscosity is temperature-dependent, hot (weak) upwellings are less capable of penetrating the upper mantle (Nakakuki et al. (1994)). As a result of the increased convective layering, a larger temperature contrast forms across the phase transition as is shown by the curves for models S14 and H10 in Figure 3.5b and c.

3.3.2 Compositional heterogeneity of upwellings

The models presented above are similar to mantle evolution scenarios proposed by e.g. Kellogg et al. (1999), Becker et al. (1999), Tackley (2002), and Tan and Gurnis (2007) to satisfy a range of geochemical and geophysical constraints. Our models include different degrees of stability of a deep mantle reservoir and convective layering at the transition zone. Heterogeneous material from the lower mantle has been considered as a source of chemical diversity in OIB. To investigate the viability of this mechanism quantitatively for the models discussed above, we examine the amount of heterogeneous material, included in lower mantle material crossing the phase boundary. To this end we apply the monitor tracer diagnostic described in Section 3.2.1. Results are shown in Figure 3.6.

Transport of heterogeneous material should be considered along with the total transport, M_{tot}, which is shown in the top row of Figure 3.6. As expected, the rate of total mass transport is larger (factor 2–3) in models where the phase barrier is weak (dashed curves) than in models with a strong phase barrier (solid curves). This is observed for both the rate of inflow into the region enclosing the phase transformation defined in Section 3.2.1 (M_{tot}^{lm}, green curves) as well as the outflow (M_{tot}^{um}, red curves). The small difference between the inflow and outflow results from the fraction of upwelling material that fails to reach the upper mantle and is returned to the lower mantle. Furthermore, mass transport is promoted during events of downwelling that sink into the lower mantle. This is illustrated by the large transport rates (Figure 3.6a,b,c) coinciding with high flow velocities of downwelling events (Figure 3.3). Transport rates of compositionally distinct material, M_{het}, are depicted in the middle row of Figure 3.6. Similar to the total mass transport shown in Figure 3.6a,b,c, transport rates of heterogeneous material are small in models with a strong convective layering and show a time dependence that corresponds to the vigour of convection.

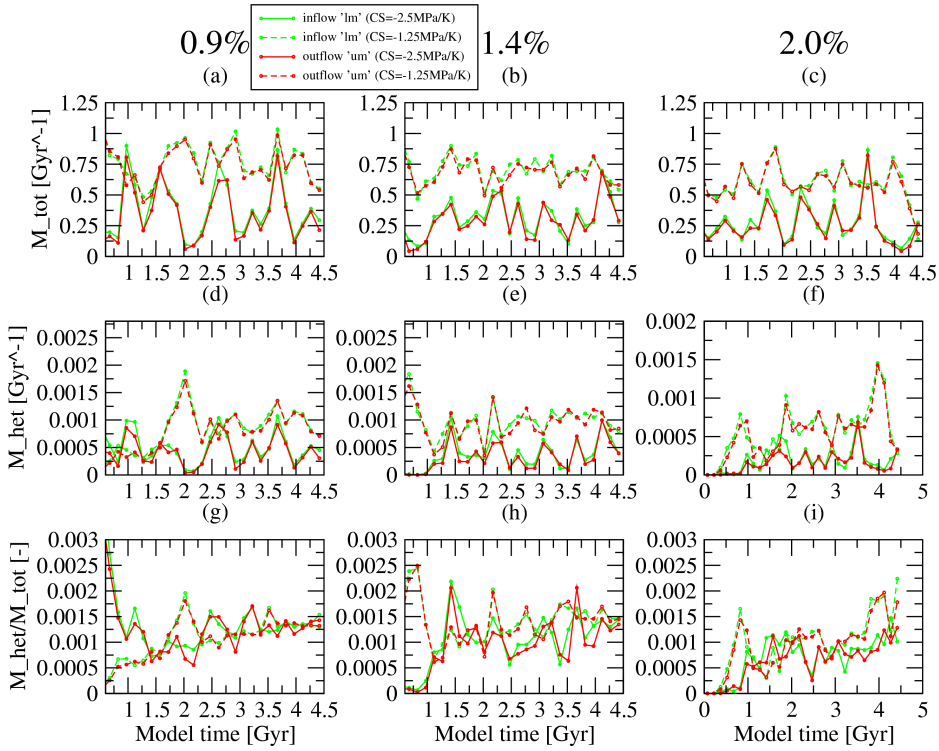

Figure 3.6: Time-averaged values of mass fractions plotted at mid-point bin times. (a,b,c) Total mass transport rate into the upper mantle. (d,e,f) Heterogeneous mass transport rate into the upper mantle. (g,h,i) Ratio of heterogeneous to total mass transport into the upper mantle. Solid lines indicate models (a, d, and g) S09, (b, e, and h) S14, and (c, f, and i) S20. The dotted lines indicate models (a, d, and g) W09, (b, e, and h) W14, and (c, f, and i) W20.

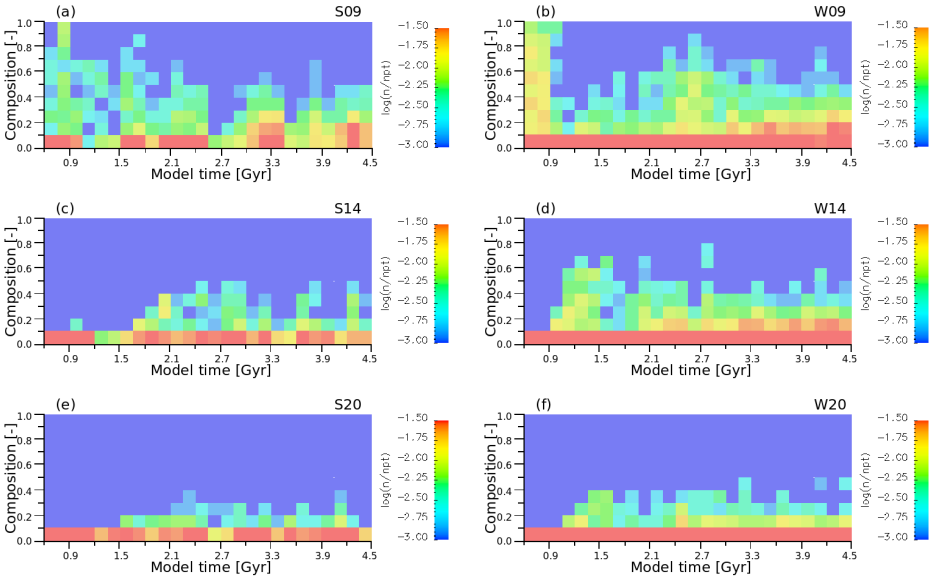

Figure 3.7: Histogram of the composition monitored during phase boundary crossing. Plotted is the logarithm of the number of tracer crossings, scaled to the total number of monitor tracers. Logarithmic values are truncated at a minimum value of -3. The model time increases from left to right from 0.6 to 4.5Gyr, composition increases upwards from 0 to 1. Models shown are (a) S09, (b) W09, (c) S14, (d) W14, (e) S20, and (f) W20.

A measure that is closely related to petrologic observations is the fraction of heterogeneous material contained in upwellings of lower mantle origin, $f_{het} = (M_{het}/M_{tot})$. The bottom row of graphs in Figure 3.6 shows the resulting time series of f_{het}. In sharp contrast to the behaviour of M_{tot} and M_{het}, the fraction f_{het} does not show a strong dependence on the Clapeyron slope. For material crossing the phase transition, the fractions f_{het}^{lm} and f_{het}^{um} (green and red curves in Figure 3.6g,h,i) fluctuate between the values 0.001 and 0.002, especially at model times larger than $t = 2.5Gyr$. Thus, upwellings entering the upper mantle contain a similar fraction of heterogeneous material, for the different thermo-chemical convection models examined. Therefore, a chemically heterogeneous source region for OIB –associated with lower mantle upwellings– seems feasible for a wide range of thermo-chemical evolution scenarios. A reduction of the fraction of heterogeneous material in upwellings during phase crossing is indicative of chemical filtering that preferentially restricts dense material to the lower mantle (Weinstein (1992)). Figure 3.6d,e,f shows slightly lower values of f_{het}^{um} compared to f_{het}^{lm}. The ratio between f_{het}^{um} to f_{het}^{lm}, averaged over the entire model evolution has a typical value of 0.85, indicating that around 15% of dense material is removed from upwelling material entering the phase transition zone, as a result of

chemical filtering.

We also examine the ability of upwellings to reproduce a compositionally diverse signature that is characteristic for OIB. Figure 3.7 shows 2-D histograms where the statistical distribution of the composition of material entering the upper mantle through the endothermic phase boundary is presented for time bins of 150 Myr and 10 bins that cover the full composition range. Logarithmic values of the number of monitor tracers that have crossed the phase transition normalised by the total number of monitor tracers are colour coded in the 2-D histograms. A sharp decrease in the transport into the upper mantle for material with larger composition values is shown in all histograms in Figure 3.7. The reduced transport of material of progressively larger excess density is caused primarily by gravitational stability effects, and to a lesser extent by chemical filtering at the phase transition, as has been discussed in preceeding paragraphs. For the entire composition range, the material transport increases at periods of large material exchange between the upper and the lower mantle (see Figure 3.7), that coincide with large values of v_{RMS} (see Figure 3.3). Increasing $\delta\rho_C/\rho_0$ increases the gravitational stability of the heterogeneous reservoir in the lower mantle as was clearly illustrated by the composition fields in Figure 3.1 and 3.2. Figure 3.7a, c, and e & 3.7b, d, and f show models for increasing values of the reservoir excess density; $\delta\rho_C/\rho_0 = 0.9\%$, 1.4%, and 2.0%, respectively. The injection of heterogeneous material into the upper mantle decreases in these models of progressively larger excess density. When increasing the Clapeyron slope from $\gamma = -1.25 MPaK^{-1}$ to $\gamma = -2.5 MPaK^{-1}$ (right- and left-hand column in Figure 3.7, respectively) transport of compositionally distinct material into the upper mantle is reduced. The reduction is caused primarily by a limited total mass exchange between the upper and lower mantle as was shown by the results presented in Figure 3.6.

3.3.3 Excess temperature of upwellings

To investigate the effect on excess temperatures of the post-spinel phase transition we evaluate the change in excess temperature, denoted T_{ex}, during phase boundary crossings: $\delta T_{ex} = T_{ex}^{um} - T_{ex}^{lm}$. Note that positive values of δT_{ex} are associated with an increase in the excess temperature, during phase boundary crossing. Firstly, a temperature contrast across the phase transition results in negative values for $\delta T_{bg} = T_{bg}^{um} - T_{bg}^{lm}$ and therefore positive values of δT_{ex}. Secondly, cooling of the ascending tracer during phase boundary crossing results in negative values of $\delta T = T^{um} - T^{lm}$, which reduces the excess temperatures.

For a selection of convective upwellings we compare the temperature, T, to the background temperature, T_{bg}. Figure 3.8a shows that a large background temperature contrast of approximately $300K$ has developed across the endothermic phase transition for model S09, which has the higher Clapeyron slope magnitude ($\gamma = -2.5 MPaK^{-1}$). A typical example of a temperature-depth trajectory for a passive,

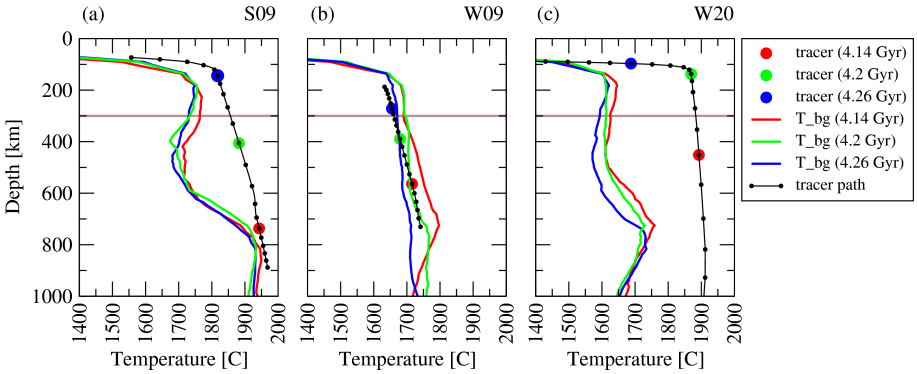

Figure 3.8: Red, green, and blue curves show the background temperature, T_{bg} (defined in Section 3.2.1), for model times $t = 4.14$, 4.2, and $4.26 Gyr$, respectively. The black curves show the temperature of monitor tracers crossing the phase transition from below (see the orange curves in Figures 3.1b and h & 3.2b and h). Small black dots represent the temperature and depth at equi-distant time intervals of $8 Myr$. Coloured thick dots are associated with background temperature profile of corresponding colours. The horizontal brown line indicates the sub-lithospheric monitor depth of 300 *km*.

mid-mantle upwelling is shown by the black curves in Figure 3.8a, which define the PTt-path of a single monitor tracer. In the lower mantle the temperature in the passive upwellings is close to the background temperature (cf. black and red curves below 700 *km*). As the particle tracer crosses the phase transition, the background temperature contrast between the upper and lower mantle is the main contributor to the excess temperatures of approximately $200K$ monitored at 300 *km* depth (brown line). A comparatively small temperature increase is related to latent heat absorption, which is shown by the small kink in the black curve near 660 *km* depth.

Figure 3.8b shows that the lower Clapeyron slope magnitude ($\gamma = -1.25 MPaK^{-1}$) produces a small background temperature contrast evolves across the phase transition. The PTt-path of the mid-mantle upwelling is close to the background temperature in the lower mantle, similar to the passive upwelling of model S09 in frame a. In this case, the temperature of the upwelling follows the background temperature closely when it enters the upper mantle. The excess temperature monitored at a depth of 300 *km* is close to $0K$.

The PTt-path of an active deep-seated upwelling is clearly different from the passive mid-mantle upwellings (Figure 3.8c) by having a temperature of around $200K$ above the background mantle temperature in the lower mantle. Because of its positive thermal buoyancy, the active upwelling ascends faster towards the surface than the passive upwellings, as shown by the larger spacing of the black dots, plotted at equi-distant time intervals of 8 *Myr*. The high absolute temperature of the deep-seated

upwelling is expressed in the high excess temperature around $350K$ monitored at 300 km depth, which exceeds geochemically inferred values of 150-$300K$.

The above results show that the excess temperature of upwellings increases with the temperature constrast at the phase transition, which in turn increases with the magnitude of the Clapeyron slope. Analysis of the different terms in the energy equation shows that the effects on excess temperature of latent heat production, adiabatic decompression, radiogenic heating, viscous dissipation, and heat diffusion are relatively small. The largest contribution to changes of the in situ temperature is associated with the effect of latent heat. For a $2000K$ convective upwelling, the latent heat effect at a Clapeyron slope of $\gamma = -2.5 MPaK^{-1}$ results in a $89K$ temperature increase in the upwelling, which is in agreement with other mantle convection studies (e.g. Christensen (1998)). Half this value is present for the models with a Clapeyron slope of $\gamma = -1.25 MPaK^{-1}$. As a result, latent heat promotes high excess temperatures in models with a large Clapeyron slope magnitude. Adiabatic cooling is close to $20K$ per 100 km for a $2000K$ convective upwellings near the depth of the endothermic phase transition. Radiogenic heating results in a temperature increase smaller than $0.2K$ per Myr, around a model time of 4.2 Gyr, or less than $2K$ during a 100 km rise at a vertical velocity of $1 cmyr^{-1}$. Conductive heat transfer can be neglected: it is many times smaller than convective heat transfer, for an upwelling with a vertical velocity of $1 cmyr^{-1}$ ($Pe = 36$, using a length-scale of $h = 100km$). The viscous dissipation was calculated in a 400×400 box surrounding a rising tracer at the moment of phase transition crossing. Typical low values correspond to a heating rate of $1K$ per $100Myr$.

The examples shown in Figure 3.8 represent the general behaviour of passive and active upwellings in the experiments conducted in this study. Average values over the time interval $3.6 < t < 4.5 Gyr$ of δT_{bg}, δT and δT_{ex} are listed in Table 3.2. A temperature contrast between the upper and lower mantle results in negative values for δT_{bg}, giving a positive contribution to δT_{ex}. This is counteracted by absolute temperatures that decrease during phase crossing (i.e. negative δT). For weak convective layering ($\gamma = -1.25 MPaK^{-1}$), δT_{bg} is slightly larger in magnitude than δT, which results in a modest rise of excess temperatures. For strong convective layering ($\gamma = -2.5 MPaK^{-1}$), however, the large increase of excess temperatures δT_{ex} is controlled by a decrease in the background mantle temperature T_{bg}, and the relative contribution of the absolute temperature effect δT is small.

The influence of the phase transition on the excess temperature of mantle upwellings during model evolution is shown in Figure 3.9. Values for δT_{ex} up to $400K$ are reached in models with Clapeyron slope $\gamma = -2.5 MPaK^{-1}$. The pronounced temporal fluctuations result from the intermittent style of mantle convection; during periods of layered mantle convection the temperature contrast across the phase change increases, which promotes large values of δT_{ex}. These periods correspond to the low mantle flow velocities shown in Figure 3.3a, c, and e. The behaviour of excess tem-

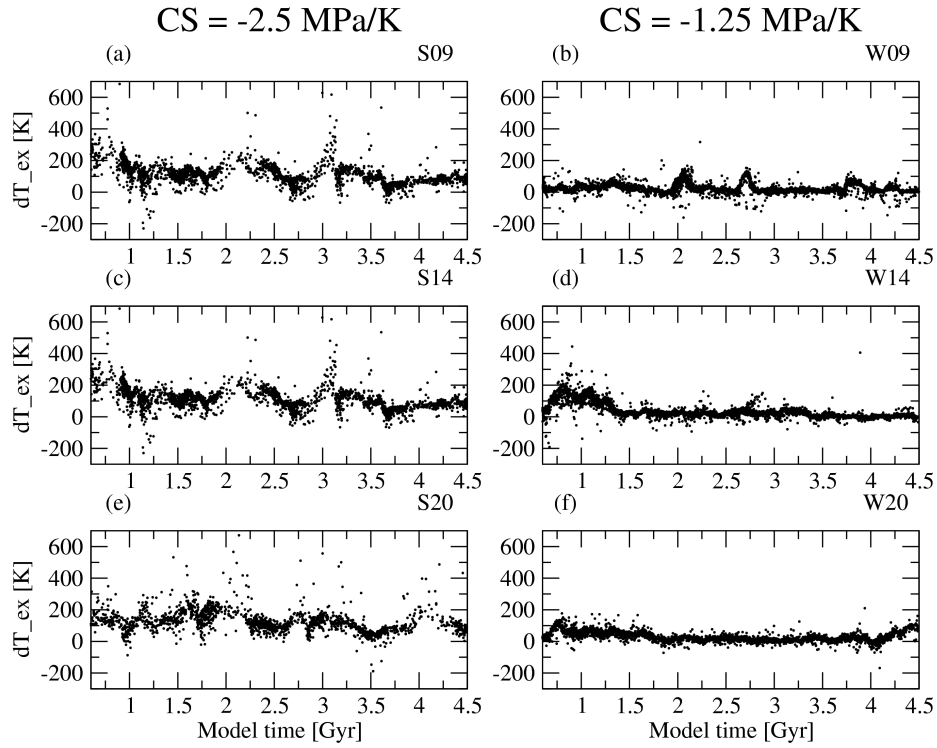

Figure 3.9: Time series of δT_{ex}; the change in excess temperatures in upwellings during crossing of the phase transition (see Section 3.2.1 for definitions). Models shown are (a) S09, (b) W09, (c) S14, (d) W14, (e) S20, and (f) W20.

perature is notably different in models with Clapeyron slope $\gamma = -1.25 MPaK^{-1}$. In absence of strong convective layering, a less pronounced temperature contrast across the phase transition develops, compared to the case with $\gamma = -2.5 MPaK^{-1}$. As a consequence, a modest increase in excess temperature during phase boundary crossing occurs in the models with the weaker Clapeyron slope ($\gamma = -1.25 MPaK^{-1}$). This is shown in Figure 3.9b, d, and f where the bulk of upwelling material is characterised by δT_{bg} values below l00K. The smaller values of δT_{bg} listed in Table 3.2 further illustrate this effect.

Next, we examine the excess temperature of upwellings that have crossed the phase boundary and approach the zone of partial melting acting as the source region of intra-plate volcanism. Figure 3.10 shows time series of the excess temperatures

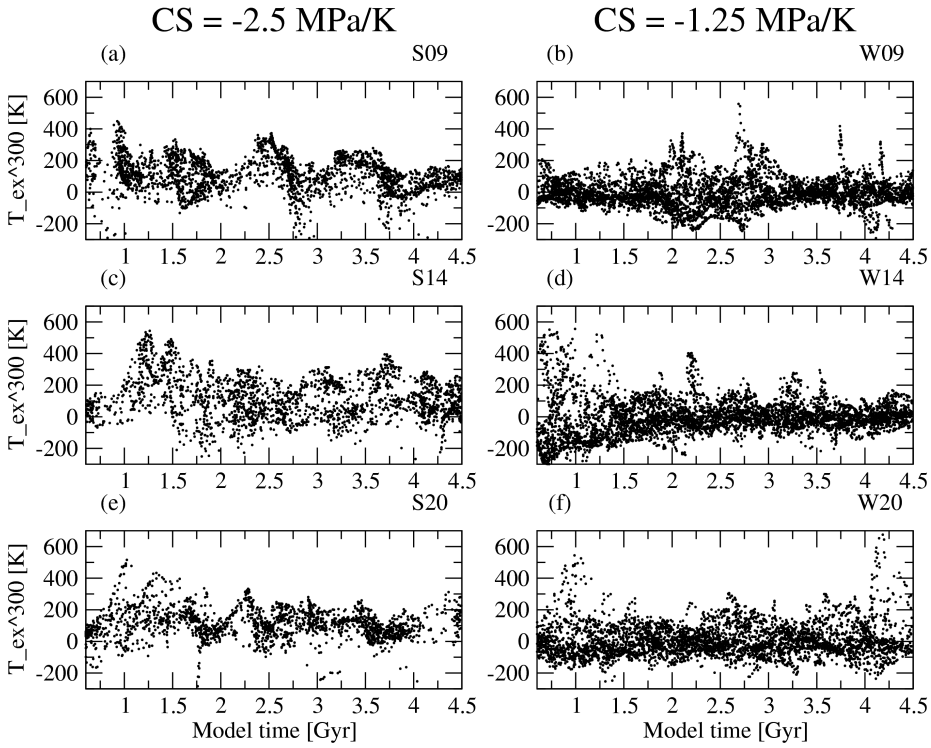

Figure 3.10: Time series of the excess temperature T_{ex} at a sub-lithospheric depth of 300 *km* (see Section 3.2.1 for definitions). Models shown are (a) S09, (b) W09, (c) S14, (d) W14, (e) S20, and (f) W20.

monitored at a sub-lithospheric depth of 300 *km*. In models with Clapeyron slope $\gamma = -1.25 MPaK^{-1}$ (right-hand column of Figure 3.10) the excess temperature in the upwellings is generally less than $300K$ – values that are consistent with geochemical estimates of 150-300K excess temperature extrapolated along a mantle adiabat to surface pressure (e.g. Putirka et al. (2007); Herzberg et al. (2007)). Infrequently, however, deep-seated upwellings (see Figure 3.2b) produce large excess temperatures with peak values as large as $T_{ex} = 500K$. Clearest examples are shown in Figure 3.10b for model W09 around model times of $t = 2.7, 3.7$ and $4.2 Gyr$, for model W14 (Figure 3.10d) at $t = 2.2$ and $3.5 Gyr$, and model W20 (Figure 3.10f) at $t = 4.2 Gyr$.

For the deep-seated upwellings, large excess temperatures result from high absolute temperatures in the upwellings (Figure 3.8c). Models with Clapeyron slope

$\gamma = -2.5 MPaK^{-1}$, shown in the left-hand column of Figure 3.10, show large values of T_{ex}, up to $500K$. These values are substantially larger than the geochemically inferred values. For the models with the larger Clapeyron slope magnitude, the maxima of excess temperatures monitored at 300 *km* depth only fall within the range of geochemically inferred excess temperatures for the model with neutral compositional excess density (model S00, Table 3.2). This is explained by excess temperatures that increase with the compositional excess density, which promotes the convective layering, as was shown in Figure 3.5.

3.4 Discussion

Endothermic phase transitions –such as the post-spinel phase transition incorporated in our models– promote layering of the convective flow (e.g. Tackley (1995)) and produce a temperature constrast across the phase boundary (e.g. Christensen and Yuen (1985)). We have shown that, as a consequence of this temperature contrast, the excess temperature increases in upwellings upon crossing of the phase transition. Analysis of the energy equations shows that –during phase boundary crossing– the excess temperature in upwellings is controlled by the background temperature.

At a Rayleigh number of 4×10^6 and a Clapeyron slope of $-2.5 MPaK^{-1}$, the effective phase buoyancy parameter $P_e = -0.18$ is close to the critical value of $P = -0.25$ estimated by e.g. Christensen and Yuen (1985), Machetel and Weber (1991)), and Nakakuki et al. (1994). The occurence of intermittent, partial layering in our models is in agreement with those studies. Partial layering at the transition zone is in line with seismological data, that indicate a varying degree of connectivity of seismic velocities across the mantle transition zone for different study regions (e.g. Van der Hilst et al. (1991); Van der Hilst and Seno (1993); Fukao et al. (1999); Nataf (2000); Lei and Zhao (2006); Zhao (2007)). The temperature contrast that develops between the upper and lower mantle (around $400K$ for a Clapeyron slope of $\gamma = -2.5 MPaK^{-1}$) is in agreement with previous modelling studies (e.g. Tackley et al. (1993)).

In general, both the strength of the thermal boundary in the phase transformation region and the excess temperature increases with increasing magnitude of the Clapeyron slope. In the models with a Clapeyron slope value of $\gamma = -1.25 MPaK^{-1}$ the contribution of convective layering to excess temperatures is around $100K$. For these models, upwellings of lower mantle origin measured at a sub-lithospheric depth of $300km$ have maximum excess temperatures that fall in the range of geochemically inferred values of 150-$300K$ for the potential temperature extrapolated adiabatically to surface pressure (e.g. Schilling (1991); Putirka et al. (2007); Herzberg et al. (2007)). The infrequent occurence of deep-seated upwellings that enter the upper mantle with excess temperatures as large as $500K$ could be associated with the formation of LIPs, because high excess temperatures promote the generation of large volume flood basalt eruptions (Farnetani and Richards (1994)). Furthermore, a deep mantle origin from

a heterogeneous reservoir has been proposed for LIPs (e.g. Torsvik et al. (2006)). A convection regime with low degrees of layering at the transition zone, therefore, provides an interesting possibility for generating LIPs that coexist with hotspots.

A Clapeyron slope of $-2.5 MPaK^{-1}$, which produces stronger convective layering, yields excess temperatures that are larger than the $150 - 300K$ inferred from OIB geochemistry (e.g Schilling (1991); Putirka et al. (2007); Herzberg et al. (2007)). The difference between model predictions and geochemically inferred values of excess temperature cannot be explained by heat diffusion, adiabatic decompression, or entrainment of (colder) surrounding material (Farnetani and Richards (1994)). For upwellings with such high excess temperatures, the formation of massive vigourous surface eruption events is expected.

Thus, our modelling suggests that excess temperatures are consistent with geochemically inferred values when the transition zone acts as a weak barrier to convective flow. At larger degrees of layering, lower mantle upwellings may continuously generate flood basalt events –a scenario that is less realistic for the present-day Earth. The residense of hot, intrinsically dense material underneath the phase transition promotes convective layering and, consequently, higher excess temperatures. Therefore, the Clapeyron slope magnitude must be smaller for thermo-chemical mantle convection than for iso-chemical convection to produce excess temperature values that are consistent with inferences from mantle petrology.

The 4% larger excess temperatures that result from evaluating temperatures at 300 *km* depth instead of extrapolating the temperatures adiabatically to the surface (see Section 2.1) is small, compared to the magnitude of calculated values and, therefore, does not change the conclusions of our study. The background temperatures extrapolated adiabatically to the surface from a sub-lithospheric depth of 300 *km* is around $1500K$ after 4.5 *Gyr* model time. We realise that this value is on the high side compared to petrological estimates of the mantle potential temperature in the range 1300-$1450K$ (e.g. McKenzie and Bickle (1988); Green and Falloon (1998); Putirka et al. (2007)). With additional control experiments, we verified the validity of the results by showing the small influence of the initial potential temperature on the diagnosed excess temperature and chemical heterogeneity in upwellings.

In the models, the compositionally distinct material contained in mantle upwellings results from a heterogeneous reservoir, initially placed in the lower mantle. Evidence for a compositionally heterogeneous lowermost mantle comes from seismological observations (Van der Hilst and Kárason (1999); Ishii and Tromp (1999); Saltzer et al. (2004); Deschamps et al. (2007)), and geochemical contraints (Hofmann (1997)). A compositionally distinct mantle reservoir can accumulate from the (combined) addition of eclogite-rich material subducted or delaminated from the lithosphere (Christensen and Hofmann (1994); Van Thienen et al. (2004); Tolstikhin et al. (2006)), iron-rich products from the core (Jeanloz and Lay (1993); Mao et al. (2006)), and remnants of magma ocean solidification in the early Earth (e.g. Abe (1996)).

Our model results suggest that different combinations of convective flow layering and reservoir configurations can produce upwellings that transport similar fractions of compositionally distinct material to the upper mantle. Apparantly, the chemically heterogeneous signature of OIB (e.g. Hofmann (1997)) is feasible for a wide range of evolutionary mantle models, including possible scenarios where the deep mantle reservoir is configured as a continuous layer (e.g. Kellogg et al. (1999)), isolated piles on top of the CMB (Tackley (2002)), or stretched-out blobs dispersed throughout the mantle (Becker et al. (1999)). Several modelling studies have shown the feasibility of reproducing the chemical signature of OIB in distinct mantle reservoirs (e.g. Christensen and Hofmann (1994); Samuel and Farnetani (2003); Xie and Tackley (2004a,b)). Our results show that a heterogeneous compositional expression in upwellings of lower mantle origin is a robust feature of thermo-chemical mantle convection. We have demonstrated that the densest fractions of a compositionally distinct reservoir are retained in the lower mantle due to gravitational stability and to a smaller extent by chemical filtering at the phase transition. The reservoir can serve as a complement for Earth's heat budget and resolve apparant conflicts in isotope systematics (Kellogg et al. (1999); Albarède and Van der Hilst (2002); Tolstikhin et al. (2006)).

3.5 Conclusions

We have performed numerical modelling experiments to study the impact of convective layering at the transition zone on transport of compositionally heterogeneous material from the deep lower mantle into the upper mantle. We compared the excess temperatures produced by models with phase transitions of different strength with estimates from geochemical analysis of intra-plate volcanism. We tested a range of long-term thermo-chemical evolution scenarios that have been proposed as possible mantle models (e.g. Kellogg et al. (1999); Becker et al. (1999); Tackley (2002)) by modelling compositionally distinct reservoirs of different stability conditions. The main conclusions are the following.

(i) An increase of excess temperatures in upwellings that enter the upper mantle results from the temperature constrast across the post-spinel phase transition, induced by regional and transient convective layering. When upwellings cross the phase transition, a $400K$ increase in excess temperatures occurs during periods of partially layered mantle convection, in models with a Clapeyron slope value of $\gamma = -2.5 MPaK^{-1}$.

(ii) At low degrees of mantle flow layering, values for the excess temperatures of upwellings are consistent with the combined existence of hotspots and LIPs. In contrast, a strong degree of convective layering promotes upwellings of high excess temperatures that can produce massive flood basalt volumes. Such a scenario is not consistent with data from present-day intra-plate volcanism at the Earth's surface. Because hot, intrinsically dense material below the phase transition favours a high degree of convective layering, thermo-chemical convection implies a smaller Clapey-

ron slope (for the excess temperature to be consistent with OIB analysis) than isochemical convection.

(iii) For a range of thermo-chemical mantle convection scenarios, heterogeneous material transport in upwellings of lower mantle origin towards the surface provides a mechanism to generate a chemically heterogeneous signature of OIB for a wide range of stability conditions for the deep mantle.

Chapter 4

Gravity expressions of thermo-chemical mantle convection models

4.1 Introduction

4.1.1 Can Earth's geoid be used as an indicator for compositional mantle heterogeneity?

Thermo-chemical mantle convection has been proposed as a model that satisfies geochemical, seismological, and heat-budget constraints (e.g. Kennett et al. (1998); Van der Hilst and Kárason (1999); Kellogg et al. (1999)). Geodynamic modelling studies have confirmed that a compositionally distinct reservoir can survive convective overturn on a billion year time-scale (e.g. Davaille (1999); Hansen and Yuen (2000); Tackley (2002); Van Thienen et al. (2005)). Although direct evidence of an interface separating compositional layers is not available (e.g. Castle and Van der Hilst (2003)), recent seismological studies indicate that a compositionally distinct component in the lower mantle is likely (e.g. Saltzer et al. (2001, 2004); Trampert et al. (2004); Helmberger and Ni (2005); Deschamps et al. (2007)).

Earth's geoid and dynamic topography of the surface and CMB are important observables, because they are closely related to the convective state and the internal density and viscosity structure of the mantle. Previous studies have shown that some amount of compositional heterogeneity in the deep mantle is compatible with the available gravity data (Ishii and Tromp (1999); Forte and Mitrovica (2001); Trampert et al. (2004)). Assessing the influence of compositional heterogeneity on the geoid is important as it may be used to derive constraints on the heterogeneity of the mantle from gravity observations. We will demonstrate, however, that the gravity expression of compositionally distinct material can be compensated by the effect of positive

thermal anomalies, which implies that the geoid does not provide an unambigious diagnostic to distinguish between thermo-chemical and iso-chemical mantle convection models.

The total dynamic geoid is well-constrained by satellite gravity missions. Undulations of the observed geoid are caused by internal density contrasts in the mantle (static term) originating from variations in temperature, composition, and solid-state phase transformations. In addition, the geoid depends on mass anomalies associated with dynamic topography of the surface boundary, CMB, and internal density interfaces. Both the magnitude and the sign of the total geoid undulation are directly related to the viscosity structure of and density distribution in the mantle (e.g. Morgan (1965); McKenzie (1977); Hager (1984)).

In addition to geoid signals, valuable, although less well-constrained information for the mantle structure is provided by knowledge of the dynamic boundary topography of the Earth's surface and CMB, which originate from stress fields related to mantle convective flow. Estimated values of the dynamic topography are obtained by correcting for isostatically compensated topography, and such estimates depend on the assumed crustal model. Available estimates for the global-scale surface dynamic topography differ substantially with inferred amplitudes varying between 100's of meters up to ~ 4 *km* (e.g. Wheeler and White (2000); Forte and Perry (2000); Panasyuk and Hager (2000b); Sandiford (2007)). Similarly, models of the CMB topography do not clearly correlate between different seismological studies, with estimates of the maximum topographic amplitude varying from 1 to 10 *km* (e.g. Redkal and Doornbos (1992); Garcia and Souriau (2000); Sze and van der Hilst (2003)).

Long wave-length convective flow primarily affects the longest wave-length ($\ell \leq 9$) geoid and dynamic topography (e.g. Ricard et al. (2006)). Although short wavelength anomalies provide a useful constraint for shallow structures on the regional scale or smaller, only long wave-length anomalies are relevant when studying the large-scale mantle convection processes.

4.1.2 Previous work

Geoid inversion studies have been done to retrieve the mantle viscosity structure that best fits the observed geoid and, optionally, surface dynamic topography. A good fit to the observed geoid (i.e. a variance reduction of more than 85%) is produced by density models of the mantle inferred from seismic tomography or subduction history. By inversion, the viscosity structure of the mantle can be inferred from such models. However, the non-unique character of the inversion problem allows a large variation in possible viscosity distributions that fit the observational data (e.g. Richards and Hager (1984); Forte and Peltier (1991); King (1995); Čadek et al. (1998); Panasyuk and Hager (2000a); Čadek and Fleitout (2006)). A robust characteristic, argued for by most inversion studies, is an increase in viscosity at or near 660*km* depth (e.g. Hager

(1984); Corrieu et al. (1994); Čadek and Van den Berg (1998)).

The importance of the degree of convective layering at the transition zone was noticed by several authors. Geoid inversion results of Thoraval et al. (1995) show that local layering of the convective flow –induced by the endothermic phase transition near 660 *km* depth– causes a reduction of the surface dynamic topography. Čadek and Fleitout (2003, 2006) obtain a best fit to the long wave-length geoid when mass exchange across the 660 *km* discontinuity is reduced by 60%.

Many geoid inversion studies use an input density model based on the assumption that seismic velocity variations have a purely thermal origin throughout the mantle. However, mounting evidence for compositionally heterogeneous material indicates that both the density structure as well as the seismic velocities in the mantle are affected by compositional mantle heterogeneity (e.g. Kellogg et al. (1999); Trampert et al. (2004); Ohta et al. (2008)). Therefore, density variations may not scale linearly with seismic wavespeed variations.

In a recent study, Simmons et al. (2007) address the influence of compositional variations on the results of a joint inversion of seismic and geodynamic data. They allow lateral variations in the conversion ratio of density to seismic S-wave velocity, which are subsequently interpreted as being related to compositional variations. An improved fit to the data was found, compared to purely thermal inversion models. The presence of compositionally dense material is inferred at mid-mantle depth in the large low shear velocity province (LLSVP) underneath Africa –a region where seismological data is suggestive of compositional heterogeneity (e.g. Van der Hilst and Kárason (1999); Helmberger and Ni (2005)). Unfortunately, the study does not show the separate contributions of compositional heterogeneity to static and boundary topography-related geoid undulations.

The predictive character of the forward approach –calculating the geoid from mantle convection models– provides a useful complement to inversion models by testing the influence of compositional heterogeneities on the geoid. Čížková and Matyska (2004) calculated the gravity signal for a mantle with a globally continuous compositional interface at a depth of 1000 *km*. However, there is no direct evidence for a global boundary at 1000 *km*. As far as we are aware, there have been no systematic investigations of the gravity expression of forward models with large-scale lateral variations in composition of the lower mantle such as proposed by Kellogg et al. (1999); Becker et al. (1999); Tackley (2002).

4.1.3 Objective

In this chapter we test the hypothesis of a chemically heterogeneous mantle against available gravity data. To this end, we examine the long wave-length geoid expression of heterogeneous mass distributions in models of thermo-chemical mantle convection and compare this with models including only thermal or phase-related density vari-

ations. In our models we separate the total density anomaly in thermal, phase, and composition-related contributions. This allows us to evaluate separately the relative importance of gravity signals originating from the different density perturbations and different mantle depths.

We make use of the results of Chapter 3 and focus the analysis on the gravity expression for models with different degrees of stability of a compositionally distinct reservoir and convective layering at the transition zone. We show a large expression in the static geoid of compositionally distinct material in the lower mantle. We also show, however, that this expression can be masked by thermal effects. The transition can influence convective transport in the mantle and the correponding expression in the gravity signal has been shown for purely thermal models (Thoraval et al. (1995)). Here, we demonstrate the implications for the long wave-length gravity signals of the distribution of compositionally distinct mantle domains controlled by transition zone layering.

4.2 Method

The total dynamic geoid anomaly is calculated by summation of the static and boundary topography component, i.e.

$$\Delta N = \Delta N_s + \Delta N_b. \tag{4.1}$$

Static geoid undulations, ΔN_S, are produced by internal density anomalies, $\Delta\rho$, in the mantle domain. From the numerical convection experiments, we evaluate separately the contributions to $\Delta\rho$ that originate from variations in temperature, $\Delta\rho_T$, mineral phase, $\Delta\rho_{ph}$, and composition, $\Delta\rho_C$, based on the equation of state, introduced in Chapter 2:

$$\begin{aligned} \Delta\rho &= \rho - \langle\rho\rangle \\ &= \Delta\rho_T + \Delta\rho_{ph} + \Delta\rho_C \\ &= \rho_0 \left[-\alpha(T - \langle T\rangle) + (\Gamma_{ph} - \langle\Gamma_{ph}\rangle)\frac{\delta\rho_{ph}}{\rho_0} + (\Gamma_C - \langle\Gamma_C\rangle)\frac{\delta\rho_C}{\rho_0} \right]. \end{aligned} \tag{4.2}$$

Symbols are explained in Table 4.1 and 4.2, and terms in '$\langle\rangle$'-brackets refer to the laterally averaged values. The distribution of the density anomaly $\Delta\rho$ is represented by a discrete set of 65 concentric mass sheets with surface density anomaly $\Delta\sigma$. The conversion from $\Delta\rho$ to $\Delta\sigma$ is described in Eqs. 4.20 and 4.21. Because the external gravity field is the sum of individual mass sheet contributions, the analysis is easily restricted to a radially bounded sub-domain, if desired.

The basis of our calculation is formed by a solution of the Poisson equation which relates the gravity potential anomaly, ΔU, to mass density anomaly, $\Delta\rho$, as follows

$$\nabla^2 \Delta U = 4\pi G_0 \Delta\rho, \tag{4.3}$$

with G_0 the gravitational constant (see Table 4.1). We solve the Poisson equation (4.3) in polar coordinates in the spectral domain, which is computationally advantageous. The solution is specific for the 2-D cylindrical geometry used in this study and is described (in addition to the solution in 2-D cartesian geometry) in more detail in Appendix A. To investigate how the above calculations in 2-D cylindrical geometry relate to 3-D spherical geometry, we present the results of a benchmark comparison for static geoid calculations in Appendix B. The smallest difference between the two geometries are obtained for the long wave-length geoid anomalies on which the present study focusses.

To obtain the geoid anomaly ΔN_S, corresponding to gravity potential ΔU_s, we use Bruns Theorem (e.g. Lambeck (1988))

$$\Delta N(\vec{x}) = \frac{-\Delta U(\vec{x})}{g(\vec{x})}. \tag{4.4}$$

We substitute a constant (radially inward) gravitational acceleration ($g(\vec{x}) = g_0$) which closely approximates the nearly constant value for Earth's mantle. From individual contributions to the density anomaly $\Delta\rho_T$, $\Delta\rho_C$, and $\Delta\rho_{ph}$, geoid undulations ΔN_T, ΔN_C, and ΔN_{ph} are calculated. The static geoid signal is the sum of the contributions above

$$\Delta N_s = \Delta N_T + \Delta N_C + \Delta N_{ph}. \tag{4.5}$$

A second contribution to the geoid results from mass anomalies related to dynamic topography on the top and bottom boundaries of the mantle domain (i.e. the surface and CMB), denoted ΔN_b. Boundary topography is calculated from the flow-induced normal stress acting on the fixed boundaries of the computational domain. We calculate the normal stress $\sigma^i_{nn}(\vec{x}^i_b)$ along both the surface boundary ($i = 1$) and CMB ($i = 2$) from the dynamic pressure and the shear stress $\sigma_{nn} = -\Delta P + \tau_{nn}$. From the normal stress, σ_{nn}, we calculate the dynamic topography, h_b, induced on the boundary i as follows (Richards and Hager (1984))

$$h^i_b = (-1)^{i+1} \frac{\sigma^i_{nn}}{\Delta\rho_i g_0}. \tag{4.6}$$

The relaxation time of boundary deformation ($\tau = 2\eta k/(\rho g)$ (Haskell (1935))) is substantially shorter than the characteristic time scale of convective mantle flow (e.g. Hager (1984)). We therefore consider dynamic topography to be formed instantaneously.

Symbol	Parameter	Value	Dimension
γ	Clapeyron slope		PaK^{-1}
$\Gamma_{ph} = \frac{1}{2}(1+\sin(\pi\frac{z-z_{ph}}{2d_{ph}}))$	Phase parameter $(z \in [z_{ph}-d_{ph}, z_{ph}+d_{ph}])$		–
$\Gamma_{ph} = H(z-z_{ph})$	Phase parameter $(z \notin [z_{ph}-\frac{d_{ph}}{2}, z_{ph}+\frac{d_{ph}}{2}])$		–
H	Heaviside function		–
d_{ph}	Half-width phase transition	100	km
$\frac{\delta\rho_{ph}}{\rho_0}$	phase density contrast	0.1	–
T_{ph}	Reference temperature phase trans.	2073	K
P_{ph}	Reference pressure phase trans.	2.5×10^{10}	Pa
C	Composition parameter		–
$\frac{\delta\rho_C}{\rho_0}$	Compositional density contrast		–
ΔT	Temperature scale	4000	K
$T = T_S + T'\Delta T$	Temperature		K
T_S	Surface temperature	273	K
T^0_{CMB}	Initial core temperature	4273	K
t	Model time		s
ρ	Density		kgm^{-3}
ρ_0	Density scale	4500	kgm^{-3}
c_P	Specific heat	1.25×10^3	$Jkg^{-1}K^{-1}$
g	Gravitational acceleration	10	ms^{-2}
z	Depth coordinate		m
h	Mantle depth	2.885×10^6	m
k	Thermal conductivity	5	$Wm^{-1}K^{-1}$
$\kappa = \frac{k}{\rho c_P}$	Thermal diffusivity	8.89×10^{-7}	m^2s^{-1}
$\Phi = \eta e^2$	Viscous dissipation function		–
$e = (\frac{1}{2}e_{ij}e_{ij})^{1/2}$	Second invariant strain rate tensor		s^{-1}
u	Convective flow velocity		ms^{-1}
$\tau_{ij} = \eta e_{ij}$	Viscous stress tensor		Pa
$Ra = \frac{\rho_0\alpha_0 g\Delta T h^3}{\kappa_0\eta_0}$	Rayleigh number	1.9×10^8	–
$Rb_C = \frac{\delta\rho_C g h^3}{\eta_0\kappa_0}$	Compositional Rayleigh number		–
$Rb_{ph} = \frac{\delta\rho_{ph} g h^3}{\eta_0\kappa_0}$	Phase Rayleigh number	2.47×10^8	–
$Di = \frac{\alpha_0 g h}{c_P}$	Dissipation number	0.46	–
$R = \frac{H_0 h^2}{c_P\kappa_0\Delta T}$	Internal heating number	30.89	–
$H(t) = H_0\exp(\frac{-t\ln 2}{\tau_{1/2}})$	Time-dependent internal heating		Wkg^{-1}
H_0	Initial internal heat production	17.411×10^{-12}	Wkg^{-1}
$\tau_{1/2}$	Radioactive half-life time	2.5×10^9	yr
$\alpha(z) = \frac{\alpha_0\Delta\alpha}{((\Delta\alpha^{1/3}-1)(1-z)+1)^3}$	Thermal expansivity		K^{-1}
α_0	Thermal expansivity scale	2×10^{-5}	K^{-1}
$\Delta\alpha$	Layer contrast thermal expansivity	0.2	–
$\eta(T,z) = \eta_0\exp(\ln(\Delta\eta_P)z' - \ln(\Delta\eta_T)T')$	Dynamic viscosity		Pas
η_0	Viscosity scale	5×10^{23}	Pas
$\Delta\eta_P$	Pressure related visc. contrast	20	–
$\Delta\eta_T$	Temperature related visc. contrast	100	–

Table 4.1: Symbol definitions of mantle convection parameter and parameter values for the models used in this chapter.

Symbol	Quantity	Value	Dimension
g	Gravitational acceleration		ms^{-2}
g_0	Gravitational acceleration scale	10	ms^{-2}
G_0	Gravitational constant	6.673×10^{-11}	$m^3kg^{-1}s^{-2}$
C	Spectral coefficient gravity potential		m^2s^{-2}
S	Spectral coefficient density anomaly		kgm^{-3}
$\Delta\rho$	Mass density perturbation		kgm^{-3}
ρ_0	Density scale	4500	kgm^{-3}
$\Delta\sigma$	Mass sheet density anomaly		kgm^{-2}
ΔN	Geoid anomaly		m
ΔU	Gravity potential anomaly		m^2s^{-2}
σ_{nn}	Normal stress		Pa
τ_{nn}	Normal deviatoric stress		Pa
ΔP	Dynamic pressure		Pa
h_b	Dynamic topography		m
λ	Wave-length		m
k	Wave number		$-$
n	Fourier index		$-$
ℓ	Spherical harmonic degree		$-$
z	Depth coordinate		m
r	Radial coordinate		m
Subscript	Meaning		
a	Anomaly		
b	Boundary topography		
s	'Static'		
S	Surface		
T	Temperature		
C	Compostion		
ph	Mineral phase transition		

Table 4.2: Model parameters and values specific for calculation of synthetic gravity signals.

Using $\Delta\rho_i = \rho_0$ for the density contrast is a reasonable approximation for the surface boundary (because the density of the atmosphere, ρ_{at}, is negligible compared to the solid Earth) and the CMB (because the density of the outermost core, ρ_c, is approximately twice as larger as that of the lowermost mantle). Mathematically, this is expressed as follows:

$$\begin{aligned} \Delta\rho_S &= \rho_m(r_S) - \rho_{at}(r_S) \approx \rho_0 \\ \Delta\rho_{CMB} &= \rho_c(r_{CMB}) - \rho_m(r_{CMB}) \approx \rho_0, \end{aligned} \tag{4.7}$$

with ρ_m the mass density of the mantle and ρ_0 the reference density used in the models ($4500\ kgm^{-3}$).

From the virtual boundary topography, h_b, the associated boundary mass load, $\Delta\sigma_b$, is calculated as follows:

$$\Delta\sigma_b = \Delta\rho h_b. \tag{4.8}$$

From the mass load $\Delta\sigma_b$ the geoid anomalies are calculated in a similar way as the static geoid contribution. We use Poisson's equation (4.3) to solve the gravity potential, and subsequently use Bruns Theorem (Eq. (4.4)) to calculate the geoid anomaly ΔN_b. Finally, the total geoid anomaly is calculated by summation of the static and topographic contributions, using Eq. 4.1.

We apply the method described above to a broad range of thermo-chemical mantle convection models to assess the gravity expresssion of compositionally distinct material in the Earth's mantle. We investigate the effects of different degrees of stability of a compositionally distinct reservoir and convective layering at the transition zone by varying the compositional excess density and the Clapeyron slope of the endothermic phase transition near 660 *km* depth (see Table 4.3).

4.3 Results

4.3.1 Gravity expressions of a compositionally distinct mantle reservoir

Description of dynamic behaviour We examine the gravity field expression of convection models of progressively increasing stability conditions of a compositionally distinct reservoir, i.e. models R00, R10, and R15 with compositional excess density $\delta\rho_C/\rho_0 = 0$, 1, and 1.5%, respectively (see Table 4.3). All other parameters are kept constant and are listed in Table 4.1. For each of the models R00, R10, and R15, the convective state is shown at a representative model time in Figure 4.1.

In all three models, convective downwellings (for instance labeled 'd1' and 'd2' in frame (b)) are directly linked to geoid undulations and surface dynamic topography. The downwellings are expressed as low temperature anomalies (Figure 4.1b,e,h) and a density anomaly of approximately 1% (Figure 4.1c,f,i).

The phase transition acts as a partial barrier to the convective flow, depending on the Clapeyron slope γ and density contrast $\delta\rho_{ph}/\rho_0$. This results in an intermittent style of mantle convection (e.g. Machetel and Weber (1991)): periods of (local) ponding of downwellings (Figure 4.1e, arrow labeled 'p') alternate with cold downwellings that (locally) 'flush' the lower mantle (Figure 4.1b, arrow labeled 'd2'). Figure 4.1c,f,i shows a narrow depth interval of large density anomalies near 660 *km* depth. They reflect topography at the phase boundary, where the density increases by $\delta\rho_{ph}/\rho_0 = 10\%$. Generally, topography of the endothermic phase transition results in density anomalies that are opposite to the surrounding thermal density anomalies. This effect is indicated by the inverted colours in Figure 4.1 (right-hand column).

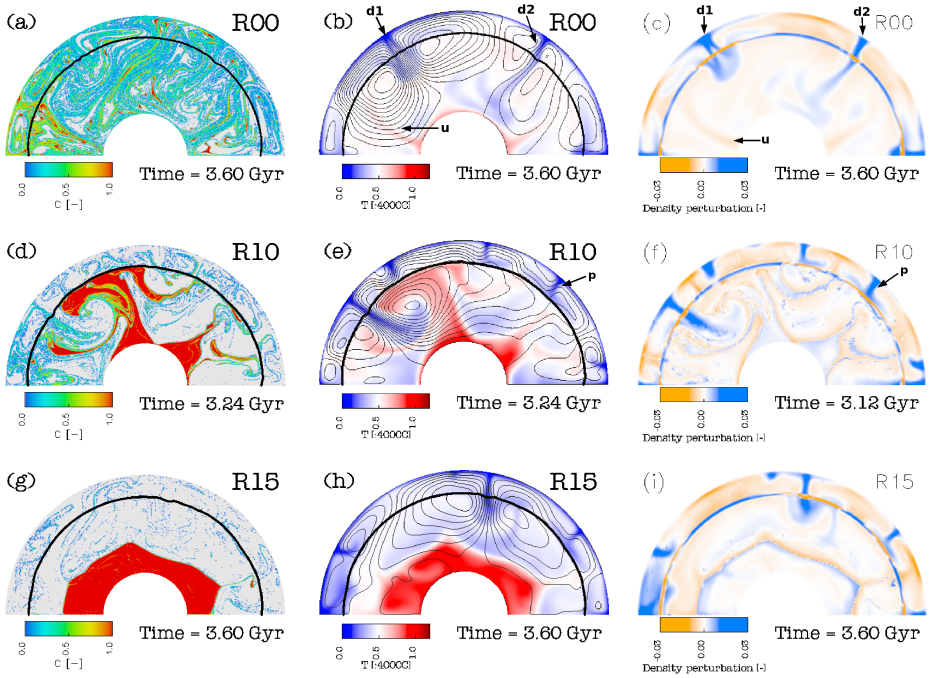

Figure 4.1: The left-hand, middle and right-hand column show the composition, temperature, and total density anomaly field, respectively. Thin black lines are stream lines, and the thick black line indicates the location of the endothermic phase transition. The top, middle and bottom row show the results for models with a distinct reservoir of subsequently increasing excess density of $\frac{\rho_C}{\rho_0} = 0\%$ (R00), $\frac{\rho_c}{\rho_0} = 1\%$ (R10), and $\frac{\rho_c}{\rho_0} = 1.5\%$ (R15). Model times are as indicated.

Model	Excess density $\frac{\delta\rho_C}{\rho_0}[\%]$	Clapeyron slope $\gamma[MPaK^{-1}]$	A_{ph+C} $[-]$	A_{ph} $[-]$	A_C $[-]$
R00	0.	-2.5	0.656	0.656	1.000
R10	1.	-2.5	0.266	0.642	0.374
R15	1.5	-2.5	1.077	0.566	1.505
G000	1.	0.	0.687	1.00	0.687
G125	1.	-1.25	0.958	1.039	0.843
G375	1.	-3.75	0.189	0.599	0.494

Table 4.3: Model parameters and values. Norm ratios of the geoid signal, A_α, for the different models at model times as indicated in the text. The ratios are defined as $A_\alpha = ||\vec{f}_T + \vec{f}_\alpha||/||\vec{f}_T||$, with $\vec{f}_T$ the thermal contribution to the static signal and $\vec{f}_\alpha$ the contribution of the phase transition ($\alpha = ph$), composition ($\alpha = C$) or both ($\alpha = ph+C$). The L2 vector norm is defined as $||\vec{f}|| = \left[\sum_{i=1}^{n} f_i^2\right]^{1/2}$, where the f_i are the surface nodal point values of the computed geoid signal.

Figures 4.1a,d,g show the composition distribution of models R00, R10, and R15, respectively. In the neutrally buoyant model (R00, Figure 4.1c), the (initially) deep reservoir has become dispersed throughout the mantle domain after a model time of 3.6 *Gyr*, as a result of passive mixing. Upwellings have a purely thermal origin, characterised by negative density anomalies, of which an example is shown in Figure 4.1b (arrow labeled 'u').

In general, adding a compositionally distinct reservoir to the system promotes a convective planform that is characterised by long wave-length convective flow (e.g. Tackley (2002)). Figure 4.1d shows the model of intermediate reservoir stability conditions (R10, $\delta\rho_C/\rho_0 = 1\%$), where large-scale compositional anomalies rest on the CMB, collect in mantle upwellings, or reside underneath the phase transition. Figure 4.1f shows that a net density anomaly in thermo-chemical upwellings below 0.5% results from the opposite effects of thermal and compositional density anomalies.

For the model with relatively stable reservoir conditions (R15, $\delta\rho_C/\rho_0 = 1.5\%$) Figure 4.1g shows that the distinct reservoir is configured as a layer that encloses the core on a global scale. In the mid-lower mantle, the interface between the reservoirs undulates as a result of convective motion, which induces lateral density anomalies of around 1.5% as is shown in Figure 4.1i. Above and below the interface, the mantle is close to an iso-compositional entity.

Static geoid undulations The individual contributions to the static geoid signal with an origin in temperature, mineral phase, and composition variations are depicted in Figure 4.2a, b, and c, respectively, for representative snapshots shown in Figure 4.1. Frame (d) shows the total static geoid signal. In all cases analysed, the largest contribution to static geoid undulations is associated with temperature variations (Figure 4.2a). Convective downwellings in the upper mantle are associated with prominent static geoid highs, indicated by the arrows labeled 'd1' and 'd2' in Figure 4.1b,c, and 4.2.

Long wave-length thermal geoid signals result from hot regions in the lower mantle, corresponding to the presence of a compositionally distinct reservoir, in which a temperature contrast with the overlying mantle has developed over billions of years. An example of massive high temperature thermo-chemical upwelling in the lower mantle is shown in Figure 4.1e. The correponding static geoid low of approximately 1 *km* is shown between angular coordinates 90-140^o in Figure 4.2a (green curve).

Figure 4.2 shows the total static geoid resulting from superposition of individual contributions of both positive and negative sign. As a consequence of this, the dominant thermal component can be significantly weakened by the contribution of the component associated with compositional or phase variations. In order to quantify the 'interference effect' of the different contributions to the geoid, we have investigated the 'signal power' defined by the L2 vector norm of the different geoid components

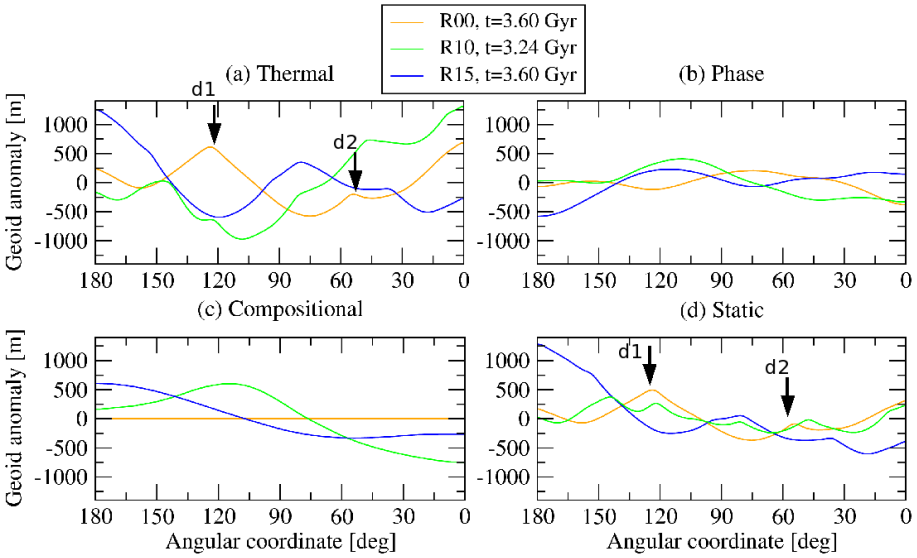

Figure 4.2: Geoid anomalies for models R00 (orange curves), R10 (green curves), and R15 (blue curves). The decomposed contributions to the static geoid that are related to variations are given in (a) temperature, (b) mineral phase, and (c) composition. Frame (d) shows the total static geoid anomalies.

using the following ratio

$$A_\alpha = \frac{||\vec{f}_T + \vec{f}_\alpha||}{||\vec{f}_T||} \tag{4.9}$$

where $||.||$ denotes the euclidean vector norm. Vector $\vec{f}_\alpha$ represents the surface nodal point vector of different combinations of geoid components; $\vec{f}_T$ thermal, $\vec{f}_{ph}$ mineral phase, $\vec{f}_C$ compositional, and $\vec{f}_{ph+C} = \vec{f}_{ph} + \vec{f}_C$. The power ratio decreases from a unit value for negligible $\vec{f}_\alpha$ to zero for complete cancellation of the thermal signal $\vec{f}_T$ by the signal $\vec{f}_\alpha$. Numerical values of A_α are listed in Table 4.3 for the different model snapshots of Figure 4.1, 4.2.

For the model with intermediate compositional density contrast (R10) intrinsically dense material preferentially collects in hot upwellings that are triggered by convective downflow during episodic mantle flushing events and rise to the top of the lower mantle. The geoid contribution caused by compositional heterogeneities significantly reduces the thermal contribution (Figure 4.2a,c, green curves). Table 4.3 shows that the thermal signal is reduced by as much as 63% ($A_C = 0.37$). In a similar way, the density anomalies –and hence geoid anomalies– associated with the phase boundary topography near 660 *km* depth are of opposite sign compared to the

local temperature anomalies, due to the negative Clapeyron slope of -2.5 $MPaK^{-1}$. The geoid contributions of opposite sign are expressed in a power reduction of 36% ($A_{ph} = 0.64$) and 73% ($A_{ph+C} = 0.27$) in combination with the composition effect.

Gravity expression of thermo-chemical anomalies in the shallow lower mantle The sensitivity of the geoid to density anomalies strongly decreases with increasing depth of the anomalies (Richards and Hager (1984)). Here, we compare the gravity expression of density anomalies of thermal, compositional, and phase origin at different mantle depths in the convection model. Figures 4.3a,b shows spatial and spectral respresentations of contributions to the geoid from density anomalies at different locations in the mantle domain. The contributions are compared for density anomalies of model R10, shown in Figure 4.1f. The contributions of dynamic topography of the surface boundary and the CMB are shown in the top and bottom bars, respectively. Not interpreted are the absolute magnitudes of Figure 4.3 that depend on the domain resolution. Contrasting colours in frame a show that geoid contributions that are related to boundary deflection (top bar) and of opposite sign to contributions of the uppermost mantle. Similarly, geoid anomalies associated with phase boundary topography around 660 *km* depth are opposite in sign to the surrounding density anomalies that are mainly thermal in origin. Figures 4.3a,b show that the contribution to the gravity potential of lower mantle origin is small and confined to long wavelength signals ($n < 4$). This follows from the decreasing sensitivity of the gravity potential to density contrasts with increasing wave number and depth (Richards and Hager (1984)).

To illustrate the depth of origin of the surface gravity contributions the geoid anomaly density per vertical *km* for each of the 65 mass sheets is shown in Figure 4.3c. The high amplitude, localised contribution that results from the phase boundary topography is shown by the blue curve. Thermal and compositional contributions to the static geoid signal (red and green curves) originate primarily from the top 1200 *km* of the mantle. In the lower mantle, the thermal contribution is substantial only in regions of large compositional heterogeneity, i.e. around 660-1200 *km* depth.

Figure 4.3d shows the variance reduction A_α (Eq. 4.9) of the thermal geoid component as a function of depth. The blue curve shows the localised effect of phase boundary topography. The green curve shows that the compositional contribution to the geoid reduces the thermal signal by approximately 80% in the shallow lower mantle (700-1400 *km*), where compositionally dense material resides below the endothermic phase transition. High values occur around a depth of 1500-2200 *km*, where temperature-related density variations are small compared to compositional density variations. Around 2200-2600 *km* is another region where thermal and compositional effects largely cancel, as indicated by the low A_C-values. Density anomalies situated at this depth do not contribute substantially to the geoid, however (Figure 4.3c, red and green curve).

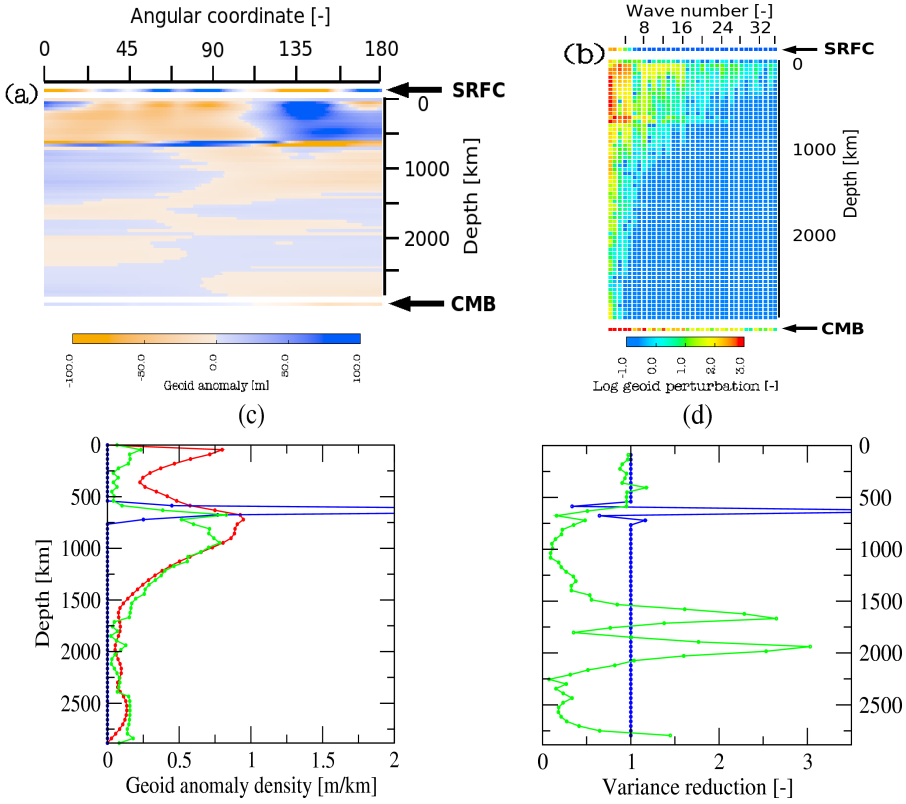

Figure 4.3: (a) Contributions to the geoid associated with density anomalies for model R10 (Figure 4.1f), shown as a function of the angular (horizontal) coordinate and (vertical) depth. The contribution of dynamic topography of the surface boundary and CMB are shown by the top and bottom bar, respectively. (b) Spectral representation of the contributions to the geoid of model R10 (shown in frame a) for the first 32 horizontal wave numbers as a function of (vertical) depth. Contributions from the top and bottom boundary dynamic topography are plotted as offset lines. (c) Depth profiles of different contributions to the static geoid for model R10 at model time $t = 3.24Gyr$. Shown is the geoid anomaly density per km in the vertical direction, i.e. RMS values of the geoid anomalies. Indiviual mass sheets are shown as dots. Red, blue, and green curves refer to static geoid contributions resulting from variations in temperature, mineral phase, and composition, respectively. (d) The variance reduction (see text for definition) of the thermal geoid contribution by effects of composition (green curves) and phase transition topography (blue curves).

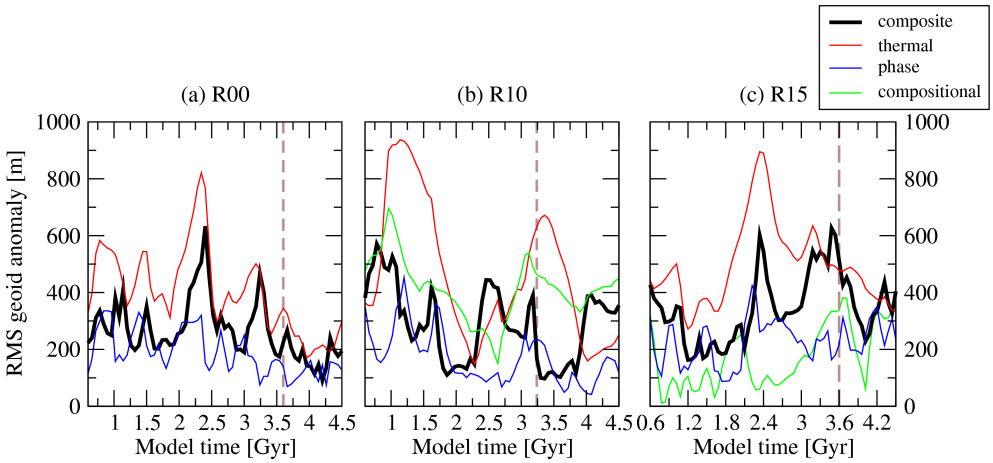

Figure 4.4: Time series of RMS values static geoid undulations. The black curve represents the total static geoid signal, and thermal, phase transition topography, and compositional contributions are represented by the Black, red, blue, and green curves, respectively. Frame a, b, and c show models R00, R10, and R15, resepctively. The brown dashed lines correspond to model times of the presented convection models discussed in the text and shown in Figure 4.1.

Time dependence To reveal the relationship between the different components of the static geoid through time we show time series of the RMS values of individual and total static geoid signals (Figure 4.4).

For the iso-chemical case (frame a) the thermal and total static geoid show a high correlation. In the absence of a composition-related geoid component, only the component related to the endothermic phase boundary topography counteracts the thermal signal.

For the thermo-chemical piles model R10 (frame b) the snaphot results at $t = 3.24 Gyr$ (Figure 4.1 and 4.2) sample a period of larger geoid contributions of both thermal and mineral phase origin (red and blue curves, respectively). The phase and compositional contributions counteract the thermal signal, which results in a significant power reduction of the total static geoid, indicated by the black curve.

For the model where the heterogeneous material forms a continuous layer (R15), lateral variations in composition are confined to a narrow depth range deep in the mantle. Frame c shows that this results in significantly smaller geoid contributions with a compositional origin, compared to the R10 model. Another contrast with model R10 is that thermal contributions are not necessarily counteracted by compositional contributions, but can also be reinforced. The deep compositional heterogeneities in the layer model are located away from the temperature variations associated with con-

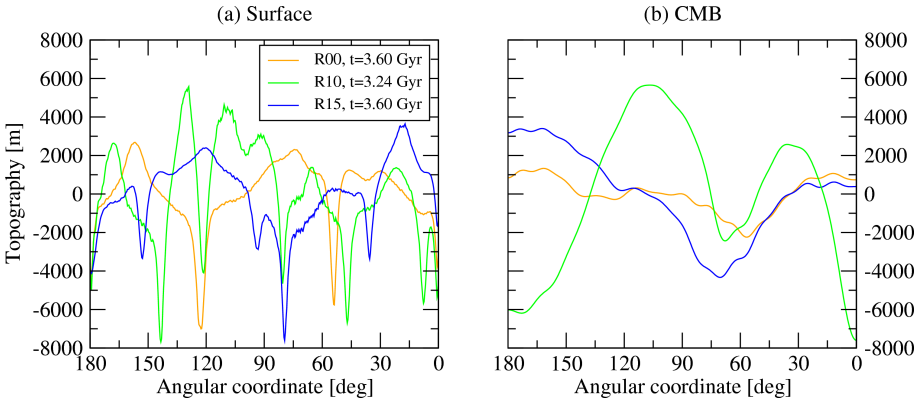

Figure 4.5: Dynamic topography for models R00, R10, R15 (orange, green, and blue curves, respectively) at model times as indicated in Figure 4.1. (a) Surface dynamic topography, (b) CMB dynamic topography.

vective downwellings in the upper mantle. Naturally, the coupling of the thermal and compositional contributions to the static geoid is lower than for the thermo-chemical piles model R10. An example is the 50% increase ($A_C = 1.5$ in Table 4.3) of the thermal contribution by compositional effects for model R15 for snapshot time $t = 3.6Gyr$ (Figure 4.1, 4.2).

Boundary topography and dynamic geoid undulations We present the predicted dynamic surface topography and CMB topography in Figure 4.5a,b for the same model snapshots as shown in Figure 4.1. Cold downwellings are represented by strong local depression of the surface boundary. An example is shown by the labels 'd1' and 'd2' for the R00 model in Figure 4.2 that facilitates comparison with Figure 4.1, 4.2.

Figure 4.5b shows the CMB topography for the different models. Dynamic topography of the CMB has similar amplitude compared to the surface boundary (frame a) but it is dominated by longer wave-length that reflects the broad-scale convective flow in the deep mantle (Figure 4.1e). The impact of dynamic topography of the CMB on the geoid is less than 10% of that of the surface boundary. In general, the CMB topography if positive (uplift) at deep mantle upwellings and negative (depression) below downwellings. Even when large-scale piles of dense material load the CMB (model R10): the most negative CMB topography is below cold downwellings of high viscosity, which is consistent with Lassak et al. (2007).

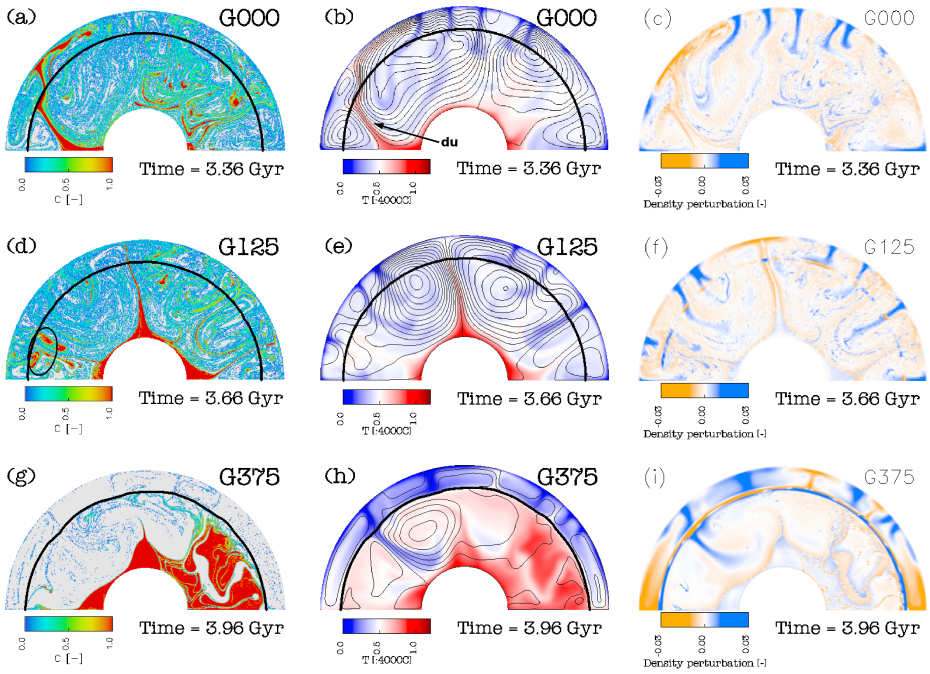

Figure 4.6: The left-hand, middle and right-hand column show the composition, temperature, and total density anomaly fields. Thin black lines are stream lines, and the thick black line indicates the location of phase transition. The top, middle and bottom row show the results for models with subsequently increasing Clapeyron slope magnitudes of $\gamma = 0 MPaK^{-1}$ (G000), $\gamma = -1.25 MPaK^{-1}$ (G125), and $\gamma = -3.75 MPaK^{-1}$ (G375), respectively. Model times are as indicated.

4.3.2 The influence of the Clapeyron slope of the 660 km phase transition

We investigate the influence of convective layering at the phase boundary on geoid undulations using a series of models with different values of the Clapeyron slope γ of the endothermic phase transition. The models presented here comprise three variations with respect to the reference model R10 with a Clapeyron slope of $\gamma = -2.5 MPaK^{-1}$ that was discussed in Section 4.3.1 (Figure 4.1, top row). A zero-value Clapeyron slope is applied in model G000, the Clapeyron slope has a small value of $\gamma = -1.25 MPaK^{-1}$ in model G125, and an increased value of $\gamma = -3.75 MPaK^{-1}$ is used in model G375 (see Table 4.3). All other model parameters are kept the same as in the reference model R10. The convective state for model G000, G125 and G375 is shown in Figure 4.6 at model times $t = 3.36$, 3.66, and $3.96 Gyr$, respectively.

Phase transition topography progressively increases for the models with larger

Clapeyron slope magnitude. This is illustrated by the RMS values of the transition zone topography, which increases from 0, to 7.8, 22.6, and 34.8 *km*, for models G000, G125, R10, and G375, respectively. Figures 4.1f and 4.6c,f,i graphically show the corresponding increase in density anomalies around the depth of 660 *km*, that are related to the phase boundary topography.

The left-hand column of Figure 4.6 shows that the survival of the distinct reservoir is promoted for progressively larger Clapeyron slope magnitudes, which is consistent with our previous modelling results for cartesian geometry (Van Thienen et al. (2005)). This result is explained by the increased resistance to convective downwellings at the endothermic phase transition, which promotes ponding of downwellings at the base of the upper mantle (e.g. Bercovici et al. (1993)). As a result, the frequency at which downwellings sink into the lower mantle decreases, which reduces mixing of the compositionally distinct reservoir.

Furthermore, for larger Clapeyron slope magnitude, the resistance to convective upwelling increases and deep-seated upwellings enter the upper mantle with a decreased frequency for models G000, G125, R10, and G375, respectively. As a result, the amount of compositionally distinct material contained in deep-seated upwellings injected into the upper mantle decreases with increasing Clapeyron slope magnitude (Chapter 3 this thesis). An example of a deep-seated upwelling, in which a substantial amount of intrinsically dense material is contained, is shown by the arrow labeled 'du' in Figure 4.6b for the model with zero Clapeyron slope. In contrast, the elliptic region in Figure 4.6d shows an example of an upwelling from which compositionally distinct material was filtered from mass transport into the upper mantle and that now resides underneath the phase transition of intermediate Clapeyron slope value.

Figures 4.6g,h show that for the model with increased Clapeyron slope magnitude (G375), large regions of low temperature reside in the lower mantle, which are the remnants of catastrophic flushing events. After such events, hot, compositionally distinct material is swept up underneath the phase boundary, heating the upper mantle from below. A process of thermal coupling of the convective flow, as described in e.g. Čížková et al. (1999), results in large-scale mantle upwellings characterised by high amplitude surface dynamic uplift. An example is depicted in Figure 4.6h at angular coordinate 0-30^o, showing upper and lower mantle convection cells circulating in opposite directions. A hot upwelling rising from the 660 *km* phase boundary is clearly shown as a low density anomaly in Figure 4.6i.

Expressions in the geoid Calculated geoid undulations for the models with varying Clapeyron slope magnitude are shown in Figure 4.7 (the large geoid anomalies of model G375 are left out of this figure). Figure 4.7b shows an increase of geoid undulations associated with phase boundary topography at progressively larger Clapeyron slope magnitudes for model G000, G125, and R10, respectively (red, black, and green

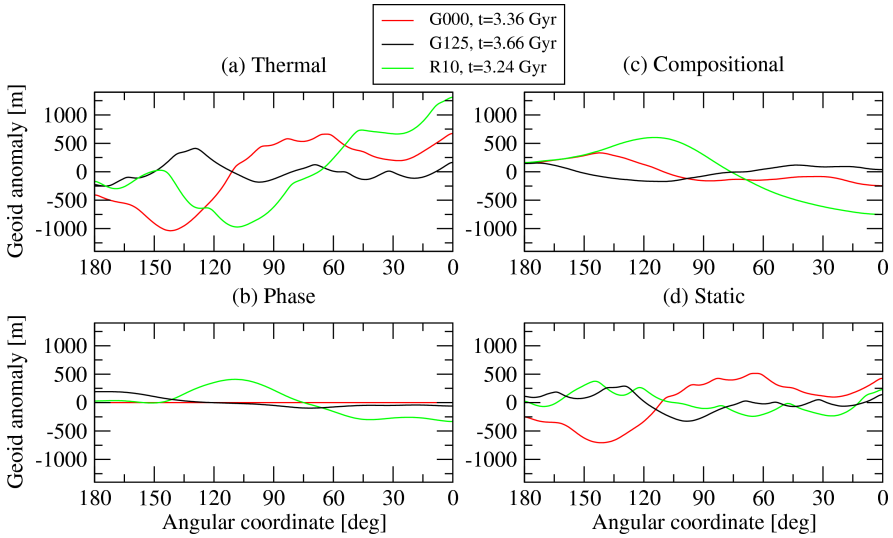

Figure 4.7: Geoid anomalies for models G000 (red curves), G125 (black curves) and R10 (green curves). The decomposed contributions to the static geoid that are related to variations are given in (a) temperature, (b) mineral phase, and (c) composition. Frame (d) shows the total static geoid anomalies.

curves). As a result, the reduction of geoid signals of thermal origin increases, which promotes lower static geoid signals. This is illustrated by the power ratio values A_{ph} in Table 4.3 that show an increased reduction of the thermal component of the static signal from 0 to 40% ($A_{ph} = 1.00 - 0.60$) for models of subsequently larger Clapeyron slope magnitude.

The rate of compositional homogenisation reduces for models of subsequently stronger degrees of convective layering at the transition zone, as was shown in Figures 4.6a,d,g. As a consequence, static geoid undulations of compositional origin increase in model G000, G125, and R10, as is shown in Figure 4.7b. In general, strong convective layering at the phase transition results in a stronger reduction of the static geoid signal of thermal origin. This is reflected by a large reduction of 51% and 63% for model G375 and R10 ($A_C = 0.49, 0.37$, respectively in Table 4.3). In contrast, model G125, in which the mantle is to a large degree compositionally homogenised at $t = 3.66 Gyr$, shows a comparatively small reduction of 16% ($A_C = 0.84$). Thus as a general rule, the modelling results show that strong convective layering at the endothermic phase transition near 660 km depth results in a significantly reduced static geoid signal. The controlling mechanism in reducing the static geoid is by promoting the survival of compositional homogeneities, and to a lesser extent by the increased phase boundary topography.

The model with zero Clapeyron slope (G000) does not follow the above trend, and shows a relatively strong reduction of 31% of the thermal component of the static geoid by compositional effects ($A_C = 0.69$ in Table 4.3). The large reduction results from deep-seated upwellings that enter the upper mantle at a relatively high frequency in the absence of any resistance from the phase boundary. A typical example is shown by the arrow labeled 'du' in Figure 4.6b. The upwellings of deep origin contain compositionally distinct material, which regionally (between $\phi = 120 - 160^o$) causes the strong reduction of the static geoid signal of thermal origin. For larger Clapeyron slope magnitude, deep-seated thermo-chemical upwellings occur less frequent and intrinsically dense material is efficiently removed from the upwellings by the process of chemical filtering at the endothermic phase transition (Chapter 3 this thesis). The removal of the compositional component in deep-seated upwellings reinforces the static geoid high over upwellings.

4.4 Discussion and conclusions

In this Chapter, we tested if it is possible to discriminate between mantle convection models with large-scale compositional heterogeneity and iso-chemical models on the basis of long wave-length gravity signals. By predicting static geoid undulations for a broad range of evolutionary thermo-chemical mantle models we extended previous work that considered the gravity expression of large-scale compositional heterogeneity in forward models (e.g. Čížková and Matyska (2004)). The models that we tested are the type of convection model that have been proposed to integrate geochemical and seismological observational data (e.g. Kellogg et al. (1999); Becker et al. (1999); Hansen and Yuen (2000)).

The limitations in predicting the dynamic topography in forward numerical models prevent a quantitative comparison of the calculated total geoid with the observations. Forward models generally calculate larger magnitudes for global surface dynamic topography undulations (e.g. King and Hager (1994); Kiefer and Kellogg (1997); Yoshida (2004); Lassak et al. (2007)) than estimates based on observations that have an amplitude of 100 m's to a few km's (e.g. Gurnis (1993); Panasyuk and Hager (2000b); Sandiford (2007)). Dynamic boundary topography overestimation is related to several limitations of the models. We performed additional experiments to test the sensitivity of the dynamic topography to the viscosity in the asthenosphere, lower mantle viscosity, and Rayleigh number. The modelling results demonstrate that controlling the dynamic topography is not straightforward, because its sensitivity to the model parameterisation is length-scale dependent. Our results confirm results of purely thermal, single cell convection experiments by Kiefer and Hager (1992). We acknowledge that there can easily be a bias of the dynamic topography in our forward geoid calculations, which prevents a quantitative comparison of the synthetic total geoid with the observations. Therefore, in the analysis of the results we focussed on

static geoid effects, rather than on the dynamic topography or total geoid undulations.

Large geoid undulations of compositional origin up to 500 *m* are possible in our convection models as a result of compositionally distinct material residing underneath the endothermic phase transition near 660 *km* depth. In particular, our study shows the significant influence on the geoid of compositional heterogeneities in the shallow lower mantle, for which independent seismological evidence exists (e.g. Trampert and van der Hilst (2005)).

The implications of compositional heterogeneity in the shallow lower mantle for the total static geoid signal are not straightforward, however. Compositional heterogeneities, together with phase boundary topography, oppose thermal contributions to the static geoid. The model results show that a power reduction of 63% of the thermal component of the static geoid is possible for the piles model (R10) when compositional heterogeneities are strongly correlated with positive temperature anomalies in the shallow lower mantle. In contrast, the power of the thermal component of the static geoid is only slightly reduced, or even amplified for the model with a globally continuous compositional interface in the deep mantle (R15), for which the convective structure of the deep mantle and the upper mantle are strongly decoupled.

Our results show that strong convective layering at the transition zone promotes the survival of a compositionally distinct reservoir, which confirms results from previous numerical modelling experiments (Van Thienen et al. (2005)). As a result, the thermal contributions to the static geoid are strongly opposed by the presence of compositionally distinct material and this favours a strong power reduction of the static geoid signal. We conclude that reduction of the thermal contribution to the static geoid due to compositional heterogeneity in the shallow lower mantle is stronger than the effects of phase boundary topography, as described e.g. by Thoraval et al. (1995).

Geoid inversion studies predict a small contribution of buoyancy anomalies of compositional origin in the mantle, if any, compared to anomalies of thermal origin (Forte and Mitrovica (2001); Simmons et al. (2007)) and cannot rule out iso-chemical models (e.g. Čadek and Fleitout (2006)). It is not clear if this is compatible with suggestions of negative buoyancy in the LLSVPs, predicted by normal mode inversion (e.g. Ishii and Tromp (1999)). Compositional anomalies can be masked in seismic tomography from which density input models are inferred for geoid inversion studies. Therefore, on the basis of the geoid inversion models it is difficult to rule out models with a large contribution of compositional heterogeneity in the Earth's mantle.

Our modelling results suggest the feasibility of more prominent compositional heterogeneities in the lower mantle. The gravity expression of large amounts of compositionally distinct material is compensated by the effect of positive thermal anomalies, which have a larger magnitude for thermo-chemical than for iso-chemical convection models. As a consequence, the two alternative models are characterised by static geoid anomalies of similar amplitude, and a distinction between the models is difficult. In sharp contrast to significant differences in seismic signature, thermal and

compositional evolution, and present-day dynamics, we show that the static geoid expression of the two alternative mantle models is remarkably similar. Therefore, the existence of significant compositional heterogeneity in the lower mantle cannot be excluded on the basis of the gravity expression.

4.5 APPENDIX A: Description of geoid and dynamic topography calculation

The method of calculating geoid anomalies in thermo-chemical mantle convection models including phase transitions was briefly introduced in Section 4.2. Here, a more detailed description of the geoid anomaly calculation in cylindrical and cartesian geometry is given.

4.5.1 Geoid and dynamic topography calculation in cylindrical geometry

Boundary condition for Poisson's equation at a mass sheet To obtain a solution of the 2-D Poisson equation in the cylindrical coordinate system, we start by defining a boundary condition for Poisson's equation at the 2-D circular cylindrical mass sheet density anomaly $\Delta\sigma(\phi)$ located at $r = r_a$. Symmetry is assumed in the z-direction, perpendicular to the r,ϕ-plane ($\frac{\partial}{\partial z} = 0$). Applying the Gauss divergence theorem to the integral expression of Eq. (4.3) we get

$$\int_{\partial V} \nabla \Delta U \cdot d\vec{A} = 4\pi G_0 \int_V \Delta\sigma(\phi)\delta(r - r_a)dV, \tag{4.10}$$

which holds for a 2-D cylindrical box region with arbitrary finite dimension L_r, L_ϕ, centred at polar coordinates (r_0, ϕ_0). In the limit of vanishing radial thickness $L_r \to 0$, the contributions from the radial surfaces vanish, because the lateral derivatives of ΔU are continuous. The integral in the left-hand side of Eq. (4.10) reduces to $\lim_{L_r/2\to 0} \int_{S_{\phi z}} \left(\left[\frac{\partial \Delta U}{\partial r}\right]_{r_0+L_r/2} - \left[\frac{\partial \Delta U}{\partial r}\right]_{r_0-L_r/2} \right) r d\phi dr$. Since this holds for an arbitrary position (r_0, ϕ_0) and box length L_ϕ, we obtain the boundary condition for a mass sheet

$$\left[\frac{\partial \Delta U}{\partial r}\right]_-^+ = 4\pi G_0 \Delta\sigma(\phi). \tag{4.11}$$

Poisson's equation in 2-D cylindrical geometry A general solution of the Poisson Equation outside a mass sheet under consideration at radius r_a is found by setting the right-hand side source term in Eq. (4.3) to zero. We obtain the Laplace equation, which in the cylindrical coordinate system reads

$$\frac{\partial^2 \Delta U}{\partial r^2} + \frac{1}{r}\frac{\partial \Delta U}{\partial r} + \frac{1}{r^2}\frac{\partial^2 \Delta U}{\partial \phi^2} = 0. \tag{4.12}$$

Using separation of variables, $\Delta U(r,\phi) = R(r)\Phi(\phi)$, Eq. (4.12) becomes

$$\frac{1}{R}\left(r^2\frac{d^2R}{dr^2} + r\frac{dR}{dr}\right) + \frac{1}{\Phi}\frac{d^2\Phi}{d\phi^2} = 0. \tag{4.13}$$

Imposing 2π periodicity on the solution in ϕ, we choose $-n^2$ for the last term on the left-hand side of Eq. (4.13). Switching to a dimensionless radius $r' = r/r_a$, with r_a the radius of the mass sheet, and using the substitution $r' = e^t$ we obtain

$$\frac{d^2R}{dt^2} - n^2R = 0. \tag{4.14}$$

The characteristic equation of Eq. (4.14) is $\lambda^2 - n^2 = 0$ with distinct roots $\lambda = \pm n$ for $n > 0$. The case with a single root, $n = 0$, corresponds to cylindrical symmetry ($\partial/\partial\phi = 0$). The symmetrical part of the potential does not contribute to the lateral potential anomalies, defined in the convection models. A cylindrically symmetrical solution leads to simple analytical solutions that can be used in benchmarking computer codes.

For $n = 0$, two independent solutions of Eq. (4.14) are

$$R_{0\pm}(r') = \begin{cases} B_{0+}\ln(r') & ,r' > 1 \\ B_{0-} & ,r' \leq 1 \end{cases} \tag{4.15}$$

From continuity of the potential $R_{0+} = R_{0-}$ at $r' = 1$, follows the condition $B_{0-} = 0$. To solve for the coeffficient B_{0+}, we use the boundary condition defined in Eq. (4.11). This results in $B_{0+} = 4\pi G_0 \Delta\sigma r_a$. Now that the coefficients in Eq. (4.15) are obtained, we can express the gravity potential as

$$\Delta U_{0\pm}(r) = \begin{cases} 4\pi G_0 \Delta\sigma r_a \ln(\frac{r}{r_a}) & ,r > r_a \\ 0 & ,r \leq r_a \end{cases} \tag{4.16}$$

Since the symmetric component is absent in the density anomalies, defined as lateral variations with respect to the angular average, we develop a general solution excluding the case $n = 0$. Zero mean combinations of logarithmic solutions of the static geoid undulation corresponding to 2-D point sources have been used to successfully benchmark the computer code.

To find the non-symmetric part, we solve Eq. (4.14) with $n \neq 0$ to obtain

$$\Delta U_{n\pm}(r,\phi) = R_{n\pm}e^{in\phi} = B_{n\pm}\left(\frac{r}{r_a}\right)^{\mp|n|} e^{in\phi} = \tag{4.17}$$

$$= \begin{cases} B_{n+}\left(\frac{r}{r_a}\right)^{-|n|} e^{in\phi} & ,r > r_a \\ B_{n-}\left(\frac{r}{r_a}\right)^{|n|} e^{in\phi} & ,r \leq r_a \end{cases}$$

Furthermore, the continuity at $r = r_a$ (i.e. $\Delta U_{0+} = \Delta U_{0-}$) constrains the spectral coefficients to $B_{n-} = B_{n+} = B_n$. To derive the coefficients B_n of the gravity potential, the boundary condition (Eq. 4.11) is applied. The left-hand side of Eq. (4.11) is

found by differentiation of Eq. (4.17) with respect to r. In the right-hand side of Eq. (4.11), we expand the density distribution in a Fourier series: $\Delta\sigma = \sum_{n\neq 0} S_n e^{in\phi}$. The result of the above operations gives the non-symmetric part of the gravity potential

$$\Delta U_{\pm}(r,\phi) = \sum_{n\neq 0} B_n \left(\frac{r}{r_a}\right)^{\mp|n|} e^{in\phi} = \sum_{n\neq 0} C_{n\pm} e^{in\phi} \tag{4.18}$$

with

$$C_{n\pm} = \frac{-2\pi r_a G_0}{|n|}\left(\frac{r}{r_a}\right)^{\mp|n|} S_n \quad , n\neq 0. \tag{4.19}$$

Computation of static geoid anomalies Static geoid anomalies are calculated from a set of mass sheet density anomalies, $\Delta\sigma_{lj} = \Delta\sigma(\phi_l, r_j)$, which are defined on an equidistant grid in polar coordinates. The grid is dimensioned $L_\phi \times L_r$, with $N_l \times N_j$ equidistant grid-points in the lateral and radial direction, respectively. Volumetric mass density anomalies $\Delta\rho(\phi_l, r_j)$ are converted to mass sheet anomalies $\Delta\sigma(\phi_l, r_j)$. Mass is conserved in this operation by defining $\Delta\sigma r_j \Delta\phi_j = \Delta\rho V_{cell}$, where the volume of the grid cell is given by $V_{cell,j} = [(r_j + \frac{\Delta r_j}{2})^2 - (r_j - \frac{\Delta r_j}{2})^2]\frac{\Delta\phi_l}{2}$. $\Delta\phi_j$ and Δr_j are the lateral and radial extent of the grid cell. This results in the following conversion relations

$$\Delta\sigma(\phi_l, r_j) = \begin{cases} \Delta\rho(\phi_l, r_j)\left[\frac{\Delta r}{2} - \frac{\Delta r^2}{8r}\right] & , j = 1 \quad , r = r_S \\ \Delta\rho(\phi_l, r_j)\left[\frac{\Delta r}{2} + \frac{\Delta r^2}{8r}\right] & , j = N_l \quad , r = r_{CMB} \\ \Delta\rho(\phi_l, r_j)\Delta r & , j \neq 1, N_l \quad , r_{CMB} < r < r_S \end{cases} \tag{4.20}$$

In cartesian geometry the grid is equidistant rectangular, with coordinates (x_l, z_j), dimension $L_x \times L_z$, and a number of $N_l \times N_j$ grid points. The z-direction is positive in the downward direction and zero at the top surface. Mass sheet density anomalies, $\Delta\sigma(x_l, z_j)$, are obtained from density anomalies using the Trapezium rule

$$\Delta\sigma(x_l, z_j) = \begin{cases} \Delta\rho(x_l, z_j)\frac{\Delta z_j}{2} & , j = 1, N_l \\ \Delta\rho(x_l, z_j)\Delta z_j & , j \neq 1, N_l \end{cases} \tag{4.21}$$

with Δz_j the local vertical grid spacing.

In the computation of the results presented in Section 4.3, we applied the following discretisation parameters: the number of angular points $N_l = 257$, the number of radial points $N_j = 65$. The number of spectral components equals the number of angular grid points in the Fourier transform.

The spectral coefficients of mass sheet density anomalies S_{nj} are obtained by applying a discrete Fourier transformation to individual rows of mass sheet density anomalies

$$S_{nj} = \sum_{l=0}^{N_l - 1} \Delta\sigma_{lj} e^{\frac{-i2\pi nl}{N_l}}, \tag{4.22}$$

with n the wave number index.

In cylindrical geometry, the spectral coefficients for the gravity potential are expressed in terms of S_{nj} for the individual mass sheets ar r_j by Eq. (4.18) and (4.23):

$$C_{nj} = \frac{-2\pi r_j G_0}{|n|} \left(\frac{r}{r_j}\right)^{-n} S_{nj}. \tag{4.23}$$

The gravity potential in the spatial domain of the mass sheet at r_j is obtained by inverse discrete Fourier transformation in the lateral direction:

$$\Delta U_{lj} = \frac{1}{N_l} \sum_{n=0}^{N_l-1} C_{nj} e^{\frac{i2\pi nl}{N_l}}. \tag{4.24}$$

The gravity potential anomaly resulting from mass anomalies distributed throughout the mantle domain is caclualted by summation of the contributions of the N_j individual mass sheets in the spectral domain

$$\Delta U_l = \frac{1}{N_l} \sum_{n=1}^{N_l-1} C_n e^{\frac{i2\pi nl}{N_l}}, \tag{4.25}$$

where $C_n = \sum_{j=1}^{N_j} C_{nj}$.

4.5.2 Geoid and dynamic topography calculation in cartesian geometry

In order to perform a benchmark comparison for the gravity field computation with available data from the literature (Blankenbach et al. (1989)), we have implemented similar computational schemes as described in the previous sections for models in 2-D cartesian geometry.

In this section, only the relevant differences between the geometries are discussed. The spectral coefficients of mass sheet density anomalies S_{nj} are obtained by discrete row-wise Fourier transformation in the lateral direction, using Eq. (4.22). In cartesian geometry the discrete Fourier coefficients of the gravity potential, C_{nj}, are written in corresponding spectral terms of the density of a single mass sheet, S_{nj}, as follows

$$C_{nj} = \frac{-2\pi G_0 S_{nj}}{k_n} e^{\mp k_n (z - z_j)}, \tag{4.26}$$

with $k_n = \frac{2\pi n}{\lambda}$ the wave number and λ the wave-length. Finally, the gravity potential ΔU is obtained by summation of C_{nj} of all mass sheets j to get C_n. To obtain the static gravity potential anomaly, ΔU_s, the inverse Fourier transform is applied

$$\Delta U_s(x,z) = \frac{1}{N_l} \sum_{n=0}^{N_l-1} C_n e^{\frac{i2\pi nl}{N_l}}. \tag{4.27}$$

Dynamic topography at the boundary surfaces, h_b^i is calculated from the normal stresses σ_{nn}, similar to the cylindrical case (Eq. 4.6). The dynamic surface load, defined as $\Delta\sigma_b = \rho_0 h_b$, is used to calculate the gravity potential ΔU_b. The total geoid anomaly is obtained using Eq. (4.1) and Brun's Theorem, (Eq. (4.4)).

Benchmark comparison for the gravity field computations, and filtering irregularities from the dynamic topography To validate the gravity calculations, we use the published 2-D cartesian convection benchmark of Blankenbach et al. (1989) (case 1a). This benchmark is suitable for our purpose as it was specifically designed for mantle convection problems and includes results for the geoid and dynamic topography. Figures 4.8a,b show the differences between the top corner points of the 2-D rectangular domain in geoid and dynamic topography, respectively. The result obtained using a moving average filter on the raw data of the computed boundary stresses (discontinuous curves) are converging with the published results (open circles) for sufficiently small size of the finite elements. This validates our code for calculating geoid undulations and dynamic topography.

In the finite element (FE) method used (Segal and Praagman (2000)) FE nodal point field values of derived quantities like stress tensor elements are averaged over adjacent finite elements. The standard averaging procedure results in small-scale noise-like irregularities of the pressure and velocity gradient fields, that appear to oscillate between FE vertices and mid-points. As a result, undesired irregularities are produced in the calculated dynamic topography. In order to remove the irregularities, an alternative regularisation method was implemented, using a variable degree of smoothing. In this approach, we project the field data calculated at FE nodal points on a structured grid, and subsequently apply spatial smoothing using a 2-D moving average filter method. The size of the smoothing window ellipse is determined by the horizontal and vertical radii that are defined in terms of a fraction f_{win} of the local FE element size. The discontinuous curves in Figure 4.8 show the results obtained using the moving average technique of subsequently larger smoothing windows (i.e. $f_{win} = 0$, 0.5 and 1.). For the cases tested, the results converge to similar values and similarly fast as the published data. The range covers the value $f_{win} = 0.6$ used to define the moving average window size in the convection results in this chapter. The benchmark results indicate that filtering applied to the convection models does not degrade the accuracy of the results significantly, whereas they are successful in removing irregularities that result from the standard averaging technique.

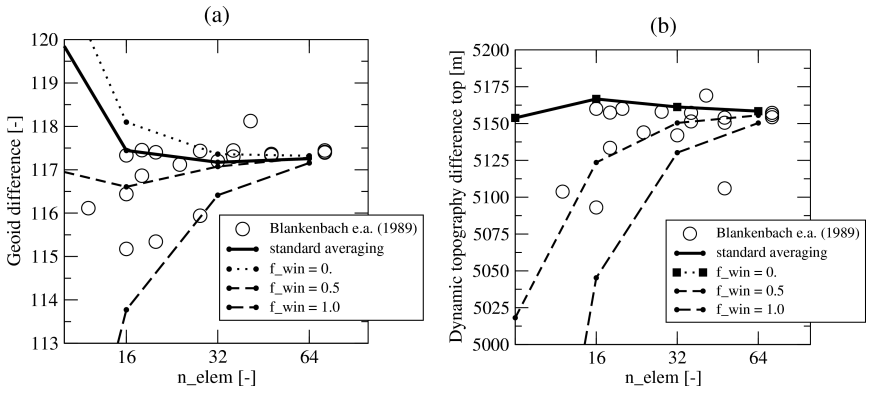

Figure 4.8: Convergence behaviour of cartesian convection benchmark for increasing number of finite elements in the horizontal direction of the 2-D rectangular domain (horizontal axis). Figures show the difference in values at the top corners of the models for (a) geoid and (b) dynamic topography. Open circles are published values from Blankenbach et al. (1989). Thick solid curves are for standard averaging technique. Discontinuous curves are for the moving averaging technique using an averaging window with radii f_{win} times the width of the finite element (see legend for values of f_{win}).

4.6 APPENDIX B: Benchmark comparison of geoid calculations in 2-D cylindrical and 3-D axisymmetric spherical geometry

In this appendix we describe a benchmark to compare geoid calculations in 2-D cylindrical geometry with calculations for corresponding density configurations in 3-D spherical geometry. The static geoid signal of an axisymmetric spherical mass sheet with a zonal surface harmonic distribution of surface mass density is compared to the geoid calculated for a corresponding cylindrical configuration. Differences are quantified as a function of depth of the mass sheet and wave-length of the surface density distribution.

The test mass sheet anomaly $\Delta\sigma$ at radius r_a is defined as a normalised zonal spherical harmonic function of degree j and order $m = 0$:

$$\Delta\sigma(r_a, \theta) = \Delta\sigma_0 P_j(\theta)\delta(r - r_a). \tag{4.28}$$

$\Delta\sigma_0$ is the amplitude of the mass sheet anomaly. The choice for a spherical harmonic function is motivated by the straightforward geoid calculation in spherical geometry. Whereas lines of equal latitude are circular in spherical geometry, in 2-D cylindrical geometry mass anomalies are extended to infinity in the direction perpendicular to the latitudinal and radial axis. The amplitude of the mass sheet anomaly is chosen arbitrarily as $\Delta\sigma_0 = 1 \times 10^6 kgm^{-2}$. Examples of the mass load anomalies for harmonic degree $j = 1 - 4$ are shown in Figure 4.9a-d. For cylindrical geometry, the lateral coordinate, ϕ, is aligned with the co-latitude θ ($\phi = \theta$).

For spherical geometry, the geoid anomaly is expressed in terms of spherical harmonic functions (e.g. Sleep and Fujita (1997), p. 490). For the mass load defined as a Legendre polynomial, the static geoid anomaly is given by

$$\Delta N_S(\theta, r_a) = \frac{4\Delta\sigma_0 \pi G_0 r_a}{(2j+1)g_0} \left(\frac{r_a}{r_{ev}}\right)^{j+1} P_j(\cos\theta), \tag{4.29}$$

Symbols are explained in Table 4.1.

In 2-D cylindrical geometry, geoid signals are computed in the spectral domain (see Appendix A). Spectral coefficients of the gravity potential, C_n, and mass load, S_n, are related by

$$C_n = \frac{-2\pi r_a G_0}{n} \left(\frac{r_a}{r_{ev}}\right)^n S_n. \tag{4.30}$$

The geoid signal is calculated by applying Brun's theorem (4.4) to the inverse Fourier transform of the gravity potential.

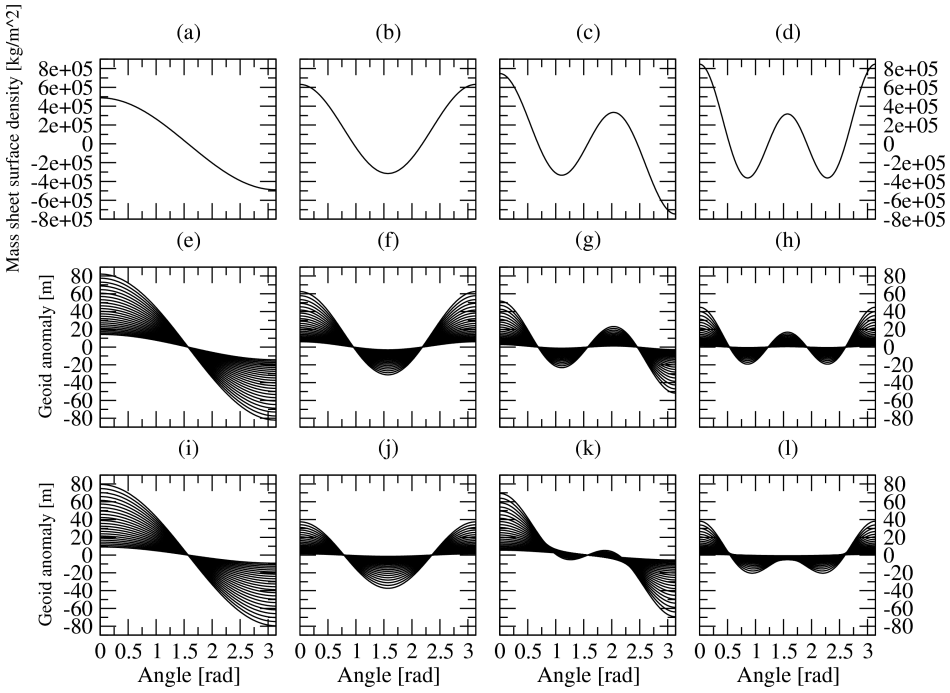

Figure 4.9: (a)-(d) Mass load as a function of the angular coordinate, for spherical harmonic degree 1-4 (as indicated). (e)-(h) Corresponding geoid anomalies in 3-D spherical geometry. (i)-(l) Corresponding geoid anomalies in 2-D cylindrical geometry. Multiple curves in frame (e)-(l) indicate results for mass sheets at 23 different depths. Curves with maximum amplitude are at a depth $h/24$, and curves of subsequently lower amplitude are at 22 equidistant depths throughout the depth range of the model.

The geoid signal corresponding to the mass load anomalies shown in Figure 4.9a-d are shown in Figure 4.9e-h and 4.9i-l, for spherical and cylindrical geometry, respectively. In each frame, geoid signals of subsequently decreasing amplitude correspond to increasing depths of the mass sheet at 23 equidistant intervals throughout the mantle domain. In addition to the depth-dependent damping, geoid signals decrease with decreasing wave-length (increasing degree j) in both geometries.

In spherical geometry, the geoid anomaly (Eq. 4.29) is described by a single Legendre polynomial of the same degree j as the mass load. In cylindrical geometry, however, the Legendre polynomial represented as a Fourier sepctrum of finite width. Because damping is stronger for small wave-length components in the calculation of the gravity potential, the geoid signals in cylindrical geometry are characterised by a large contribution of the long wave-lengths, compared to the mass loads (cf. Figure 4.9i-l and 4.9a-d).

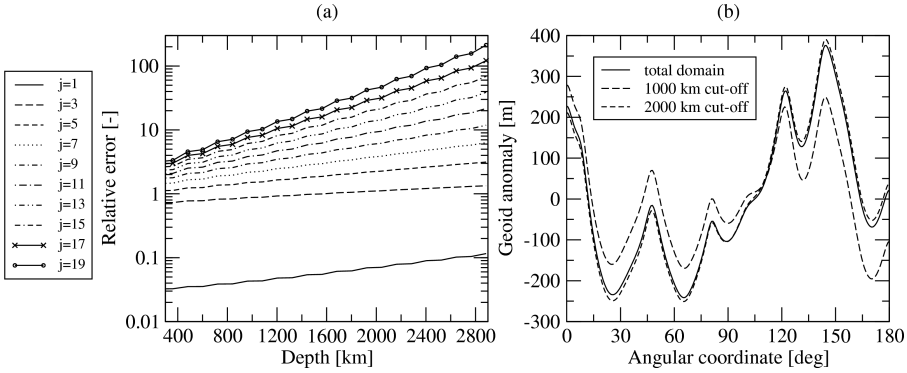

Figure 4.10: (a) The relative norm of the difference ε (see Eq. 4.31) for definition) of the geoid signal in 2-D cylindrical geometry as compared to 3-D spherical geometry. (b) Static geoid signal calculated from density anomalies in the entire domain (solid curve), and above a cut-off depth of 2000 *km* (dashed curve), and 1000 *km* (dotted curve).

We compare the obtained results for different harmonic degree and radius, for mass load anomalies of different harmonic degree j. To quantify the correspondence of geoid undulations in both geometries, we measure the relative norm of the difference ε of the geoid signal in 2-D geometry as compared to 3-D spherical geometry.

$$\varepsilon(j,r_a) = \left[\sum_{i=1}^{n}(\Delta N_s^{i,sph}(\theta_i,r_a))^2\right]^{-1}\left[\sum_{i=1}^{n}(\Delta N_s^{i,cyl}(\phi_i,r_a)-\Delta N_s^{sph}(\theta_i,r_a))^2\right]. \quad (4.31)$$

Figure 4.10a shows ε for different values of r_a and j. For a valid comparison, we only consider at the odd degrees, which have a zero average value in both geometries. The geoid signal is overestimated in cylindrical geometry and the relative error ε increases with increasing degree j and depth of the mass sheet. This is in accord with Eq. 4.29 and 4.30, that show a larger damping with depth in spherical geometry (the exponent of r_a is spherical harmonic degree $j+2$) than in cylindrical geometry (exponent is Fourier coefficient $n+1$). The correspondence between 2-D cylindrical and spherical geometry are best for the density anomalies for which the geoid is most sensitive, i.e. long wave-length, shallow anomalies.

To quantify the contributions of the deep mantle, the static geoid calculated from the entire mantle domain is compared to the geoid calculated using a cut-off depth of 1000 and 2000 *km*. For a representative model of thermo-chemical convection, Figure 4.10b shows the small contribution to the static geoid with an origin below 1000 and 2000 *km*. The respective L2 norm ratio $||\vec{f}_{cutoff}||/||\vec{f}_{wholedomain}||$ is 0.842 and 0.976. Nevertheless, the overestimation in cylindrical geometry becomes stronger for deep, short wave-length density anomalies. Geoid signals associated with small-scale, deep structure must therefore be interpreted with some caution.

Chapter 5

Constraints on thermo-chemical mantle convection from comparison of synthetic seismic velocity anomalies to seismological observables

5.1 Introduction

In the previous chapters we investigated the thermal and compositional heterogeneities associated with convective upwellings (Chapter 3) and their expression in the Earth's gravity field (Chapter 4). In this chapter, we calculate synthetic seismic velocity anomalies of thermo-chemical and iso-chemical convection models. The synthetic data is compared to seismological data –an important source of information for the mantle.

To investigate the convective regime of the mantle it is appropriate to focus on the deviations of seismic velocity from the lateral average, which are closely related to the driving forces of the convective flow. From previous studies on thermo-chemical mantle convection it was concluded that the agreement with seismological observations is better for models with large-scale thermo-chemical piles atop the CMB than for models of globally continuous thermo-chemical layering in the deep mantle (Tackley (2002); Deschamps et al. (2007)). It has remained difficult, however, to exclude purely thermal (iso-chemical) models on the basis of seismic velocity anomalies (Tackley (2002)) or to distinguish between different types of thermo-chemical convection (Nakagawa and Tackley (2004a)). A combined analysis of shear wave and bulk sound velocity anomalies can be expected to improve the constraints on com-

position because compositional anomalies leave an expression that is distinct from thermal anomalies in density and shear wave and bulk sound velocity (or shear wave and longitudinal velocity) (see Trampert and van der Hilst (2005) for an overview). Yet, such a combined analysis has not yet been done.

There are several seismological indications for lower mantle compositional heterogeneity. Large low shear velocity provinces (LLSVP) in the lowermost 1000 *km* of the mantle have been interpreted previously as positively buoyant "super plumes" of thermal origin (e.g. Romanowicz and Gung (2002); DePaolo and Manga (2003)). However, a negative correlation between shear wave and bulk sound velocities (Van der Hilst and Kárason (1999); Saltzer et al. (2001)), together with a higher-than-average density anomaly (Ishii and Tromp (1999)), is in fact a strong hint for compositionally distinct material in this region. In addition, a compositional origin has been suggested for the boundary interface of the African LLSVP, which appears to be sharper than expected from a thermally-induced gradient (Ni et al. (2002)). Finally, the behaviour of the ratio of shear wave over bulk sound velocity anomalies, defined as $R_{\phi/S} = \frac{\delta \ln v_\phi}{\delta \ln v_S}$, is discordant with a purely thermal origin. Positive values for $R_{\phi/S}$ are most likely associated with a thermal origin, and strongly negative values reported for the lowermost mantle likely arise from chemical heterogeneities (Saltzer et al. (2001); Karato and Karki (2001); Kennett and Gorbatov (2004)). The correlation function and the seismic ratio are useful diagnostics to study the origin of seismic velocity anomalies. A limitation is that they do not provide an unambiguous diagnostic for chemical heterogeneities because of trade-off effects between composition and temperature (Deschamps and Trampert (2003)).

A combined analysis of synthetic v_s and v_ϕ anomalies also allows for a more detailed study of the petrological origin of a compositionally distinct reservoir. Understanding the large-scale variations in lower mantle bulk composition is required to distinguish between different proposed formation scenarios for a compositionally heterogeneous mantle. Previously suggested formation processes of a compositionally distinct deep mantle reservoir are sinking of basaltic crust (Christensen and Hofmann (1994); Tolstikhin and Hofmann (2005); Van Thienen et al. (2005)), differential crystallisation from a magma ocean (e.g. Walter et al. (2004)), and interaction with the core (Jeanloz and Lay (1993); Mao et al. (2004)). The most obvious candidates to influence the lower mantle bulk composition are variations in iron and perovskite content and it has been suggested that both are required to explain density and seismic velocity systematics in the lower mantle (Kellogg et al. (1999); Trampert et al. (2004)). The influence of iron and perovskite on the combined shear wave and bulk sound velocity has not been analysed systematically in forward modelling studies based on thermo-chemical convection models.

The thermal and compositional evolution of the mantle is also linked to heterogeneities in the shallow lower mantle, which are important indicators for material and heat transport between the upper and lower mantle (Chapter 3, this thesis). Unfor-

tunately, tomographic imaging near the mantle transition zone is hampered by poor seismic resolution (Antolik et al. (2003)). The seismological data currently available cannot rule out substantial compositional heterogeneity in the shallow lower mantle (Trampert et al. (2004)). A discrepancy between observational evidence for a compositional heterogeneous shallow lower mantle and comparatively iso-chemical synthetic predictions was pointed out by Deschamps et al. (2007) and could be due to the absence of phase transitions in their model. Phase transformations in the transition zone influence the temperature and composition field in the shallow lower mantle by modulating thermo-chemical upwellings from the deep mantle (Chapter 3, this thesis). For a rigorous evaluation of the synthetic seismic signature to the observational data one must include solid-state phase transitions in the convection models. The need to include phase transformations is further illustrated by the seismic expression of phase transitions, to which we will refer as metamorphic effects. Recent advances in mineral physics show that, locally, phase transformations can contribute more to the seismic velocity anomalies than temperature variations, for instance near 660 *km* depth (Stixrude and Lithgow-Bertelloni (2007)). The metamorphic effects have often been disregarded in forward modelling studies on thermo-chemical mantle convection (e.g. Goes et al. (2000); Deschamps et al. (2007); Tan and Gurnis (2007)).

In this study, we investigate thermo-chemical mantle convection by calculating synthetic seismic velocity anomalies for a wide range of thermo-chemical and iso-chemical mantle convection models. We analyse synthetic shear wave and bulk sound velocities, which are sensitive to compositional heterogeneity and compare the synthetic results to global seismic tomography data. To obtain seismic sensitivities to temperature, composition, and mineral phase tranformations we apply equation of state modelling to a petrologic model. The most voluminous mineral phases of the mantle transition zone are represented in this model, i.e. ringwoodite and garnet coexisting in the upper mantle, and perovskite and magnesiowüstite coexisting the lower mantle. To investigate the seismic signature of the shallow lower mantle we analyse dynamic and metamorphic effects associated with the 660 *km* phase transitions in more detail than before (e.g. Goes et al. (2004)).

The most likely contributors to variations in bulk composition, iron and perovskite, are analysed separately to investigate their seismic expression systematically in Section 5.3.2. Trade-off effects on the synthetic seismic signature are investigated for thermo-chemical reservoir parameters that are related to thermal evolution of the core and convective layering at the transition zone (Section 5.3.3). In Section 5.3.4 we investigate the combined influence of iron and perovskite enrichment to put the modelling results in context with possible formation scenarios of a compositionally distinct reservoir. In particular, we focus on sinking of basaltic crust and fractional differentiation of a magma ocean. From our modelling results we conclude that thermo-chemical models are in better agreement with the seismological data than iso-chemical models.

5.2 Method

5.2.1 A posteriori calculation of seismic velocity anomalies

We calculate shear wave and bulk sound velocity anomalies from numerical models of thermo-chemical convection. Key parameters are listed in Table 5.1. The seismic velocity anomalies are relative deviations from the lateral average, i.e. $\delta \ln v = \delta v / \langle v \rangle$, where $\delta v = v - \langle v \rangle$ represents the absolute deviations from the lateral average of the 180^o 2-D cylindrical model, represented as $\langle v \rangle = \frac{1}{\pi} \int_0^\pi v d\phi$. The forward modelling we apply allows for the separate analysis of seismic anomalies that result from different fields associated with thermo-chemical convection, which comprise anomalies in temperature, δT, composition, δC, and mineral phase, $\delta \Gamma_{ph}$. Composition variations are associated with variations in the relative volume proportion of iron, δX_{Fe}, which interchanges with magnesium, and variations in (Mg,Fe)SiO_3-perovskite, δX_{pv}, which interchanges with (Mg,Fe)O-wüstite (see Section 5.2.2). Phase variations relate to solid-state phase transformations near 660 *km* depth. Mathematically, the a posteriori calculation is expressed as

$$\delta \ln v = \sum_{k=1}^{n_{ph}} \Gamma_{ph,k} \left[\left(\frac{\partial \ln v}{\partial T} \right)_k \delta T + \left(\frac{\partial \ln v}{\partial X_{Fe}} \right)_k \delta X_{Fe} + \right. \tag{5.1}$$

$$\left. + \left(\frac{\partial \ln v}{\partial X_{pv}} \right)_k \delta X_{pv} \right] + \sum_{k=1}^{n_{ph}-1} \left(\frac{\partial \ln v}{\partial \Gamma_{ph}} \right)_{k \to k+1} \delta \Gamma_k .$$

In the above expression the $\frac{\partial \ln v}{\partial Z}$ represent sensitivities of seismic velocity to various model parameters $Z = T, X_{Fe}, X_{pv}$, or Γ_k. Different mineral phases are indicated by the phase index k. The first three terms on the right-hand side describe isomorphic contributions, i.e. seismic velocity anomalies resulting from temperature, iron, and perovskite variations. The last right-hand side term describes the metamorphic contribution, i.e. seismic velocity variations associated with variations from one mineral phase (k) to the next ($k+1$).

Symbol	Parameter	Dimension
v	Seismic velocity	ms^{-1}
C	Composition parameter	–
X_{Fe}	Relative volume proportion of iron	–
X_{pv}	Relative volume proportion of perovskite	–
Γ_{ph}	Phase parameter	–
γ	Clapeyron slope	$MPaK^{-1}$
$R_{\phi/S} = \frac{\delta \ln v_\phi}{\delta \ln v_S}$	Seismic ratio bulk sound to shear wave velocity	–
$\phi_{S\phi}$	Correlation function between $\delta \ln v_S$ and $\delta \ln v_\phi$	–
K_{Fe}^{UM}	Iron distribution coefficient upper mantle	–
K_{Fe}^{LM}	Iron distribution coefficient lower mantle	–
V_{res}	Mantle fraction of compositionally distinct reservoir volume	–
T_c	Initial core temperature	K
T_c^{ad}	Initial adiabatic temperature extrapolated to CMB depth	K
$\Delta T_{CMB} = T_c - T_c^{ad}$	Initial temperature contrast across the CMB	K

Table 5.1: Symbol definitions and parameter values.

5.2.2 Petrological model

We apply seismic sensitivities to temperature and composition for a $FeO-MgO-SiO_2$ mantle. We omit minor constituents such as calcium and aluminum and several minor phases near 660 km depth, such as calcium-pv and akimotoite. Some effect on both the isomorphic and metamorphic seismic sensitivities can be expected from these additional phases (Mattern et al. (2005); Jacobs and de Jong (2007); Stixrude and Lithgow-Bertelloni (2007)). The three chemical components represent the bulk of the mantle (Weidner and Wang (1998)). Within the three-component system, the thermo-dynamically equilibrated coexisting phases of the lower mantle are perovskite and magnesiowüstite (see Table 5.2). Locally, the composition of the lower mantle can change due to variations in iron or silica. A variation in the volume proportion of perovskite (δX_{pv}) that coexists with magnesiowüstite corresponds with a variation in the silica content. The iron content (δX_{Fe}) can change as a result of iron-magnesium interchange within each mineral phase. To obtain seismic sensitivities to temperature, iron, and perovskite in the lower mantle we use depth-dependent parameters for a $FeO-MgO-SiO_2$ mantle, calculated in Trampert et al. (2004).

To calculate the seismic sensitivities to phase transitions near 660 km depth, we apply equation of state modelling of a $FeO-MgO-SiO_2$ petrological model in which the lower mantle is coupled to the upper mantle. The equation of state modelling is described in detail in Appendix A. For the upper mantle, we assume the coexisting mineral phases ringwoodite and garnet to be partitioned at 55-45 vol% (see Table 5.2

Symbol	Mineral phase	Formula	Volume fraction [-]
ri	ringwoodite	Mg_2SiO_4	0.55
gt	garnet	$MgSiO_3$	0.45
pv	perovskite	$MgSiO_3$	0.71
mw	magnesio-wüstite	MgO	0.29

Table 5.2: Mineral phases used in equation of state modelling.

for specifications). Both the olivine and garnet components transform to the denser perovskite and magnesiowüstite phases near 660 *km* depth in our model. The lower mantle consists of a mineralogical mix of 71-29% perovkite-magnesiowüstite. For the upper-lower mantle transition we calculate the seismic sensitivity to the combined effect for both phase transitions. We do not account for the possibility that garnet transforms to perovskite at a higher pressure than the pressure at which ringwoodite transforms to perovskite and magnesiowüstite. The difference in transformation depth depends on mantle temperature and composition and whether it is significant for the mantle is a current issue of debate (Hirose et al. (1999); Wang et al. (2006)).

From the equation of state modelling we also calculate seismic sensitivities to temperature and iron for the lowermost part of the upper mantle. Although the focus of our analysis is on the lower mantle, synthetic seismic velocity anomalies for the upper mantle serve as a background for the effects of phase transformations near 660 *km* depth. By assuming that olivine is in the ringwoodite phase and the transformation from pyroxene to the garnet-majorite phase is complete, the applicability of the sensitivities is limited to depths greater than 520 *km*. The seismic expression of ringwoodite-garnet variations is not taken into account.

We assume a bulk iron fraction of 10%, based on mineral physics estimates for the lower mantle (e.g. Green and Falloon (1998)). Applied values for iron partitioning coefficients are in line with recent mineral physics estimates, i.e. $K_{Fe}^{UM} = \frac{X_{Fe}^{ri}/X_{Mg}^{ri}}{X_{Fe}^{gt}/X_{Mg}^{gt}} = 0.75$ for the upper mantle (Frost (2003)) and $K_{Fe}^{LM} = \frac{X_{Fe}^{pv}/X_{Mg}^{pv}}{X_{Fe}^{mw}/X_{Mg}^{mw}} = 0.25$ for the lower mantle (Auzende et al. (2008)). We verified that our choice for K_{Fe}^{UM} and K_{Fe}^{LM} has a minor influence on the model results and does not affect the conclusions of this study.

5.2.3 Model test cases with iron and perovskite variations

We use several test cases where the composition parameter applied in the thermochemical model, δC (see Method Chapter 2), is associated with various combinations of iron and perovskite anomalies, δX_{Fe} and δX_{pv}. We apply the following expression

to relate δC to δX_{Fe} and δX_{pv}:

$$\frac{\delta\rho_C}{\rho_0}\delta C = \frac{\partial \ln\rho}{\partial X_{Fe}}\delta X_{Fe} + \frac{\partial \ln\rho}{\partial X_{mw}}\delta X_{mw}. \tag{5.2}$$

The proportionality constant, $\delta\rho_C/\rho_0$, relates density and composition parameter, C, in the convection model. The term $(\delta\rho_C/\rho_0)\delta C$ is the effective compositional excess density. The partial derivatives $\frac{\partial \ln\rho}{\partial X_{Fe}}$ and $\frac{\partial \ln\rho}{\partial X_{pv}}$ express the density sensitivity to iron and perovskite, respectively. To maintain a constant petrological anomaly when a parcel changes depth we must apply a constant sensitivity of density to petrologic anomaly ($\frac{\partial \ln\rho}{\partial X}$) because the density derivative with respect to the composition parameter ($\frac{\partial \ln\rho}{\partial C} = \frac{\delta\rho_C}{\rho_0}$) is constant with depth in our model.

Iron and perovskite anomalies have a different seismic expression and the influence of single components is investigated in Section 5.3.2 and 5.3.3. For this purpose, two model cases are applied. For case FE (see Table 5.3) compositional variations are associated with iron variations. We apply a density sensitivity to iron of $\frac{\partial \ln\rho}{\partial X_{Fe}} = 0.37$, which is representative for the entire lower mantle depth (Trampert et al. (2004)). For the FE case, perovskite is absent from the model ($\delta X_{pv} = 0$) and has no effect on the density ($\frac{\partial \ln\rho}{\partial X_{pv}} = 0$). For case PV, compositional variations are associated with perovskite variatons. Iron anomalies are absent for this case ($\frac{\partial \ln\rho}{\partial X_{Fe}} = 0$ and $\delta X_{Fe} = 0$). For the lower mantle, values of $|\frac{\partial \ln\rho}{\partial X_{pv}}| < 0.02$ are inferred, changing from positive in the shallow lower mantle to negative in the deep lower mantle (Wang et al. (1994); Trampert et al. (2004)). The small value of $|\frac{\partial \ln\rho}{\partial X_{pv}}|$ results in large variations of perovskite for a given compositional density anomaly in the convection models. To avoid petrologically unrealistical perovskite anomalies, we apply a value $\frac{\partial \ln\rho}{\partial X_{pv}} = 0.05$ for the density sensitivity to perovskite.

We put our models in perspective with possible formation processes of a compositionally distinct reservoir in Section 5.3.4. To this end, we apply two additional model cases in which the seismic velocity anomalies depend on a combination of iron and perovskite anomalies. Because perovskite has a negligible influence on density in the lower mantle we assume ($\frac{\partial \ln\rho}{\partial X_{pv}} = 0$) for these cases and compositional density anomalies are entirely associated with iron enrichment ($\frac{\partial \ln\rho}{\partial X_{Fe}} = 0.37$). For case C1 the amount of perovskite is similar as in the PV cases, and for case C2 the amount of perovskite is doubled (see Table 5.3). The iron and perovskite content for each case are listed in Table 5.3 and affect the seismic velocity according to equation (5.1).

Model	$\frac{\delta\rho_C}{\rho_0}$ [%]	γ $[MPaK^{-1}]$	V_{res} [%]	T_c [K]	ΔT_{CMB} [K]	Case	$\frac{\partial \ln\rho}{\partial X_{Fe}}$ [−]	δX_{Fe} [−]	$\frac{\partial \ln\rho}{\partial X_{pv}}$ [−]	δX_{pv} [−]
R00	0.	-2.5	20	4273	1723	FE	0.37	0	0	0
						PV	0	0	0.05	0
R10	1.	-2.5	20	4273	1723	FE	0.37	1.35	0	0
						PV	0	0	0.05	10
R15	1.5	-2.5	20	4273	1723	FE	0.37	2.00	0	0
						PV	0	0	0.05	15
G125	1.	-1.25	20	4273	1723	FE	0.37	1.35	0	0
						PV	0	0	0.05	10
T40V10	1.	-2.5	10	4273	1723	FE	0.37	1.35	0	0
						PV	0	0	0.05	10
T37V10	0.9	-2.5	10	3973	1423	FE	0.37	1.21	0	0
						PV	0	0	0.05	9
T32V10	0.8	-2.5	10	3473	923	FE	0.37	1.08	0	0
						PV	0	0	0.05	8
						C1	0.37	1.08	0.	8
						C2	0.37	1.08	0.	16
T24V10	0.8	-2.5	10	2673	123	FE	0.37	1.08	0	0
						PV	0	0	0.05	8
T24	0.8	-2.5	20	2673	123	FE	0.37	1.08	0	0
						PV	0	0	0.05	8

Table 5.3: Parameters values for the different models, with compositional excess density $\frac{\delta\rho_C}{\rho_0}$, Clapeyron slope γ, reservoir volume percentage with respect to the mantle volume V_{res}, initial core temperature T_c, and initial temperature contrast across the CMB that is defined as the difference between the cut-off temperature of the adiabatic geotherm at the CMB and core temperature: $\Delta T_{CMB} = T_c - T_c^{ad}$. The different cases refer to models in which only iron is present (FE), only perovskite is present (PV), or a combination of both iron and perovskite (C1 and C2). The cases are described in detail in Section 5.2. They differ in the density sensitivity to iron ($\frac{\partial \ln\rho}{X_{Fe}}$) and perovskite ($\frac{\partial \ln\rho}{X_{pv}}$). The petrological anomaly associated with an anomaly in the compositional parameter $\delta C = 0.5$ is indicated for iron (δX_{Fe}) and perovskite (δX_{pv}).

5.3 Results

5.3.1 Seismic sensitivities

Figure 5.1 shows the seismic sensitivities to temperature, iron, and perovskite variations used throughout this chapter to calculate shear wave and bulk sound velocity anomalies. Lower mantle sensitivities are from Trampert et al. (2004) (shown below $z = 660$ *km*) and upper mantle sensitivities (above 660 *km*) result from equation of state modelling applied to a ri-gt/pv-mw petrological model, described in Section 5.2.2 and Appendix A. Upper and lower mantle seismic sensitivities are of the same sign and similar amplitude. The seismic velocity increase across the ri-gt=pv-mw phase transformations is 16.6% for shear wave and 2.8% for bulk sound velocity (not shown in Figure 5.1).

To put our modelling results in perspective with the seismological observations, we compare the density and elastic moduli that are calculated from the equation of state modelling (describeb in Section 5.2 and Appendix A) to the 1-D reference model PREM (Dziewonski and Anderson (1981)). Our predictions for density, bulk modulus, and shear modulus deviate from the PREM values calculated at the 670 *km* discontinuity by respectively -1%, -4%, and -7% in the upper mantle and +1%, -6%, and +12% in the lower mantle. It is possible that our predicted increase of shear wave velocity at the upper-mantle boundary is somewhat larger than in PREM, which predicts a 6.5% increase at 670 *km* and a 12.3% increase between 600-770 *km*. For bulk sound velocity, a 2.8% increase at the upper-lower mantle boundary is in reasonable agreement with seismological and petrological observations (Wang et al. (2008)).

We verified that the above results are not significantly affected by model input parameters, such as perovskite content and the high temperature-pressure conditions to which we extrapolate the physical quantities (see Appendix A for details). The comparatively large misfit to PREM for the shear modulus (and hence shear wave velocity) is persistent in our model. To decrease the deviations in shear modulus from PREM from -7% and +12% to -4% and +6% for the upper and lower mantle respectively, the bulk iron fraction has to increase from 10% to 20%, but this degrades the match to density (+2% and -5% deviations from PREM instead of +1% and -1%). Future improvements in the determination of the physical rock properties or adding more complexity to the petrological model could also affect the match with PREM. From the above results, we conclude that the applied petrological model is useful for investigating the seismic expression of the phase transformations around 660 *km* depth.

5.3.2 Seismic expression of compositionally heterogeneous material

The seismic sensitivities of Section 5.3.1 are used to calculate the seismic signature of dynamically consistent thermo-chemical and iso-chemical convection models. Figure

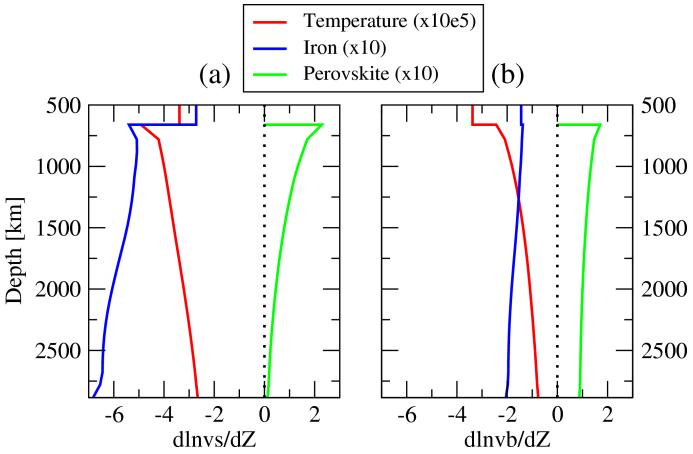

Figure 5.1: Seismic sensitivities used to calculate seismic velocity anomalies for (a) shear wave velocity and (b) bulk sound velocity. The lower mantle values (shown below 660 *km*) are from Trampert et al. (2004). Upper mantle values (shown below 660 *km*) are calculated using equation of state modelling described in Section 5.6. Values for sesimic sensitivities to phase transformations are mentioned in the text (Section 5.3.1). The black dotted line indicates zero value for reference.

5.1 shows that the seismic sensitivities to iron and temperature are of the same sign and sensitivities to perovskite and temperature are of opposite sign. To investigate the consequences for models of thermo-chemical mantle convection, we analyse the seismic expression of iron and perovskite variations separately in this section. We apply case FE for models with anomalies associated with iron anomalies purely, and case PV for models with only perovskite (see Section 5.2.3 and Table 5.3 for a description of the model cases). The same cases are used in Section 5.3.3 where the influence of different convection parameters on the synthetic results is investigated. With model cases C1 and C2 we examine the combined influence of iron and perovskite in Section 5.3.4 to put the modelling results in context with formation processes of a compositionally distinct mantle reservoir.

Figure 5.2 shows results for models R00, R10, and R15 (explained in more detail in Chapter 4) with a progressively larger compositional excess density: $\delta\rho_C/\rho_0 = 0$, 1, and 1.5%. The top three rows show lateral variations of composition, temperature, and phase function. For the neutrally buoyant model (R00, left-hand column) the compositionally distinct reservoir mixes passively with the overlying mantle and becomes dispersed throughout the mantle domain, as shown by the lateral anomalies in the composition field (top row). For the other two models the reservoir is configured as thermo-chemical piles (model R10, middle column) or as a globally continuous layer (model R15, right-hand column). Temperature anomalies are sub-

stantially larger for thermo-chemical models than for iso-chemical models (2nd row), because a higher thermal buoyancy is required to destabilise intrinsically dense material (e.g. Lin and van Keken (2006)). For all models shown, lateral variations in the phase parameter (3rd row) reflect thermally-induced topography of the endothermic phase transition, with uplift over hot upwellings.

Seismic velocity anomalies calculated for the above models are shown in row 4-7. Note that the predicted seismic anomalies have no physical meaning above the wadsleyite-ringwoodite transformation around 520 *km* depth (see Section 5.2.2), although these results are shown for reference. In general, the occurence of negative seismic velocity anomalies at positive temperature anomalies is dictated by the negative seismic sensitivities to temperature (see Figure 5.1). Near 660 *km* depth, shear velocity anomalies change sign (row 4 and 6) and bulk sound velocities are reduced to nearly zero (row 5 and 7), due to the endothermic phase transition. Note that the amplitude ratio of the thermal and metamorphic contribution to seismic anomalies is insenstive to model dynamics, because both contributions are influenced by temperature in a similar way.

The influence of variations in iron and perovskite content on the seismic signature are compared using the two model cases in which compositional anomalies are associated with variations in a single petrological anomaly. Figure 5.2 shows $\delta \ln v_S$ and $\delta \ln v_\phi$ anomalies for the case with variations in iron fraction (case FE) in row 4 and 5 and the case with perovskite variations in row 6 and 7. For the neutrally buoyant model, R00, seismic velocity anomalies depend on temperature and phase, but not on composition. Consequently, the results for the FE and PV cases are identical (Figures 5.2a4,5 and a6,7). For the thermo-chemical models, R10 and R15, positive temperature anomalies generally coincide with positive compositional anomalies (Figures 5.2b1,2 and c1,2). In the presence of iron-rich material, negative seismic velocity anomalies in hot compositionally dense material are amplified (Figures 5.2b4,5 and c4,5) and v_S and v_ϕ anomalies are of the same sign. For these cases compositional anomalies of $\delta C = 0.5$ are associated with iron anomalies of $\delta X_{Fe} = 1.35\%$ for model R10 and $\delta X_{Fe} = 2.\%$ for model R15 (see Table 5.3). The seismic expression of perovskite is very different from iron, as shown by the PV cases depicted in Figures 5.2b6,7 and c6,7 for model R10 ($\delta X_{pv} = 10\%$ at $\delta C = 0.5$) and model R15 ($\delta X_{pv} = 15\%$). Seismic anomalies associated with perovskite-rich material counteract seismic anomalies of thermal origin. As a consequence, shear wave and bulk sound velocity anomalies are of opposite sign in regions with large-scale compositional heterogeneity.

The relation between lateral variations in v_S and v_ϕ is a powerful diagnostic for compositional heterogeneities. To focus on this relation in more detail, we quantify the influence of reservoir petrology on the seismic signature by showing depth profiles of the v_S-v_ϕ correlation, denoted $\phi_{S\phi}$ (Figure 5.3), and histograms of the seismic ratio $R_{\phi/S} = \delta \ln v_\phi / \delta \ln v_S$ (Figure 5.4). Strongly decreased or negative correlations

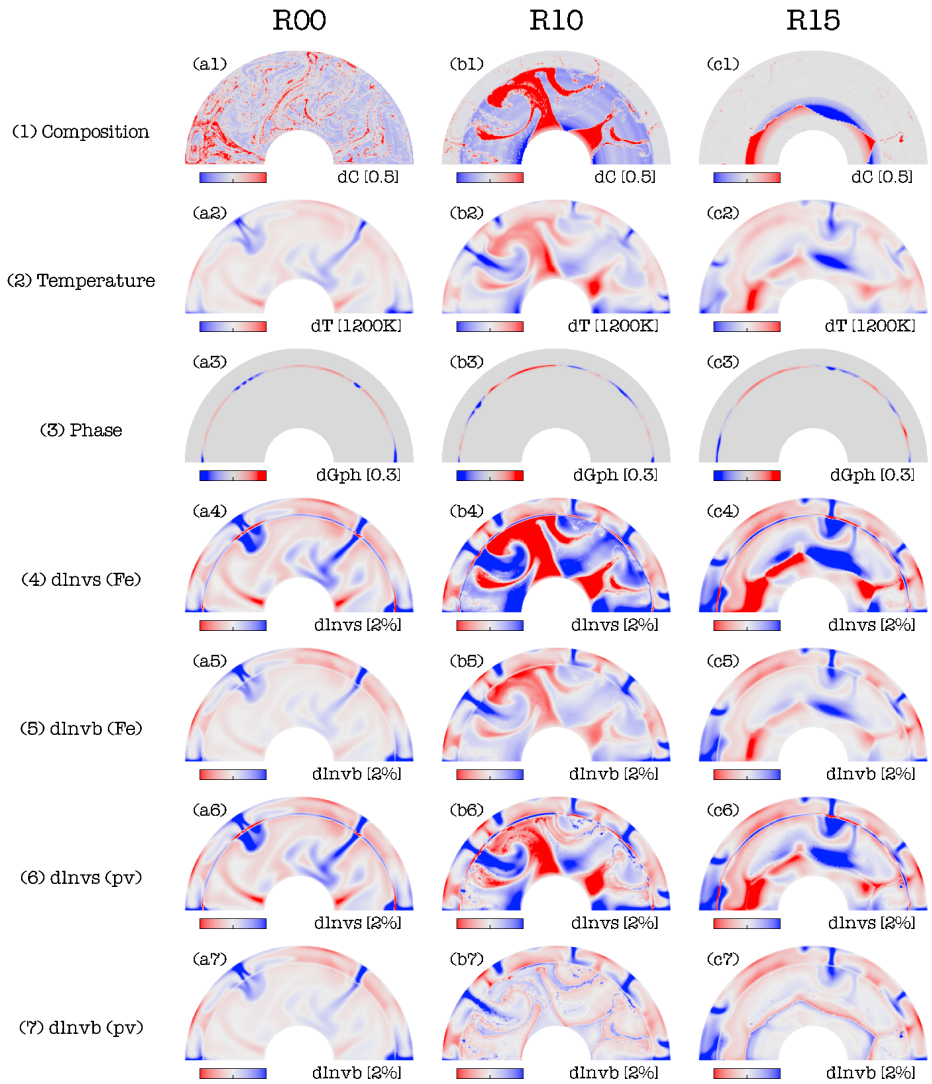

Figure 5.2: Synthetic seismic velocity anomalies calculated for models with different compositional excess density $\frac{\delta\rho_C}{\rho_0}$. (left) neutrally buoyant model R00 ($\frac{\delta\rho_C}{\rho_0} = 0$), (middle) model R10 ($\frac{\delta\rho_C}{\rho_0} = 1$), and (right) model R15 ($\frac{\delta\rho_C}{\rho_0} = 1.5$). Different rows show lateral variations in (1) composition parameter, (2) temperature, (3) phase function. (4) $\delta \ln v_S$ and (5) $\delta \ln v_\phi$ for a model with iron variations. (6) $\delta \ln v_S$ and (7) $\delta \ln v_\phi$ for a model with perovskite variations. Because of neutral compositional buoyancy, the seismic velocity anomalies for model R00 are dependent on temperature and phase but independent of composition. As a consequence, frames a4-a6 and a5-a7 are identical. All results shown are for a model time of 3.6 *Gyr*.

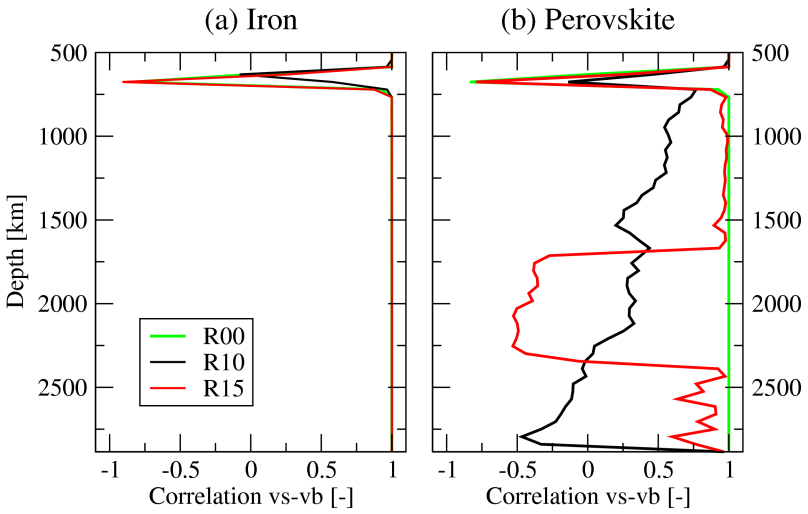

Figure 5.3: Depth profiles of correlation function between shear wave and bulk sound velocity anomalies, $\phi_{S\phi}$. Models R00, R10, and R15 (green, black, and red curves) have a subsequently higher compositional excess density of $\frac{\rho_C}{\rho_0} = 0, 1$, and 1.5% (see Table 5.3). The two frames show different model cases in which compositional anomalies are associated with (a) iron variations (case FE) and (b) perovskite variations (case PV).

for $\phi_{S\phi}$, together with strong negative values for $R_{\phi/S}$ have been inferred in the lowermost mantle from seismological data (e.g. Su and Dziewonski (1997); Van der Hilst and Kárason (1999); Saltzer et al. (2001); Kennett and Gorbatov (2004)). The modelling results also show a negative correlation between density and shear wave anomalies where compositionally distinct material is present in the deep mantle. This is shown for example for model R10 in Figure 4.1f and 5.2 (frame b4 and b6) and is qualitatively in agreement with normal mode data (Ishii and Tromp (1999, 2004)).

Figure 5.3a shows a high correlation close to $\phi_{S\phi} = 1$ for models with an iron-enriched reservoir in the entire lower mantle, except near 660 *km* depth where phase transitions play a role. Iron enrichment has little influence on $\phi_{S\phi}$ because shear wave and bulk sound velocity sensitivities to iron and temperature show a similar behaviour (Trampert et al. (2001)), as shown in Figure 5.1a. Consequently, the correlation function cannot discriminate between iron and temperature anomalies. Figure 5.3b shows that the correlation is sensitive to perovskite and decreases down to $\phi_{S\phi} = 0.5$ in regions with pronounced compositional lateral heterogeneity (cf. to Figure 5.2). For model R10 (black curve) the correlation decreases gradually with depth, while for model R15 a strong decrease in correlation is restricted to 1700-2400 *km* depth (red curve). For model R15, the high correlation ($\phi_{S\phi} \sim 1$) observed below 2400 *km* reflects a nearly iso-chemical mantle below the undulating compositional interface.

Histograms of the seismic ratio $R_{\phi/S}$ (Figure 5.4) are calculated by point-by-point comparison of non-zero velocity anomalies within three lower mantle depth intervals as indicated in the figure caption. A bin size of 0.1 is applied. Models with iron variations (frame a) and purely thermal models (green curves) are characterised by narrow histograms. Significant negative values are only observed for models where compositional heterogeneity is associated with perovskite enrichment and configured as isolated piles or dispersed blobs in the lower mantle. This is shown in Figure 5.1 for model R10 (frame b1-b3, black curves) where $R_{\phi/S}$ values are dispersed towards lower values throughout the lower mantle. The seismic ratio $R_{\phi/S}$ can discriminate between anomalies in perovskite and temperature, but not between iron and temperature, similar to the correlation function $\phi_{S\phi}$. This behaviour is similar to the reported behaviour of the seismic ratio between P and S-velocity anomalies (Deschamps and Trampert (2003)).

Figure 5.2 showed that seismic velocity anomalies are substantially larger for thermo-chemical models than for iso-chemical models (row 4-7), because of larger thermal anomalies required to destabilise intrinsically dense material (row 2). The differences in amplitude between contrasting models are quantified by depth profiles of (laterally averaged) RMS seismic velocity anomalies in Figure 5.5. Recent models of global seismic tomography are shown for reference by the black curves in this figure (see caption for details). For the iso-chemical model R00 (green curves) v_S and v_ϕ anomalies are closest to the observational data. For the layered model a strong mid-lower mantle peak in RMS amplitude is associated with the temperature contrast at the undulating compositional interface (R15, red curves). Such a strong local maximum of seismic velocities in the mid-mantle is not in agreement with the tomographic data (black curves). For the thermo-chemical piles model (R10, black curves) the trend in the depth-distribution of RMS seismic velocity anomalies is in general agreement with the observational data: low amplitudes in the mid-lower mantle and higher amplitudes in the shallow and deep lower mantle. RMS shear wave velocity anomalies are increased throughout the lower mantle up to a factor 3 for perovskite-enriched cases and a factor 4 for iron-enriched case, with respect to the seismic data. The RMS amplitudes of the piles model are significantly higher than the observed amplitudes in global seismic tomography. The discrepancy can (partly) result from poor tomographic resolution in vast parts of the mantle (e.g. Antolik et al. (2003); Romanowicz (2003)) which can result in an underestimation of the RMS amplitudes in tomographic models by as much as 50% or (locally) more. In the following section we will investigate how the amplitudes of seismic velocity anomalies depend on several parameters of the thermo-chemical convection model.

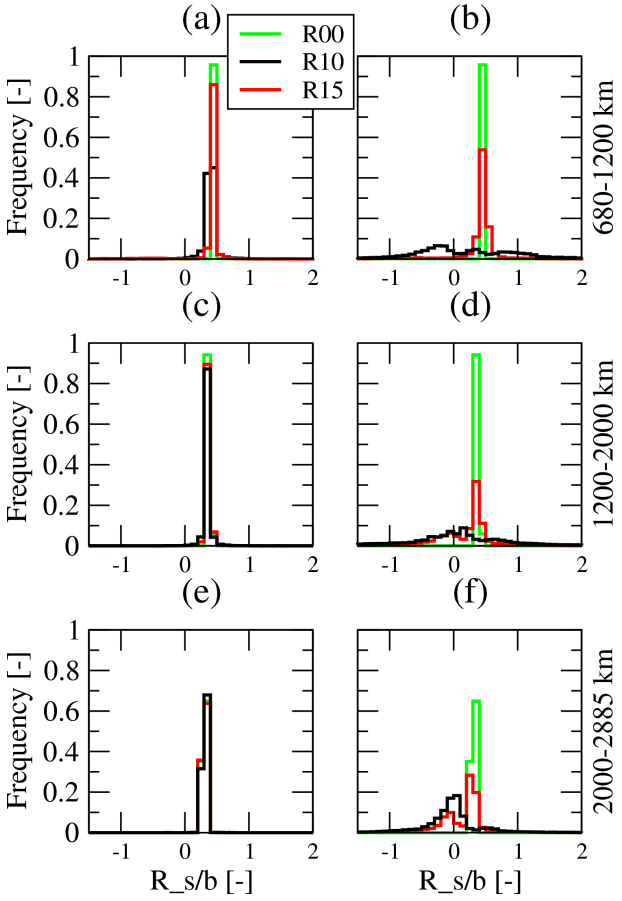

Figure 5.4: Histograms of seismic ratio $R_{\phi/S}$ for the depth ranges (top) 680-1200km, (middle) 1200-2000 km, and (bottom) 2000-2885km. The histogram bin size is 0.1. The ratio of shear wave to bulk sound velocity anomalies is shown for models with (a) iron and (b) perovskite variations. Different models are R00 (green curves), R10 (black curves), and R15 (red curves) (see Table 5.3 for specifications).

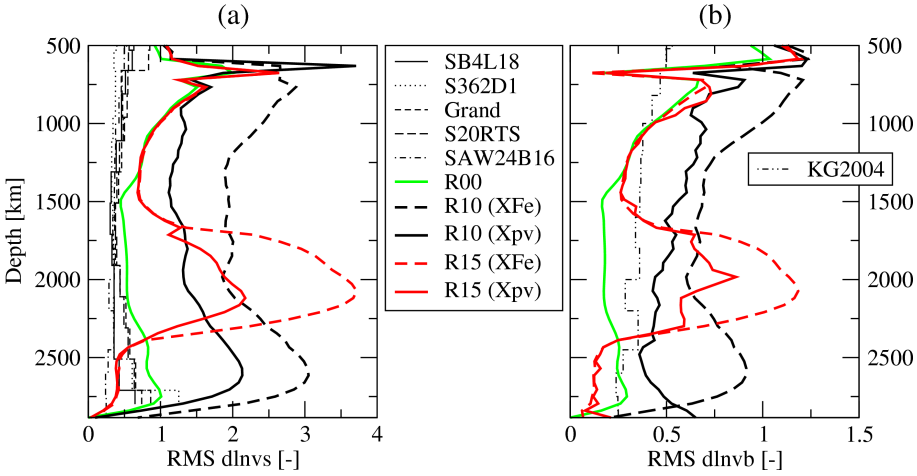

Figure 5.5: Depth profiles of RMS values of the seismic velocity amplitudes, calculated for (a) $\delta \ln v_S$, and (b) $\delta \ln v_\phi$. Thin black curves are data for different global tomography models. Shear wave velocity models are S362D1 (Gu and Dziewonski (1999)), SB4L18 (Masters et al. (2000)), SAW24B16 (Mégnin and Romanowicz (2000)), Grand (Grand et al. (1997)), and S20RTS (Ritsema and Van Heijst (2000)). The shear wave models are available from the UCSD web site `http://mahi.ucsd.edu/Gabi/rem2.dir/shear-models.html#visual`. The bulk sound model indicated as KG2004 is from Kennett and Gorbatov (2004).

5.3.3 Seismic signature dependency on convection parameters

The results of Section 5.3.2 showed that for the model with large-scale thermo-chemical piles enriched solely in perovskite (R10), the synthetic seismic signature is characterised by a negative correlation between v_S-v_ϕ anomalies in the deep mantle –in general agreement with seismological inferences. Such behaviour is not observed for iso-chemical models, nor for thermo-chemical models with a reservoir enriched in iron or configured as a globally continuous layer (R15), which strengthens previous work (e.g. Deschamps et al. (2007)). For the piles model, the depth-dependent character of synthetic seismic velocity anomalies is in general agreement with the observational data. However, the amplitudes of the velocity anomalies are significantly larger than the tomographic data suggest and perhaps difficult to reconcile with the observational data, although the resolution of tomographic data is an issue here. In the experiments described below we investigate if and how amplitudes of synthetic seismic velocity anomalies decrease for different mantle convection parameterisation, using model R10 as a reference.

Clapeyron slope of the endothermic phase transition The degree of convective layering at the transition zone has a strong influence on mantle dynamics and phase boundary topography and both influence the seismic signature (Section 5.3.2, Figure 5.2). This motivates additional experiments with varying Clapeyron slope magnitude. Figure 5.7 shows the results for model G125 (dark green curves), in which the Clapeyron slope magnitude was reduced to $\gamma = -1.25 MPaK^{-1}$ (see Table 5.3) and which is otherwise similar to model R10 (black curves). The Clapeyron slope influences the synthetic seismic signature in three ways (see also Chapter 3).

Firstly, a decreased Clapeyron slope magnitude for model G125 results in reduced phase boundary topography. Consequently, a decrease of metamorphic effects occurs which is reflected by the smaller deviations near 660 *km* depth from the background RMS values in Figure 5.7.

Secondly, a reduced Clapeyron slope produces an increased frequency of downwellings that penetrate the lower mantle, which promotes reservoir destabilisation and compositional homogenisation of the lower mantle (see Chapter 3). In absence of large-scale thermal anomalies, seismic anomalies decrease thoughout the lower mantle. This results in a reduction of RMS velocity anomalies throughout the lower mantle, as shown in Figure 5.7.

Thirdly, a lower Clapeyron slope magnitude results in a lower degree of convective layering at the transition zone, which is associated with a smaller thermo-chemical boundary layer near the top of the lower mantle (see Chapter 3). A high degree of convective layering at the upper-lower mantle transition zone promotes seismic velocity anomalies of compositional origin in the shallow lower mantle. This is expressed by the RMS profiles in Figure 5.7, which shows that seismic velocity anomalies in

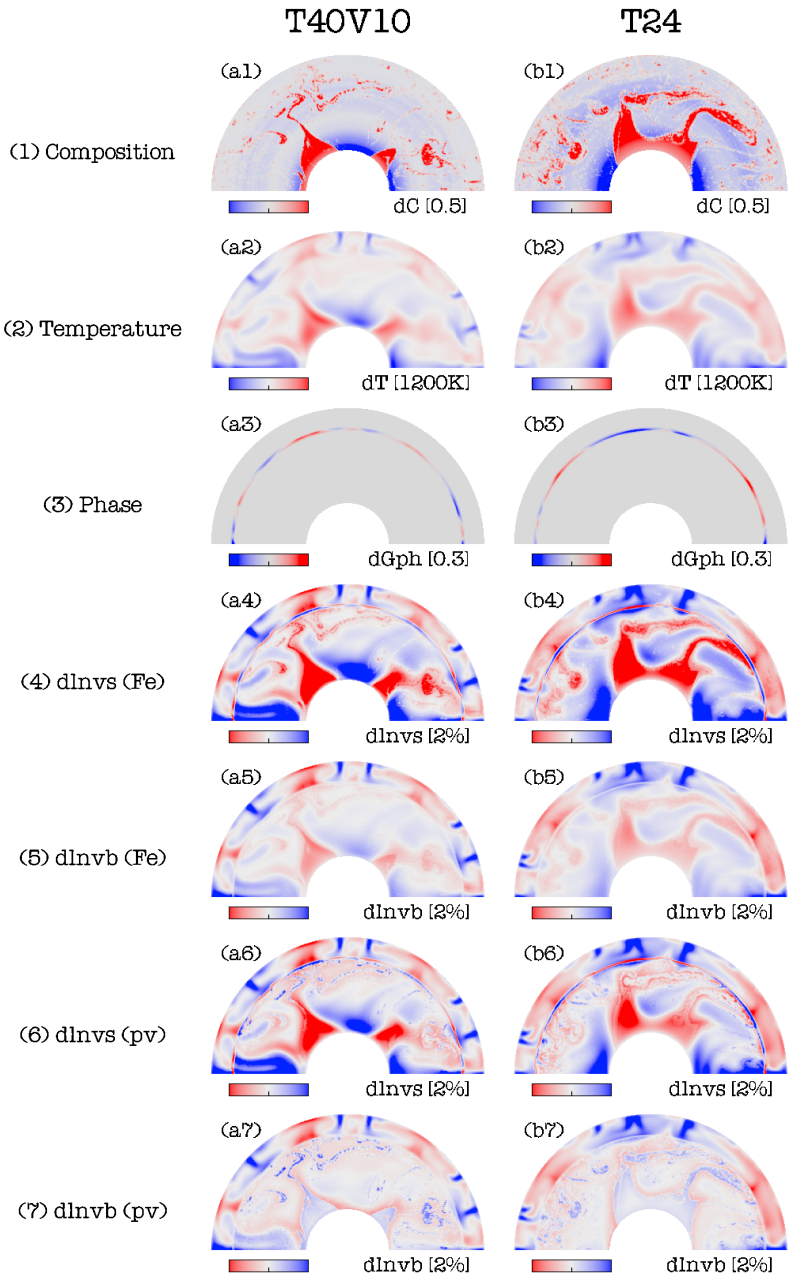

Figure 5.6: Same as in Figure 5.2 for (left) model T40V10 with a compositionally distinct reservoir volume of $V_{res} = 10vol\%$. (right) model T24 with the initial core temperature reduced to $T_c = 2673K$. Both models are otherwise similar to model R10 with $V_{res} = 20vol\%$ and $T_c = 4273K$ (see Figure 5.2 and Table 5.3). All results shown are for a model time of 4.5 Gyr.

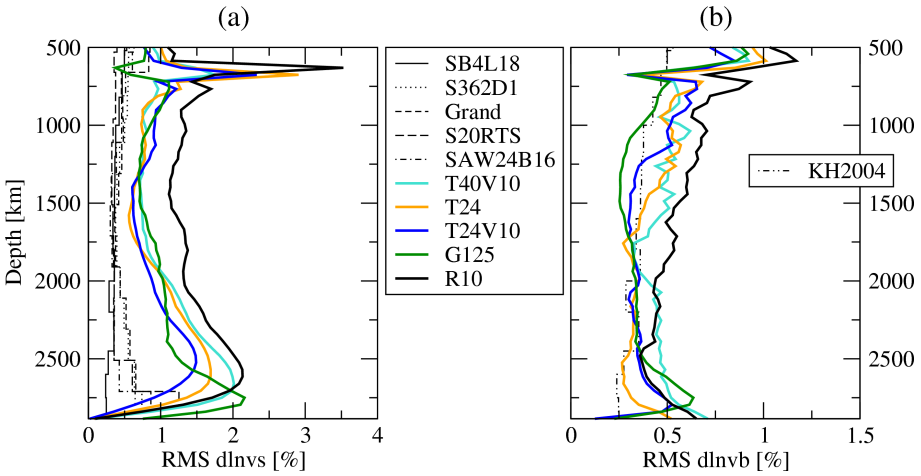

Figure 5.7: Same as in Figure 5.5 for a compilation of models with convection parameters varied from the reference model R10 (thick black curves) as indicated in Table 5.3. Models T40V10 (turqoise), T24R08 (orange), T24V10 (blue), and G125 (dark green) are described in Section 5.3.3.

the shallow lower mantle (680-1200 *km*) are larger for model R10 than for model G125. A compositional heterogeneous shallow lower mantle has been inferred from seismic inversion studies (Trampert et al. (2004)). Convection models that neglect the dynamic influence of convective layering at the transition zone have shown a discrepancy between the synthetic and observational data (Deschamps et al. (2007)).

Volume of the compositionally distinct reservoir Because the amplitude of seismic velocity anomalies increases in the presence of a compositionally distinct reservoir, an obvious parameter to test is the reservoir volume. To quantify the influence of reservoir volume we examine model T40V10, in which a reservoir volume of 10 vol% is applied –half the volume of reference model R10 (see Table 5.3). Figures 5.6 (right-hand column, frame 4-7) and 5.7 show that in absence of compositionaly distinct material, seismic velocity anomalies are reduced in amplitude in large parts of the lower mantle for model T40V10 (turqoise curves) relative to model R10 (black curves). Large-scale compositional heterogeneity is preserved in the deep lower mantle that is associated with a decreased correlation between shear wave and bulk sound velocity anomalies, shown in Figure 5.7a.

Core temperature For thermally convective systems, lateral temperature variations increase for larger temperature contrasts across the top and bottom of the mantle domain (e.g. Hansen et al. (1993)). Therefore, some effect of the uncertain core temper-

ature on the seismic signature can be expected. Below, we explore core temperature values that reflect the current range of uncertainties (Alfè et al. (2007), R. Boehler, personal communication). For all models, the initial adiabatic geotherm has a potential temperature of $T_p = 2073K$. The initial adiabatic geotherm extrapolated to the CMB corresponds with a temperature of $T_c^{ad} = 2550K$, but it is truncated at the CMB to the initial core temperature T_c, which varies between the different models (see Table 5.3 for values). The temperature constrast across the CMB equals $\Delta T_{CMB} = T_c - T_c^{ad}$.

The effect of core temperature on seismic signature is demonstrated for model T24, which has a substantially lower initial core temperature of $T_c = 2673K$ than the reference model R10 ($T_c = 4273K$) (see Table 5.3). Model T24 was selected for having similar reservoir stability conditions as model R10, which was achieved by decreasing the compositional excess density from 1 to 0.8%. Thermal anomalies are smaller when the temperature contrast across the CMB decreases. This is reflected by the smaller seismic velocity anomalies of thermal origin throughout the lower mantle for model T24 (Figure 5.6a4-7) than for model R10 (Figure 5.2b4-7). The reduction of seismic velocity anomalies is shown by the RMS profiles of Figure 5.7 (T24, orange curves; R10, black curves).

To put our results in context with the evolution of core-mantle heat transport, we investigate the core temperature and CMB heat flux for the models with contrasting core temperature. Included are models with an initial core temperature between $2473K$ and $4373K$ (models T24V10, T32V10, T37V10, and T40V10). The compositional excess density is scaled to maintain comparable reservoir stability conditions between the different models (see Table 5.3). In the experiments, the volume of the compositionally distinct reservoir was reduced to 10 vol%, because previous experiments demonstrated the improved agreement to the observational data. We verified the combined effect of a reduction in reservoir volume and initial core temperature for model T24V10 ($T_c = 2673K$; $V_{res} = 10vol\%$). The RMS profiles of Figure 5.7 shows that seismic velocity anomalies for model T24V10 (blue curves) are reduced even further than in the model with reduced core temperature (T24, orange curves) or reduced reservoir volume (T40V10, turqoise curves).

Time series of the core temperature and CMB heat flux for contrasting models are shown in Figure 5.8. An increase of the volume of the disctinct reservoir results in a small decrease of the core cooling rate and CMB heat flux, as shown for models T24 (orange curve) and T24V10 (blue curves). Increased compositional excess density promotes gravitational stability of the reservoir in the deep mantle. The corresponding increase in thermal blanketing of the core is reflected by a significantly slower core cooling and lower CMB heat flux shown for models R00, R10, and R15 in Figure 5.8 (green, black, red dotted curves, respectively).

The influence of decreasing the initial core temperature from $4273K$, $3973K$, $3473K$ to $2673K$ is shown in Figure 5.8 for models T40V10 (turqoise curves), T37V10 (brown), T32V10 (magenta), and T24V10 (blue), respectively. Figure 5.8a shows that

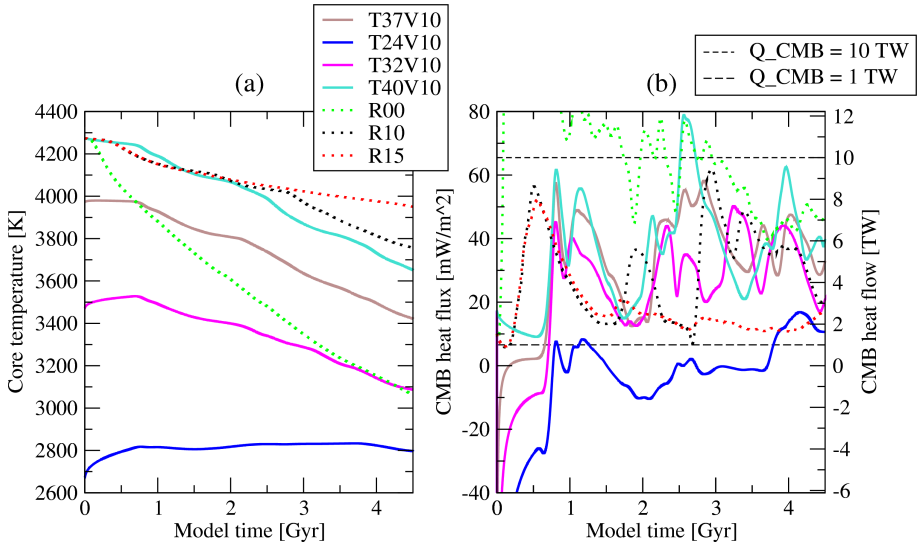

Figure 5.8: Evolution of (a) core temperature and (b) CMB heat flux. The CMB heat flux is positive in the outward core-to-mantle direction. Different models are indicated by the legend. Dashed lines in frame b indicate limit values for the heat flow across the CMB. The values correspond with proposed upper and lower bounds for the total CMB heat flow of 10 and 1 TW, respectively.

the CMB temperature at the end of the model time are around 3650, 3400, 3100, and 2800 K for the models of subsequent lower initial core temperature. The above core temperatures can be compared to estimates of the CMB temperature based on the occurence of a perovskite to post-perovskite (pv-ppv) double crossing that serves as a deep mantle thermometer. When the CMB temperature exceeds the phase boundary temperature at CMB pressure, the geotherm is expected to cross the endothermic phase boundary at two different depths (e.g. Hernlund et al. (2005)) and this can explain seismologically observed complexity in the deep mantle (Van der Hilst et al. (2007)). Recent mineral physics studies predict a minimum required CMB temperature for a pv-ppv double crossing of 3800 K (Hirose (2006)). This value changes by $\sim 500K$ assuming reasonable uncertainties for the reference pressure and Clapeyron slope of the phase boundary of $5GPa$ and $2MPaK^{-1}$, respectively (Murakami et al. (2004); Oganov and Ono (2004); Hirose et al. (2006)). For the convection models with an initial core temperature higher than $T_c = 3473K$ the core temperature after 4.5 Gyr model time is consistent with the constraint for a pv-ppv double crossing.

An upper bound of $\sim 10TW$ for the CMB heat flow has been proposed on the basis of backward extrapolation of the core temperature from heat budget models (see Lay et al. (2008) for an overview). A lower bound around $\sim 1TW$ is estimated for the

core heat loss required to power the geodynamo that has existed for at least 3.5 *Ga* (e.g. Christensen and Tilgner (2004); Biggin et al. (2008)). The CMB heat fluxes that correspond with the heat flow bounds of $\sim 10TW$ and $\sim 1TW$ are indicated by the dashed lines in Figure 5.8b. Figure 5.8b shows that a decrease of the initial core temperature causes a smaller CMB temperature constrast, ΔT_{CMB}, throughout the model evolution and this results in a decrease of the CMB heat flux and core cooling rate. The core has a positive CMB heat flux for the model with the higher initial core temperature (T40V10, turqoise curve) and falls between the proposed upper and lower bounds. For the model with the lowest initial core temperature (T24V10, blue curve) the CMB heat flux is above the proposed lower bound for small time windows around 1 *Gyr* model time and after 3.7 *Gyr*, which is difficult to reconcile with the long-term existence of the geodynamo.

5.3.4 Seismic expression of combined enrichment of iron and perovskite

In the above, iron and perovskite enrichment were analysed separately to examine the seismic expression of the components systematically. To prevent unrealistically large perovskite anomalies in the previous experiments the amount of perovskite for the PV cases was set to the δX_{pv} values listed in Table 5.3. In the experiments below, we take a different approach and put the results in context with candidate formation processes by examining the seismic expression of combined iron and perovskite enrichment in compositionally distinct material. Here the seismic signature depends on variations of both iron and perovskite, whereas compositional density anomalies are associated with iron variations purely. The sensitivity of density to perovskite is neglected, as suggested by mineral physics studies indicating a small density sensitivity to perovskite $\frac{\partial \ln \rho}{\partial X_{pv}}$ compared to the corresponding sensitivity to iron $\frac{\partial \ln \rho}{\partial X_{Fe}}$ (Wang et al. (1994)).

We apply four different cases with different petrological anomalies δX_{Fe} and δX_{pv} to convection model T32V10. Based on previous results, T32V10 is our preferred model in terms of similarity to the seismic observations (see Table 5.3 for model specifications). Petrological anomalies representative for $\delta C = 0.5$ are listed in Table 5.3 and are given between brackets below. We test the following cases: case FE with only iron variations ($\delta X_{Fe} = 1\%$); case PV with only perovskite variations ($\delta X_{pv} = 8\%$); case C1 with a combination of iron and perovskite variations ($\delta X_{Fe} = 1\%$; $\delta X_{pv} = 8\%$); and case C2 which is similar to case C1 but with twice as much perovskite ($\delta X_{Fe} = 1\%$; $\delta X_{pv} = 16\%$). We compare synthetic data to global seismic tomography data (see caption of Figure 5.5 for details).

Figure 5.9 shows the convective regime and synthetic seismic velocity anomalies of model T32V10. The thermal and compositonal anomalies (frame a1 and b1) shows the presence of a 10 vol% thermo-chemical reservoir configured as piles on the CMB, with additional distinct material residing below the endothermic phase transition. The

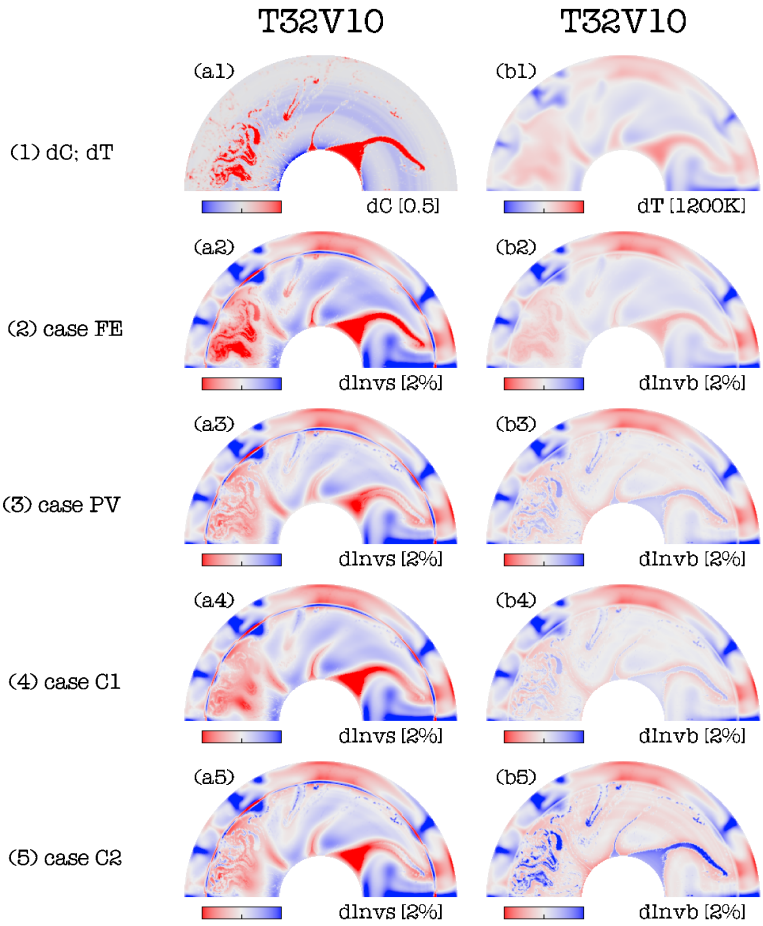

Figure 5.9: Convective state and synthetic seismic velocity anomalies for model T32V10 (see Table 5.3 for specifications). Lateral anomalies are shown for (a1) composition, (b1) temperature. The lower four rows show anomalies in (left) $\delta \ln v_S$ and (right) $\delta \ln v_\phi$ for (2nd row) case FE (3rd row) case PV, (4th row) case C1, and (5th row) case C2. See text for description of the different cases. All results shown are for a model time of 4.5 *Gyr*.

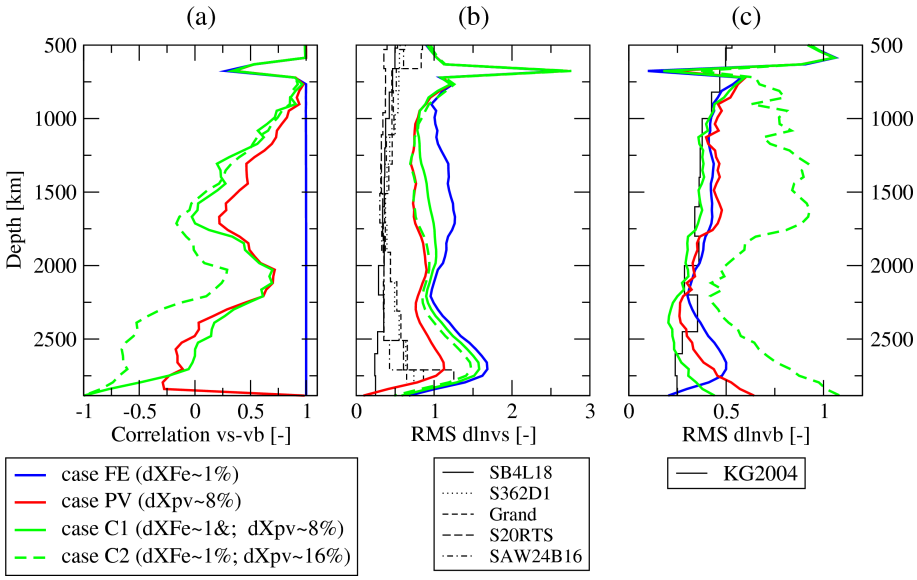

Figure 5.10: Seismic signature for model T32V10 for different combinations of petrological anomalies. Model cases FE, PV, C1, and C2 are indicated by the legend. Between brackets is the petrological anomaly that corresponds with a compositional anomly of $\delta C = 0.5$. (a) Depth profiles of correlation function $\phi_{S\phi}$. RMS profiles are shown in (b) $\delta \ln v_S$ and (c) $\delta \ln v_\phi$. The thin black curves show global tomographic models for comparison (see Figure 5.5 for details).

correlation between v_S and v_ϕ is positive thoughout the lower mantle for the FE case (row 2), and negative for case PV with only perovskite (row 3), in line with the results of Section 5.3.2 and 5.3.3. For the combined iron-perovskite case C1, the effect of 8% perovskite dominates over the effect of 1% iron. As a consequence, the v_S and v_ϕ-anomalies for case C1 (row 4) are closer to the PV case (row 3) than the FE case (row 2). Compared to case C1, the increased amount of perovskite for case C2 (row 5) results in a decrease of shear wave velocity amplitudes in the shallow lower mantle, and an increase of bulk sound velocity amplitudes throughout the lower mantle.

Figure 5.10a shows the v_S-v_ϕ correlation for the different cases. Case C1 and PV (green and red curves) have a comparable v_S-v_ϕ correlation because the perovskite content is identical in these cases and iron has little influence on the correlation. For case C2, large perovskite anomalies dominate the seismic signature in the deep lower mantle and this results in a negative correlation down to $\phi_{S\phi} = -1$ in this region (green dashed curves).

Figure 5.10b shows RMS anomalies for v_S. Because of low v_S sensitivity to perovskite near the CMB (see Figure 5.1), the RMS amplitudes for v_S in the deep mantle are comparable for models with the same amount of iron, i.e. case FE, C1, and C2

(blue, green and green dashed curves). For all cases, the v_S amplitudes are larger than the observational data (black curves), especially when compositionally distinct material is enriched in iron.

The RMS anomalies for v_ϕ are shown in Figure 5.10c. In constrast to v_S, the sensitivity of v_ϕ to perovskite is strong in the deep lower mantle (see Figure 5.1). As a consequence, Figure 5.10c shows that for the case with high perovskite variations (C2, green dashed curve) RMS amplitudes of v_ϕ exceed that of the other cases. The bulk sound velocity amplitudes are higher than the tomographic data suggests (black curve).

5.4 Discussion

In this study, we investigated thermo-chemical mantle convection results by calculating synthetic shear wave and bulk sound velocity anomalies from 2-D numerical models. Applying a combined analysis of shear wave and bulk sound velocities and including the effects of upper-lower mantle phase transformations enables us to investigate thermo-chemical mantle convection in more detail compared to previous studies (e.g. Goes et al. (2000); Nakagawa and Tackley (2006); Deschamps et al. (2007); Tan and Gurnis (2007); Nakagawa and Tackley (2008)). Compared to previous work, our study provides additional constraints with regards to properties of a compositional lower mantle reservoir such as the configuration and volume of the reservoir. Furthermore, we put our results in perspective with possible formation processses of a compositionally distinct reservoir, thermal core evolution, and the seismic expression of the mantle transition zone.

In general, our modelling results show a strongly decreased or negative correlation between v_S-v_ϕ and v_S-ρ in the deep mantle for compositionally distinct material enriched in both perovskite and iron content. Compared to iron, perovskite has a stronger control on seismic velocity anomalies, but iron controls the compositional density anomalies. Within the applied framework such a seismic signature cannot be achieved for iso-chemical models nor for models in which compositional heterogeneity is associated with a single petrological component, i.e. iron or perovskite. The synthetic seismic signature is closest to the available seismological data for models with a deep mantle reservoir characterised by an increase of 1% in iron volume fraction, 8% in perovskite volume fraction, and by 0.8% compositional excess density relative to the overlying mantle. These values are consistent with values suggested by seismic inversion results of Trampert et al. (2004)). The compositional excess density required to ensure gravitional stability and survival of a deep mantle reservoir (e.g. Kellogg et al. (1999)) is compatible with inferences from the Earth's gravity field (Chapter 4) and normal mode data (Ishii and Tromp (2004)). An upper limit for perovskite enrichment is demonstrated by models in which 16% perovskite anomalies cause $\delta \ln v_\phi$ RMS values in the lowermost mantle that exceeds the +1% level, which

is larger than seismological data suggests.

In connection with the thermo-chemical mantle convection models the question arises how large-scale compositionally distinct domains in the deep mantle may have formed. Perhaps the most evident formation process is delamination or subduction of basaltic crust, which is enriched in iron and silica with respect to bulk mantle peridotite and with a density above the lateral average in the deep mantle (e.g. Ono et al. (2005); Perrillat et al. (2006)). Sinking of basaltic crust may have operated throughout Earth's evolution (Christensen and Hofmann (1994)), probably at an increased rate in the Archaean (Tolstikhin and Hofmann (2005); Van Thienen et al. (2005)). Another candidate formation process generating large-scale compositional heterogeneity is differential crystallisation of perovskite-rich material from a magma ocean. Recent mass balance models predict the separation of an assemblage dominated by perovskite to form an isolated reservoir that occupies a mantle volume of 10-15% (Walter et al. (2004)) –similar to that of our preferred model and large enough to influence the seismic signature in the lowermost mantle. Iron enrichment is not predicted in this model but may be explained by subsequent accumulation of subducted basaltic material and/or percolation of iron from the core (Jeanloz and Lay (1993)), perhaps catalysed by the presence of post-perovskite phase of high iron solubility (Mao et al. (2004)).

The analysis of our modelling results shows that the synthetic seismic signature of a reservoir configured as isolated piles on top of the CMB is in good agreement with the seismological observations, provided that the reservoir is enriched in perovskite and reasonable amounts of iron. Less likely is a globally continuous layer in the mid-lower mantle, because no seismological evidence exists for the pronounced v_S and v_ϕ velocity anomalies in the mid-lower mantle that we calculate for such a model. Our combined analysis of shear wave and bulk sound velocity anomalies strengthens conclusions from previous studies (Tackley (2002); Nakagawa and Tackley (2004a); Deschamps et al. (2007); Tan and Gurnis (2007)).

In general, the amplitudes of seismic velocity anomalies in our models are higher than the amplitudes predicted by global seismic tomography data (e.g. Masters et al. (2000); Kennett and Gorbatov (2004)). For thermo-chemical models thermal anomalies required to destabilise intrinsically dense material exceed thermal anomalies for iso-chemical convection models and promote seismic velocity anomalies that are larger than the seismological data suggest. As a result, seismic velocity anomalies increase for increasing reservoir volume and the synthetic seismic signature is closer to the observations for models with a reservoir of 10% mantle volume or less, than for a volume of 20% or more. The above percentages need to be verified using models of 3-D spherical geometry.

The issue of high temperature anomalies associated with heterogeneous material is also related to the value of the temperature contrast across the CMB and the temperature of the core. A high initial core temperature in our models promotes a large

temperature contrast across the CMB for a given mantle temperature. A high core temperature promotes high temperature anomalies in hot upwellings rising from the boundary layer and seismic velocity anomalies increase correspondingly. The agreement with the seismic data is best for models with an initial core temperature of $T_C = 2673K$, is reasonable when using $T_C = 3473K$, and disappears for $T_C = 4273K$. On the other hand, the core temperature in our models are constrained by a positive (core-to-mantle) CMB heat flux of $\sim 1TW$ required by the existence of a geomagnetic field for 3.5 *Ga* or longer (Biggin et al. (2008); Christensen and Tilgner (2004)). Furthermore, heat loss from the core to the mantle is required for reasonable evolution scenarios for inner core growth (Labrosse and Macouin (2003); Nakagawa and Tackley (2004b)). The models with an initial core temperature as low as $T_C = 2673K$ are incapable in generating a positive CMB heat flux throughout most of Earth's history. The predicted present-day core temperature for these models of $\sim 2800K$ is substantially lower than experimentally determined estimates based on iron melting data of around $4000K$ (see Boehler (2000) for a review), although lower estimates may be expected when other elements such as sulfur are accounted for (Boehler, personal communication). Finally, recent seismological imaging of a second crossing of the deep mantle geotherm with the phase boundary between perovskite and its high pressure polymorph post-perovskite suggests a core temperature above $3800K$ (Hirose (2006); Van der Hilst et al. (2007)). Based on the above, we consider models with a present-day core temperature around $3500K$ (model T37V10) as the best compromise to seismic and heat budget constraints.

Large-scale compositional heterogeneity in the shallow lower mantle observed in our models is a natural consequence of chemical filtering in models of partial convective layering at the transition zone in combination with intrinsically dense material of critical gravitational stability (Chapter 3, this thesis). This mechanism can resolve discrepancies between previous synthetic results with a iso-chemical shallow lower mantle (Deschamps et al. (2007)) and seismological data that suggests a compositionally heterogeneous shallow lower mantle (Trampert et al. (2004). Improved seismic resolution in the shallow lower mantle could elucidate how compositional heterogeneity imposed by convective layering at the transition zone relates to the influence of subducting slabs that are compositionally heterogeneous.

Our results show a strong seismic expression near 660 *km* depth of the ri→pv-mw and gt→pv phase transformations, with v_S anomalies that are opposite in sign to the surrounding thermally-induced anomalies and v_ϕ anomalies that are reduced to approximately zero. The metamorphic effects are confined to a narrow layer of $\sim$ 50-70 *km* in the radial direction, but can reduce the velocity amplitudes imaged by seismic tomography images over 100's of *km* because of vertical smearing at transition zone depth (Antolik et al. (2003)). The metamorphic effects are calculated for models with a phase boundary topography of 16 *km* RMS variation –in agreement with recent seismological inferred values (Gu et al. (2003); Deuss et al. (2006)). The localised effect

of phase boundary topography is consistent with several seismic observations in the 500-1000 *km* region, such as a strong local decrease in v_s-v_ϕ and v_s-ρ correlation (Su and Dziewonski (1997); Ishii and Tromp (2004)) and a peak in v_S amplitudes (Masters et al. (2000)).

A direct comparison between tomographic models and seismic velocity predictions from mantle convection models is hampered by uncertainties both in the seismological data and the mineral physics based parameterisation in the convection models. Poor tomographic resolution in vast parts of the mantle affects the amplitudes, correlation functions, and seismic ratios of velocity anomalies to which we compare our data (e.g. Romanowicz (2003); Antolik et al. (2003)). Filtering of the synthetic data to mimic the tomographic resolution could further improve the comparison to the observations in future work (e.g. Deschamps et al. (2007)). Other uncertainties are related to equation of state modelling that is based on several assumptions and emperical laws and rock properties that can be determined with finite precision experimentally and theoretically (Williams and Knittle (2005); Bukowinski and Akber-Knutson (2005); Jacobs and de Jong (2007)). Intrinsic uncertainty in lower mantle petrology is perhaps best illustrated by the discussion about which type of meteorites serve as the petrological building blocks for Earth (e.g. McDonough and Sun (1995)). Whether the less abundant chemical components such as aluminium and calcium have a significant influence on the physical properties of the lower mantle is a current topic of debate (e.g. Mattern et al. (2005)). The seismic signature of the lowermost mantle may be further affected by a high-spin to low-spin transition in iron atoms in perovskite and/or magnesiowüstite (Badro et al. (2004)) and/or the existence of a post-perovskite phase, perhaps enriched in iron due to a high iron solubility (Murakami et al. (2004); Mao et al. (2004); Nakagawa and Tackley (2006)).

5.5 Conclusions

We discussed that the predictive power of numerical mantle convection models will improve when a more direct comparison between synthetic data and observational data becomes possible, which is closely related to future advances in seismic tomography and mineral physics. The main conclusions that we draw from our study are summarised as follows:

- Based on synthetic data for shear wave and bulk sound velocity anomalies, convection models with a compositionally distinct mantle reservoir enriched in both iron and perovskite are more realistic than iso-chemical models, or models with a thermo-chemical reservoir enriched in only perovskite or only iron.

- The seismic signature predicted by convection models is closest to the seismological observations when the deep mantle portion of the compositionally

distinct reservoir is configured as piles on top of the CMB and with a reservoir volume limited to 10 vol%.

- An upper bound of $\sim 3500K$ present-day core temperature is suggested by high amplitudes of seismic velocity associated with hot thermo-chemical material. This constraint becomes more important in view of a suggested lower bound associated with reasonable evolution scenarios of the CMB heat-flux (e.g. Lay et al. (2008)) and inner core growth and the occurence of double crossings of the post-perovskite phase boundary (e.g. Hirose (2006)).

- A reservoir enriched in iron and perovskite that is in agreement with formation processes related to delamination or subduction of basaltic crust (e.g. Christensen and Hofmann (1994); Van Thienen et al. (2005); Tolstikhin et al. (2006)) is associated with a seismic signature that is in general agreement with data fom global seismic tomography. Formation by differential crystallisation of perovskite-rich material in a magma ocean (Walter et al. (2004)) is possible as well, if additional iron originates from the core and/or from deep subduction of basaltic crust.

- Convective layering at the upper-lower mantle transition promotes large-scale compositional heterogeneity in the shallow lower mantle that can resolve discrepancies between previous synthetic data and observational data.

- For reasonable mantle convection parameters, phase transformations near 660 *km* depth are accompanied by a strong seismic expression that can reduce the seismic velocity amplitudes in images of global seismic tomography over 100s of *km* radially.

5.6 APPENDIX A: Calculation of seismic sensitivities using equation of state modelling

The derivation of seismic velocity sensitivities requires calculation of density and elastic moduli at high pressure-temperature conditions. To this end, we apply third-order Birch-Murnagham equation of state modelling. Key parameters are listed in Table 5.4. We broadly follow the approach described in Trampert et al. (2001). The equation of state modelling is applied to rock properties at ambient conditions based on recent mineral physics studies. Values are listed in Table 5.5.

Extrapolation consists of two steps: to high temperature at ambient pressure followed by extrapolation along a mantle adiabat to high pressure. The extrapolation is applied to coexisting mineral phases(e.g. phase 1 and 2 for perovskite and magnesiowüstite). Each phase contains iron and magnesium. Iron is partitioned between the two phases by the iron partition coefficient as follows

$$K_{Fe} = \frac{x^1_{Fe}/x^1_{Mg}}{x^2_{Fe}/x^2_{Mg}}, \tag{5.3}$$

with x^i_{Fe} and $x^i_{Mg} = 1 - x^i_{Fe}$ the volume fractions of iron and magnesium end-members for phase i. The iron fractions for the coexisting phases are related to the global volume fraction of iron as follows

$$X_{Fe} = X_1 x^1_{Fe} + (1 - X_1) x^2_{Fe}, \tag{5.4}$$

with volume fractions X_1 and $X_2 = 1 - X_1$ for phase 1 and 2, respectively.

Symbol	Parameter	Dimension
α_0	Thermal expansivity constant	K^{-1}
α_1	Thermal expansivity constant	K^{-2}
α_2	Thermal expansivity constant	K
G	Shear modulus	GPa
$G' = (\frac{\partial G}{\partial P})_S$	Isentropic pressure derivative shear modulus	GPa
K	Bulk modulus	GPa
$K' = (\frac{\partial K}{\partial P})_S$	Isentropic pressure derivative bulk modulus	GPa
γ_0	Grüneisen parameter	$-$
$q = -d\ln\gamma/d\ln\rho$	Anonymous constant	$-$
$\delta S = -1/(\alpha K)(\partial K/\partial T)_P$	Anderson-Grüneisen parameter	$-$
ε	Eulerian strain	$-$
T_f	Foot of adiabatic temperature profile	K
T_{end}	Final temperature	K
x^i_{Fe}	Relative volume proportion of iron for phase i	$-$
m	Molar fraction	$-$
V	Molar volume	$m^3 mol^{-1}$
M	Molar volume	$kgmol^{-1}$

Table 5.4: Symbol definitions and parameter values for quatities used in equation of state modelling.

The density ρ of a single mineral phase is calculated from the ratio of the weighted sums of molar masses and molar volumes of end-members j:

$$\rho = \frac{\sum_{j=1}^{2} m_j M_j}{\sum_{j=1}^{2} m_j V_j}, \tag{5.5}$$

with V and M the molar volume and molar mass of the two constituents. The molar fraction is defined as $m_j = n_j/n$, with n_j the number of moles of constituent j and n the total number of moles of all constituents. The volume fractions are expressed in the molar fractions of the constituents as follows:

$$x_1 = \frac{m_1 V_1}{m_1 V_1 + (1-m_2)V_2} \tag{5.6}$$

$$x_2 = 1 - x_1 = \frac{(1-m_1)V_2}{m_1 V_1 + (1-m_2)V_2}. \tag{5.7}$$

For extrapolation of density to high temperature conditions we apply a commonly used polynomial expansion for the thermal expansivity (e.g. Fei (1995))

$$\frac{\rho(T_f, P_0)}{\rho(T_0, P_0)} = \exp\left[-\int_{T_0}^{T_f} \alpha_0 + \alpha_1 T - \alpha_2 T^{-2} dT\right]. \tag{5.8}$$

Symbol	ri (mg)	ri (fe)	gt (mg)	gt (fe)	pv (mg)	pv (fe)	mw (mg)	mw (fe)
$V_0[cm^3mol^{-1}]$	39.65 (e)	42.02 (e)	28.54 (e)	29.43 (e)	24.45 (e)	25.59 (e)	11.25 (e)	12.25 (e)
$a_0[K^{-1}](\times 10^{-5})$	2.57 (c)	2.57 (c)	2.880 (a)	2.880 (a)	2.461 (b)	2.461 (b)	3.768 (a)	3.203 (a)
$a_1[K^{-2}](\times 10^{-8})$	1.42 (c)	1.42 (c)	0.2787 (a)	0.2787 (a)	0.165 (b)	0.165 (b)	0.7404 (a)	0.6293 (a)
$a_2[K]$	0. (c)	0. (c)	-0.5521 (a)	-0.5521 (a)	0. (b)	0. (b)	-0.7446 (a)	0. (a)
$G_0[GPa]$	124 (h)	79 (h)	85 (d)	85 (d)	175 (d)	138 (d)	130 (d)	47 (d)
$G'[-]$	1.4 (h)	0.6 (h)	1.4 (d)	1.4 (d)	1.7 (d)	1.7 (d)	2.2 (d)	0.7 (d)
$K_0[GPa]$	184 (h)	200 (h)	159.8 (e)	159.8 (e)	251 (d)	281 (d)	161 (d)	179 (d)
$K'[-]$	4.4 (h)	4.4 (h)	4.9 (e)	4.9 (e)	4.1 (d)	4.1 (d)	3.9 (d)	4.9 (d)
$\gamma_0[-]$	1.09 (d)	1.17 (d)	0.97 (d)	0.97 (d)	1.44 (d)	1.44 (d)	1.50 (d)	1.53 (d)
$q[-]$	2.8 (d)	2.8 (d)	1.5 (d)	1.5 (d)	1.4 (d)	1.4 (d)	1.5 (d)	1.5 (d)
$(\frac{\partial K}{\partial T})_P[GPaK^{-1}]$	-0.028 (f)	-0.028 (f)	-0.020 (d)	-0.026 (d)	-0.025 (e)	-0.075 (e)	-0.031 (d)	-0.029 (d)
$(\frac{\partial G}{\partial T})_P[GPaK^{-1}]$	-.014 (d)	-.014 (d)	-.014 (d)	-.014 (d)	-.014 (d)	-.014 (d)	-.017 (d)	-.017 (d)

Table 5.5: Mineral physics data at ambient PT-conditions from (a) Fei (1995), (b) Mattern et al. (2005), (c) Katsura et al. (2004), (d) Stixrude and Lithgow-Bertelloni (2007) and references therein, (e) Piazzoni et al. (2007), (f) Matsui et al. (2006), (g) Weidner and Wang (1998), (h) Higu et al. (2006),

The bulk and shear modulus at high temperature conditions are calculated by applying the following isobaric extrapolation (Anderson and Isaak (1995)):

$$K(T_f,P_0) = K_0 \left(\frac{\rho(T_f,P_0)}{\rho_0} \right)^{\delta S_0} \tag{5.9}$$

$$G(T_f,P_0) = G_0 + \left(\frac{\partial G}{\partial T} \right)_P (T_f - T_0), \tag{5.10}$$

with δS_0 the Anderson-Grüneisen parameter.

For compression to high pressure conditions we use adiabatic finite strain theory, with a high-temperature isentropic third-order Birch-Murnagham equation of state (Birch (1952)). The pressure, P, Eulerian strain, ε, density, ρ, and seismic velocities are related through (Davies and Dziewonski (1975)):

$$P = -(1-2\varepsilon)^{5/2} \left(C_1\varepsilon + \frac{C_2}{2}\varepsilon^2 + \frac{C_3}{6}\varepsilon^3 \right) \tag{5.11}$$

$$\rho v_p^2 = K + \frac{4G}{3} = (1-2\varepsilon)^{5/2} \left(L_1 + L_2\varepsilon + \frac{L_3}{2}\varepsilon^2 \right) \tag{5.12}$$

$$\rho v_s^2 = G = (1-2\varepsilon)^{5/2} \left(M_1 + M_2\varepsilon + \frac{M_3}{2}\varepsilon^2 \right) \tag{5.13}$$

$$v_\phi^2 = v_p^2 - \frac{4}{3}v_s^2 \tag{5.14}$$

with

$$\rho(T,P) = \rho(T_f,P_0)(1-2\varepsilon)^{3/2}. \tag{5.15}$$

We assume full relaxation of the deviatoric stress, appropriate for convecting mantle material (Stacey (2005)). In this case the average density of a mineralogical mixture is calculated as the volumetric average of the individual component and elastic parameters are determined using the Voigt-Reuss-Hill average.

The final temperature at high pressure conditions, T_{end}, is extrapolated adiabatically to high pressure conditions from the foot of the adiabat (e.g. Anderson (1989)):

$$T_{end} = T_f \exp\left[\frac{\gamma_0(1-(\rho_0/\rho)^q)}{q} \right]. \tag{5.16}$$

The constants C_i, M_i, and L_i in equations 5.11-5.14 are calculated from the elastic moduli and their pressure derivatives at ambient conditions as follows (Davies and Dziewonski (1975)):

$$C_1 = 3K_0 \tag{5.17}$$
$$C_2 = 9K_0(4-K_0') \tag{5.18}$$
$$C_3 = 27K_0\left(K_0K_0'' - K_0'(7-K_0') + 143/9\right) \tag{5.19}$$
$$M_1 = G_0 \tag{5.20}$$
$$L_1 = K_0 + \frac{4}{3}G_0 \tag{5.21}$$
$$M_2 = 5M_1 - 3G_0'K_0 + 5L_1 \tag{5.22}$$
$$L_2 = 5L_1 - 3K_0(K_0' + \frac{4}{3}G_0') \tag{5.23}$$
$$M_3 = 5M_1(3K_0'-5) - 3M_2(K_0'-4) + 9G_0''K_0^2 \tag{5.24}$$
$$L_3 = 5L_1(3K_0'-5) - 3L_2(K_0'-4) + 9K_0^2(K_0'' + \frac{4}{3}G_0'') \tag{5.25}$$

The Eulerian strain, ε, is calculated at high pressure conditions by inverting Eq. (5.11) numerically. We assumed temperature-independence for the first pressure derivatives of the elastic moduli, K' and G', at ambient pressure. This assumption is justified by the demonstrated low values of $\partial K'/\partial T$ (Jackson (1998); Li et al. (2005)) and uncertainties in $\partial G'/\partial T$ (see Matas et al. (2007) and references therein). K'' is related to K and K' through Eq. (14) by assuming $C_3 = 0$. To find G'', we use a linear relationship based on Stacey's emperical law for a mantle adiabat, i.e. $G''(T_f) = AK''(T_f)$ with $A = 0.631$ (Stacey (1992)).

Seismic sensitivities are calculated by differentiation of equations 5.13-5.14 with respect to T or X (Trampert et al. (2001)). This results in

$$\frac{\partial \ln v}{\partial Z} = \frac{1}{2\rho v^2}\left[\left(\frac{\partial M}{\partial Z}\right) - v^2\left(\frac{\partial \rho}{\partial Z}\right)\right], \tag{5.26}$$

where Z stands for either T or X, and M for K or G. The quantities ρ, v, K, and G are average values for a mineralogical mixture. The partial derivatives of elastic moduli and density that appear in the above expressions are evaluated using finite difference of values calculated at slightly different conditions for temperature and volumetric proportion of iron and perovskite. We calculate the seismic sensitivity to mineral phase from the seismic velocity for different end-member mineral phases at constant pressure and assume a linear dependence of seismic velocity on the phase parameter Γ_{ph} (Stixrude and Lithgow-Bertelloni (2007)).

Chapter 6

Concluding remarks

The implications of the results of the convection modelling described in chapters 3, 4, and 5 of this thesis are discussed below, together with suggestions for future research. The central theme of this thesis is to understand how the mantle convects as a compositionally heterogeneous entity on a time scale of the age of the Earth. The related sub-problems concern the formation of compositionally distinct mantle domains, their subsequent evolution, and the expression in the present-day state of mantle convective structure. To address these questions, we performed a series of numerical modelling studies of thermo-chemical mantle convection. To evaluate the modelling results against observational constraints from different research disciplines, synthetic data was extracted from the convection models, including excess temperatures and chemical heterogeneity of the upper mantle, the static component of the geoid, and the distribution of lateral variations in seismic wave velocity.

In Chapter 3, we obtained convection parameter values required for the survival of a compositionally distinct reservoir on a 4.5 *Gyr* time scale. Critical stability conditions occur in our models for a buoyancy number of $B = 0.1 - 0.15$, associated with an excess density of the reservoir of $\frac{\delta\rho_C}{\rho} \sim 1\%$ relative to the overlying mantle. The above values confirm previously established estimates obtained mostly from convection modelling in cartesian geometry (e.g. Kellogg et al. (1999); Davaille (1999); Hansen and Yuen (2000); Van Thienen et al. (2005); Deschamps et al. (2007)). For a reservoir that is critically stable on a billion-year time scale, most of the distinct material survives in the deep mantle in the form of isolated piles on top of the core-mantle boundary (CMB), but part of the material is entrained into and mixed with the overlying mantle. Due to the effect of ponding (or pooling) of slabs, an internal boundary layer grows at the endothermic post-spinel phase transformation near 660 *km* depth, which destabilises rather abruptly when critical gravitational stability is reached (Solheim and Peltier (1994)). As a result, convective downwellings enter the lower mantle with increased convective vigour (inducing intense mixing) but occur at a decreased frequency (due to long periods of predominantly layered convective circulation) (Ma-

chetel and Weber (1991); Solheim and Peltier (1994)). In our models, the combined effects of slab ponding are in favour of gravitational stabilisation of a deep mantle reservoir, of which the long-term survival becomes feasible at a lower excess density relative to the overlying mantle. The above scenario with slabs ponding at the 660 *km* phase boundary is consistent with deflection of slabs at the base of the upper mantle inferred from seismic tomography imaging (Van der Hilst et al. (1991); Fukao et al. (1999)).

We investigated in more detail than Weinstein (1992) the deflection of intrinsically dense material entrained in convective upwellings underneath the endothermic phase transition, prior to potential further ascent into the upper mantle. Due to compositional filtering, the shallow lower mantle becomes compositionally heterogeneous in the convection models, which may explain recent seismic inversion results (Trampert et al. (2004)). Convective upwellings that originate from the heterogeneous shallow lower mantle would have a compositionally heterogeneous signature for a wide range of reservoir stability conditions and transition zone layering. Therefore, it is difficult to distinguish between different configurations or stability conditions of an isolated mantle reservoir based on the chemical signature of MORB and OIB alone. The opposite is also true: for a wide range of thermo-chemical mantle convection parameters upwellings of lower mantle origin show a compositionally heterogeneous signature, consistent with a chemically heterogeneity observed in OIB (e.g. Hofmann (1997)). The above results illustrate the important control of the transition zone on the transport of compositional heterogeneity from the deep mantle to the surface. Tomographic images of plume-like structures have been reported (Bijwaard and Spakman (1999); Antolik et al. (2003); Nolet et al. (2007)), but the interaction of convective upwellings with the upper-lower mantle boundary cannot at present be resolved by seismic tomography. Currently available geochemical, and petrological evidence for the depth of origin of mantle upwellings is not conclusive either (Hofmann (1997); Lyubetskaya and Korenaga (2007); McCammon (2001); Spengler et al. (2006)).

Our modelling results show that regional and transient convective layering produces a temperature constrast across the post-spinel phase transition which, in turn, results in an increase of excess temperatures in upwellings that enter the upper mantle. At low degrees of mantle flow layering at the endothermic post-spinel phase transition, synthetic excess temperatures in upwellings are consistent with petrologically determined excess temperatures estimated for present-day intra-plate volcanism, including the combined existence of hotspots and large igneous provinces (LIP). More difficult to reconcile with observational data are models with a strong degree of convective layering that produce upwellings of high excess temperatures that can produce massive flood basalt volumes. Our results are thus suggestive of a relatively low degree of convective layering.

The synthetic gravity calculations of Chapter 4 show that the existence of large-scale compositional heterogeneity in the lower mantle cannot be refuted on the basis

of the static component of the geoid. It is difficult to draw more specific conclusions from the convection results because of the non-unique nature of the geoid inversion problem and the trade-off effects of temperature and density of a thermo-chemical reservoir. For the same reasons, geoid and dynamic topography analyses cannot rule out models of purely thermal or thermally dominated mantle convection (Forte and Mitrovica (2001); Čadek and Fleitout (2006)). A recent geoid inversion study shows the viability for compositionally distinct domains in the lower mantle (Simmons et al. (2007)) but it does not, however, require the existence of such domains. The long wave-length geoid is already determined with a high precision, but new insights could follow from more accurate determination of surface dynamic topography, on which there is currently no consensus (Wheeler and White (2000); Forte and Perry (2000); Panasyuk and Hager (2000b); Sandiford (2007)). More accurate determination of the topography of the core-mantle boundary (Redkal and Doornbos (1992); Garcia and Souriau (2000); Sze and van der Hilst (2003)) would also help constrain convection models (Lassak et al. (2007)).

In Chapter 5, we analysed the synthetic seismic expression of compositional mantle heterogeneity by employing a combined analysis of anomalies in density (ρ), shear wave (v_S) and bulk sound velocity (v_ϕ), and a more detailed analysis of the shallow lower mantle. For the model with large-scale thermo-chemical piles on top of the CMB, the synthetic data shows a negative or strongly reduced correlation between v_S-v_ϕ and v_S-ρ anomalies in the deep mantle, in good agreement with seismological constraints (e.g. Masters et al. (2000); Saltzer et al. (2001); Ishii and Tromp (2004)). In contrast, none of the iso-chemical models or models with a globally continuous layering that we investigated show a successful match to the seismological observations. Models with a rather small deep mantle reservoir volume of 10 vol% or less agree best with the amplitudes of the seismic velocity anomalies inferred from seismology. Reservoir volumes of this size are consistent with recent geochemical mass balance studies (Tolstikhin et al. (2006); Lyubetskaya and Korenaga (2007)).

Based on a comparison with tomographic data, the results are suggestive of an upper bound for the present-day core temperature, preliminarily put at a value of $\sim 3500K$. This value falls within the range of uncertainty in CMB temperature estimates from experimental and theoretical calculations (Alfè et al. (2007), R. Boehler, personal communication) and can be reconciled with lower bounds for the CMB temperature based on the occurrence of double crossings of the post-perovskite phase boundary that serve as a deep mantle thermometer (e.g. Hernlund et al. (2005); Hirose (2006); Lay et al. (2006); Van der Hilst et al. (2007)). For our preferred model the CMB heat flux falls between inferred bounds for CMB heat flux of 1 and 10 TW (e.g. Christensen and Tilgner (2004); Lay et al. (2008)).

Phase transformations at the upper-lower mantle boundary have a strong local control on the synthetic seismic wavespeed signature in a layer less than 100 km thick near 660 km depth in the convection model. Locally, contributions to the seismic

signature from phase transformations exceed those from thermal or compositional anomalies, which is consistent with predictions from mineral physics (Stixrude and Lithgow-Bertelloni (2007)). The local, high amplitude seismic velocity anomalies of metamorphic origin will smear over 100's of kilometers radially in seismic tomography images and entangle with anomalies of thermal and compositional origin. Although this severely complicates interpretation of seismic images, future advances in seismic imaging may help to elucidate the convection processes in the transition zone region.

We have put our models in perspective with proposed formation processes for a deep mantle reservoir by investigating the seismic expression of distinct reservoirs of different petrological origin. Early differentiation of mantle domains has been suggested by geochemical isotope dating (Allègre and Lewin (1995); Blichert-Toft et al. (1999); Caro et al. (2004)) and such a reservoir can have formed in the early hot Earth by delamination of eclogite from a thick basaltic crust (Vlaar et al. (1994)) or episodic rapid sinking of 1000km segments of crust (Van Thienen et al. (2005); Tolstikhin et al. (2006)). A deep mantle reservoir originating from former basaltic crust is expected to be enriched in iron and silica and has a density above the lateral average (e.g. Ono et al. (2005); Perrillat et al. (2006)). Our results show that for such a scenario the synthetic seismic signature of the lowermost mantle is in general agreement with the seismic tomography data. Formation by differential crystallisation of perovskite-rich material in a magma ocean (Walter et al. (2004)) is possible, but our modelling results show that additional iron is required to match the seismological observations. This process is less straightforward, but viable if significant amounts of iron are added to the deep mantle by accumulation of former basaltic crust, interaction with the core (e.g. Mao et al. (2005)), or both.

In conclusion, the results presented in this thesis are interpreted as follows. Large-scale compositional heterogeneity that formed early in Earth's evolution can survive for billions of years in a mantle subject to convective overturn. Thermo-chemical models evolved this way are more successful than purely thermal models in fitting observational data from different research disciplines, specifically: the upper mantle excess temperature and compositional heterogeneity, the static part of the geoid, and lateral variations in seismic wave velocity. The shallow lower mantle is identified as a key region for future testing, because the counterpart of deep mantle compositional heterogeneity residing in this region serves as an indicator for the degree of convective layering at the transition zone. The preferred mantle convection model that emerges from this thesis is characterised by compositionally distinct domains that occupy a moderate fraction of the mantle volume and which are configured as critically stable piles residing on top of the CMB, with a counterpart underneath the upper-lower mantle boundary at which convective upwellings become deflected and are modulated both thermally and chemically, before reaching the upper mantle.

Summary

In modern geoscience, mounting evidence in support of large-scale lateral variations in the composition of Earth's deep mantle has fueled the debate on the style and evolution of mantle convection. Seismological data supports the view that material transport across the mantle transition zone is significant. On the other hand, complete homogenisation of the entire mantle by convective overturn is argued against by geochemical data suggestive of long-lived compositionally distinct domains and seismological evidence for large-scale lateral variations in the composition of the lowermost mantle. It has become difficult to integrate the observational data with models of "layered convection" and "whole mantle convection", which are end-member models characterised by (piece-wise) iso-chemical layers that are well-mixed internally by convective overturn. More successful in reconciling the observational data is a model of thermo-chemical convection, with large-scale lateral variation in the deep mantle imposed by compositionally distinct reservoirs (e.g. Kellogg et al. (1999); Tackley (2002)). Nevertheless, validation of this model is difficult because of uncertainties in the parameters that determine deep mantle convection.

In this thesis, we try to understand how the mantle has evolved as a compositionally heterogeneous entity on the billion-year time-scale of the age of the Earth (4.5 billions of years). Relevant sub-problems are: Can the existence of compositionally distinct domains in the present-day deep mantle be reconciled with geochemical, gravity, and seismological data? How can a compositionally distinct reservoir survive on a billion year time-scale in the deep mantle? How is the convective evolution affected by material transport at the mantle discontinuity near 660 km depth? Is it possible to discriminate between previously proposed processes for the formation of large-scale compositionally distinct reservoirs in the deep mantle?

To address these research questions, we perform a series of numerical modelling studies of thermo-chemical convection of the Earth's mantle. Synthetic data is then extracted from the modelling results for comparison with available observational data. The different "observables" considered this way are: excess temperatures in and chemical heterogeneity of the upper mantle, long wave-length gravity signals, and the distribution of lateral variations in seismic wave velocity.

The conclusions derived from this thesis are summarised as follows. Large-scale

compositional heterogeneity that formed early in Earth's evolution can survive for billions of years in a mantle subject to convective overturn. Thermo-chemical models evolved this way are more successful than iso-chemical models in fitting observational data from different research disciplines. The shallow lower mantle is identified as a key region for future testing, because the counterpart of deep mantle compositional heterogeneity residing in this region serves as an indicator for the degree of convective layering at the transition zone –an important parameter to understand the thermal and compositional evolution of the Earth. The preferred mantle convection model that emerges from this thesis is characterised by compositionally distinct domains that occupy a moderate fraction of the mantle volume and which are configured as critically stable piles residing on top of the core-mantle boundary, with a counterpart underneath the upper-lower mantle boundary at which convective upwellings become deflected and are modulated both thermally and chemically, before reaching the upper mantle.

Samenvatting (Summary in Dutch)

Het hedendaagse aardwetenschappelijke debat met betrekking tot de structuur en de evolutie van mantelconvectie wordt gevoed door toenemend bewijs voor grootschalige laterale variaties in de samenstelling van de diepe mantel van de aarde. Enerzijds ondersteunen seismologische gegevens de opvatting dat een significante hoeveelheid materiaal de transitiezone van de mantel doorkruist. Dit suggereert dat de boven- en ondermantel geen strikt gescheiden reservoirs zijn. Anderzijds lijkt een volledige homogenisatie van de gehele mantel door middel van convectieve circulatie in strijd met zowel geochemische data (die lang-bestaande compositioneel afwijkende domeinen suggereren) als seismologische aanwijzigingen voor grootschalige laterale compositievariaties in de diepste regionen van de mantel. Het wordt steeds moeilijker om deze observaties te verklaren met behulp van modellen van "gelaagde convectie" en "hele-mantelconvectie", wat de limietgevallen zijn gekarakteriseerd door (stukwijs) iso-chemische lagen die intern goed gemengd worden middels convectieve circulatie. Een model dat beter slaagt in het verklaren van de observaties is dat van thermo-chemische convectie, waarin grootschalige laterale samenstellingsvariaties in de diepe mantel worden veroorzaakt door compositioneel afwijkende reservoirs (bv. Kellogg et al. (1999); Tackley (2002)). Desalniettemin is het moeilijk om dit model te valideren vanwege grote onzekerheden in parameters die bepalend zijn voor convectie in de diepe mantel.

In dit proefschrift wordt de hypothese getest dat de mantel evolueerde als een compositioneel heterogene eenheid op een tijdschaal die karakteristiek is voor de ouderdom van de aarde (4.5 miljard jaar). Relevante deelproblemen die aandacht vereisen zijn de volgende: Kan het bestaan van compositioneel afwijkende domeinen in de huidige diepe mantel in overeenstemming worden gebracht met geochemische, zwaartekrachts- en seismologische data? Hoe kunnen compositionele heterogeniteiten op een tijdschaal van miljarden jaren overleven in de diepe mantel? Hoe wordt de convectieve evolutie beïnvloed door materiaaltransport door de manteldiscontinuiteit op een diepte van ongeveer 660 km? Is het mogelijk om eerder voorgestelde formatieprocessen voor grootschalige compositionele heterogeniteiten in de diepe mantel van elkaar te onderscheiden?

Voor het beantwoorden van bovenstaande onderzoeksvragen wordt een serie van

numerieke modelexperimenten uitgevoerd van thermo-chemische mantelconvectie. Vervolgens worden synthethische data van de modelresultaten afgeleid en vergeleken met beschikbare observationele data. De ”observationele” signalen die op deze manier worden behandeld zijn: de thermische en chemische structuur van de bovenmantel, langgolvige zwaartekrachtssignalen en de distributie van seismische golfsnelheden.

De conclusies die worden ontleend aan dit promotieonderzoek kunnen als volgt worden samengevat: Grootschalige compositionele heterogeniteiten die gevormd werden in een vroeg stadium van de aardevolutie kunnen mantelcirculatie miljarden jaren lang overleven. Thermo-chemische modellen die op deze manier zijn geëvolueerd slagen er beter in om observaties van diverse onderzoeksdisciplines te verklaren dan iso-chemische modellen. De ondiepe ondermantel is een cruciale regio voor verder onderzoek, omdat een afsplitsing van de compositionele heterogeneiteiten uit de diepe mantel die zich hier ophouden als een indicator dienen voor de mate van convectieve gelaagdheid op de transitiezone –een belangrijke parameter voor het begrijpen van de thermische en compositionele evolutie van de aarde. Het te verkiezen model voor mantelconvectie dat voortkomt uit dit promotie-onderzoek wordt gekenschetst door compositioneel distincte domeinen die een beperkte fractie van het totale mantelvolume beslaan, een kritieke stabiliteit hebben en als afzonderlijke stapels opeenhopen boven de kern-mantelgrens, met een afgesplitst deel dat zich ophoudt onder de grens tussen de boven- en ondermantel, alwaar convectieve opwaartse stromingen worden afgebogen en zowel thermisch als chemisch worden gemoduleerd alvorens deze de bovenmantel bereiken.

Bibliography

Abe, Y. (1996). Thermal and chemical evolution of the terrestrial magma ocean. *Earth Planet. Sci. Lett.*, 100:27–39.

Albarède, F. and Van der Hilst, R. D. (1999). New mantle convection model may reconcile conflicting evidence. *EOS. Trans. AGU*, 45:535–539.

Albarède, F. and Van der Hilst, R. D. (2002). Zoned mantle convection. *Philos. Trans. R. Soc. Lond. A*, 360:2569–2592.

Alfè, D., Gillian, M. J., and Price, G. D. (2007). Temperature and composition of the Earth's core. *Contemporary Physics*, 48(2):63–80.

Allègre, C. J. and Lewin, E. (1995). Isotopic systems and stirring times of the Earth's mantle. *Earth Planet. Sci. Lett.*, 136:629–646.

Anderson, D. L. (1989). Theory of the Earth. *Blackwell Scientific Publications*.

Anderson, D. L. (2006). Speculations on the nature and cause of mantle heterogeneity. *Tectonophysics*, 416:7–22.

Anderson, O. L. and Isaak, D. G. (1995). Elastic Constants of Mantle Minerals at High Temperature. *Mineral Physics and Crystallography: A Handbook of Physical Constants (AGU reference shelf 2) Ed. T.J. Ahrens*, pages 64–97.

Antolik, M., Gu, Y. J., Ekström, G., and Dziewonski, A. M. (2003). J362D28: a new joint model of compressional and shear velocity in the Earth's mantle. *Geophys. J. Int.*, 153:443–456.

Auzende, A., Badro, J., Ryerson, F. J., Weber, P. K., Fallon, S. J., Addad, A., Siebert, J., and Fiquet, G. (2008). Element partitioning between magnesium silicate perovskite and ferropericlase: New insights into bulk lower-mantle geochemistry. *Earth Planet. Sci. Lett.*, 269:164–174.

Badro, J., Rueff, J., Vanko, G., Monaco, G., Fiquet, G., and Guyot, F. (2004). Electronic transitions in perovskite: possible nonconvecting layers in the lower mantle. *Science*, 305:383–386.

Becker, T. W., Kellogg, J. B., and O'Connell, R. J. (1999). Thermal constraints on the survival of primitive blobs in the lower mantle. *Earth Planet. Sci. Lett.*, 171:351–365.

Bercovici, D. and Karato, S. I. (2003). Whole-mantle convection and the transition-zone water filter. *Nature*, 425:39–44.

Bercovici, D., Schubert, G., and Tackley, P. J. (1993). On the penetration of the 660 km phase change by mantle downflows. *Geophys. Res. Lett.*, 23:2599–2602.

Biggin, A. J., Strik, G. H. M. A., and Langereis, C. G., F. (2008). Evidence for a very-long-term trend in geomagnetic secular variation. *Nature Geoscience*, 1:395–398.

Bijwaard, H. and Spakman, W. (1999). Tomographic evidence for a narrow whole mantle plume below Iceland. *Earth Planet. Sci. Lett.*, 166:121–126.

Birch, F. (1952). Elasticity and and constitution of the Earth's interior. *J. Geophys. Res.*, 57:227–286.

Blankenbach, B., Busse, F., Christensen, U., Cserepes, L., Gunkel, D., Hansen, U., Harder, H., Jarvis, G., Koch, M., Marquart,

G., Moore, D., Olson, P., Schmeling, H., and Schnaubelt, T. (1989). A benchmark comparison for mantle convection codes. *Geophys. J. Int.*, 98:23–38.

Blichert-Toft, J., Albarède, F., Rosing, M., Frei, R., and Bridgwater, D. (1999). The Nd and Hf isotopic evolution of the mnatle through the Archean. Results from the Ishua supracrustals, West Greenland and from the Birimian terranes of West Africa. *Geochim. et Cosmochim. Acta*, 63(22):3901–3914.

Boehler, R. (2000). High-pressure experiments and the phase diagram of lower mantle and core materials. *Rev. Geophys.*, 38:221–245.

Boyet, M. and Carlson, R. W. (2005). 142-Nd Evidence for Early (¿4.53 Ga) Global Differentiation of the Silicate Earth. *Science*, 309:576–581.

Buffett, B. A. (2000). Dynamics of the earth's core. *AGU Geophysical Monograph*, 117:37–62.

Bukowinski, M. S. T. and Akber-Knutson, S. (2005). The Role of Theoretical Mineral Physcis in Modeling the Earth's Interior In: Van der Hilst R. D., Bass, J., Trampert, J. (Eds). *Earth's Deep Mantle: Structure, Composition, and Evolution, AGU Geophysical Monograph)*, 160:137–163.

Bunge, H.-P. (2005). Low plume excess temperatures and high core heat flux inferred from non-adiabatic geotherms in internally heated mantle circulation models. *Phys. Earth Planet. Int.*, 153:3–10.

Bunge, H. P., Richards, M. A., and Baumgardner, J. R. (1997). A sensitivity study of three-dimensional spherical mantle convection at 10(8) Rayleigh number: Effects of depth-dependent viscosity, heating mode, and an endothermic phase change. *J. Geophys. Res.*, 102(B6):11991–12007.

Čadek, O. and Fleitout, L. (2003). Effect of lateral viscosity variations in the top 300 km on the geoid and dynamic topography. *Geophys. J. Int.*, 152(3):566–580.

Čadek, O. and Fleitout, L. (2006). Effect of lateral viscosity variations in the core-mantle boundary region on predictions of the long-wavelength geoid. *Studia Geophysica et Geodaetica*, 50(2):217–232.

Čadek, O. and Van den Berg, A. P. (1998). Radial profiles of temperature and viscosity in the Earth's mantle inferred from the geoid and lateral seismic structure. *Earth Planet. Sci. Lett.*, 164:607–615.

Čadek, O., Yuen, D. A., Čížková, H., Kido, M., Zhou, H., Brunet, D., and Machetel, P. (1998). New perspectives on Mantle Dynamics from High-resolution Seismic Tomographic Model P1200. *Pure Appl. Geophys.*, 151:503–525.

Campbell, I. H. (2007). Testing the plume theory. *Chem. Geol.*, 24:153–126.

Caro, G., Bourdon, B., Birck, J. L., and Moorbath, S. (2004). ^{146}Sm-^{142}Nd evidence from Isua metamorphosed sediments for early differentiation of the Earth's mantle. *Nature*, 423:428–432.

Castle, J. C. and Van der Hilst, R. D. (2003). Searching for seismic scattering off mantle interfaces between 800 km and 2000 km depth. *J. Geophys. Res.*, 108(B2):2095, doi:10.1029/2001JB000286.

Chopelas, A. and Boehler, R. (1992). Thermal expansivity in the lower mantle. *Geophys. Res. Lett.*, 19(19):1983–1986.

Christensen, U. R. (1989). Models of mantle convection: one or several layers. *Philos. Trans. R. Soc. Lond. A*, 328:417–424.

Christensen, U. R. (1998). Dynamic phase boundary topography by latent heat effects. *Earth Planet. Sci. Lett.*, 154:295–306.

Christensen, U. R. and Hofmann, A. W. (1994). Segregation of subducted oceanic crust in the convecting mantle. *J. Geophys. Res.*, 99(B10):19,867–19,884.

Christensen, U. R. and Tilgner, A. (2004). Power requirement of the geodynamo from ohmic losses in numerical and laboratory dynamos. *Nature*, 429:168–171.

Christensen, U. R. and Yuen, D. A. (1984). The interaction of a subducting lithospheric slab with a chemical or phase boundary. *J. Geophys. Res.*, 89(B6):4389–4402.

Christensen, U. R. and Yuen, D. A. (1985). Layered Convection Induced by Phase Transitions. *J. Geophys. Res.*, 90(B12):10291–10300.

Čížková, H., Čadek, O., van den Berg, A. P., and Vlaar, N. J. (1999). Can Lower Mantle Slab-like Seismic Anomalies be Explained by Thermal Coupling Between the Upper and Lower Mantles. *Geophys. Res. Lett.*, 26(10):1501–1504.

Čížková, H. and Matyska, C. (2004). Layered convection with an interface at a depth of 1000 km: stability and generation of slab-like downwellings. *Phys. Earth Planet. Int.*, 141:269–279.

Condie, K. C. (1999). Episodic continental growth models: afterthoughts and extensions. *Tectonophysics*, 322:153–162.

Corrieu, V., Ricard, Y., and Froideveaux, C. (1994). Converting mantle tomography into mass anomalies to predict the Earth's radial viscosity. *Phys. Earth Planet. Int.*, 184(1-4):3–13.

Cserepes, L. and Yuen, D. A. (2000). On the possibility of a second kind of mantle plume. *Earth Planet. Sci. Lett.*, 183:61–71.

Cuvelier, C., Segal, A., and van Steenhoven, A. A. (1986). Finite Element Methods and Navier-Stokes Equations. *Reidel Publishing Company, Dordrecht, Holland.*

Davaille, A. (1999). Simultaneous generation of hotspots and superswells by convection in a heterogeneous planetary mantle. *Nature*, 402:756–760.

Davies, G. F. (1986). Mantle convection under simulated plates: effects of heating modes and ridge and trench migration, and implications for the core-mantle boundary, bathymetry, the geoid and Benioff zones. *Geophys. J. R. Astron. Soc.*, 84:153–183.

Davies, G. F. and Dziewonski, A. M. (1975). Homogeneity and constitution of the Earth's lower mantle and outer core. *Phys. Earth Planet. Int.*, 10:336–343.

De Smet, J., Van den Berg, A. P., and Vlaar, N. J. (2000). Early formation and long-term stability of continents resulting from decompression melting in a convecting mantle. *Tectonophysics*, 322:19–33.

DePaolo, D. J. and Manga, M. (2003). Deep Origin of Hotspots – the Mantle Plume Model. *Science*, 300:920–921.

Deschamps, F. and Trampert, J. (2003). Mantle tomography and its relation to temperature and composition. *Phys. Earth Planet. Int.*, 140:227–291.

Deschamps, F., Trampert, J., and Tackley, P. J. (2007). Thermo-chemical structure of the lower mantle: seismological evidence and geodynamical consequences. *'Superplume: Beyond Plate Tectonics', D. A. Yuen, S. Maruyama, S. I. Karato, and B. F. Windley (Eds)*, pages 293–320.

Deuss, A., Redfern, S. A. T., Chambers, K., and Woodhouse, J. H. (2006). The Nature of the 660-Kilometer Discontinuity in Earth's Mantle from Global Seismic Observation of PP Precursors. *Science*, 311:198–201.

Dziewonski, D. L. and Anderson, D. L. (1981). Preliminary reference Earth model. *Phys. Earth Planet. Int.*, 25:297–356.

Farnetani, C. G. (1997). Excess temperatures of mantle plumes: The role of chemical stratification across D". *Geophys. Res. Lett.*, 24(13):1583.

Farnetani, C. G. and Richards, M. A. (1994). Numerical investigations of the mantle plume initiation model for flood basalt events. *J. Geophys. Res.*, 99(B7):13,813–13,833.

Fei, Y. (1995). Thermal Expansion. *Mineral Physics and Crystallography: A Handbook of Physical Constants (AGU reference shelf 2) Ed: T.J. Ahrens*, pages 29–44.

Fei, Y., van Orman, J., Li, J., van Westre-

nen, W., Sanloup, C., Minarik, W., Hirose, K., Kombayashi, T., and Walter, M. (2004). Experimentally determined postspinel transformation boundary in Mg2SiO4 using MgO as an internal pressure standard and its geophysical implications. *J. Geophys. Res.*, 109:B02305.

Fischer, K. M., Jordan, T. H., and Creager, K. C. (1988). Seismic constraints on the morphology of deep slabs. *J. Geophys. Res.*, 93:4773–4783.

Forte, A. M. and Mitrovica, J. X. (2001). Deep-mantle high-viscosity flow and thermochemical structure inferred from seismic and geodynamic data. *Nature*, 410:1049–1056.

Forte, A. M. and Peltier, W. R. (1991). Mantle convection and core mantle boundary topography - Explanations and implications. *Tectonophysics*, 187(1-3):91–116.

Forte, A. M. and Perry, H. K. C. (2000). Geodynamic Evidence for a Chemically Depleted Continental Tectosphere. *Science*, 290:1940–1944.

Frost, D. J. (2003). Fe^{2+}-Mg partitioning between garnet, magnesiowüstite, and $(Mg,Fe)_2SiO_4$ phases of the transition zone. *American Mineralogist*, 88:387–397.

Fukao, Y., Widiyantoro, S., and Obayashi, M. (1999). Stagnant slabs in the upper and lower mantle transition region. *Rev. Geophys.*, 39(3):291–323.

Garcia, R. and Souriau, A. (2000). Amplitude of the core-mantle boundary topography estimated by stochastic analysis of core phases. *Phys. Earth Planet. Int.*, 117:345–359.

Goes, S., Cammarano, F., and Hansen, U. (2004). Synthetic seismic signature of thermal mantle plumes. *Earth Planet. Sci. Lett.*, 218:403–419.

Goes, S., Govers, R., and Vacher, P. (2000). Shallow mantle temperatures under Europe from P and S wave tomography. *J. Geophys. Res.*, 105:11,153–11,169.

Grand, S. P., Van der Hilst, R. D., and Widiyantoro, S. (1997). Global seismic tomography: a snapshot of convection in the Earth. *Geol. Soc. Am. Today*, 7:1–7.

Green, D. H. and Falloon, T. J. (1998). Pyrolite: A Ringwood Concept and Its Current Expression. *In: The Earth's Mantle, I. Jackson (Ed)*, pages 311–378.

Green, D. H., Falloon, T. J., M., E. S., and M., Y. G. (2001). Primary magmas and mantle temperatures. *European Journal of Mineralogy*, 13(3):437–451.

Gu, Y. J. and Dziewonski, A. M. (1999). Mantle Discontinuities and 3-D Tomographic Models. *EOS. Trans. AGU*, 80(F717).

Gu, Y. J., Dziewonski, A. M., and Ekström, G. (2003). Simultaneous inversion for mantle shear velocity and topography of transition zone discontinuities. *Geophys. J. Int.*, 154:559–583.

Gurnis, M. (1993). Phanerozoic marine inundation of continents driven by dynamic topography above subducting slabs. *Nature*, 364:589–593.

Hager, B. (1984). Subducted Slabs and the Geoid: Constraints on Mantle Rheology and Flow. *J. Geophys. Res.*, 89(B7):6003–6015.

Hansen, U. and Yuen, D. A. (2000). Extended-Boussinesq thermal-chemical convection with moving heat sources and variable viscosity. *Earth Planet. Sci. Lett.*, 176:401–411.

Hansen, U., Yuen, D. A., Kroenings, S. E., and Larsen, T. B. (1993). Dynamic consequences of depth-dependent thermal expansivity and viscosity on mantle circulations and thermal structure. *Phys. Earth Planet. Int.*, 77(3-4):205–223.

Haskell, N. A. (1935). The motion of a viscous fluid under a surface load. *Physics*, 6:265–269.

Helmberger, D. V. and Ni, S. (2005). Seismic Modeling Constraints on the South African Super Plume In: Van der Hilst R.

D., Bass, J., Trampert, J. (Eds). *Earth's Deep Mantle: Structure, Composition, and Evolution, AGU Geophysical Monograph*, 160:63–81.

Hernlund, J. W., Thomas, C., and Tackley, P. J. (2005). A doubling of the post-perovskite phase boundary and structure of the earth's lowermost mantle. *Nature*, 434(7035):882–886.

Herzberg, C., Asimow, P. D., Arndt, N., Niu, Y., Lesher, C. M., Fitton, J. G., and Cheadle, M. J. (2007). Temperatures in ambient mantle and plumes: Constraints from basalts, picrites, and komatiites. *Geochem. Geophys. Geosyst.*, 8:Q02006, doi:10.1029/2006GC001390.

Higu, Y., Inoue, T., Irifune, T., and Liebermann, R. C. (2006). The effects of iron on the elastic properties of ringwoodite at high pressure. *Phys. Earth Planet. Int.*, 159:276–285.

Hirose, K. (2002). Phase transitions in pyrolitic mantle around 670-km depth: Implications for upwelling plumes from the lower mantle. *J. Geophys. Res.*, 107(B4).

Hirose, K. (2006). Postperovskite phase transition and its geophysical implications. *Rev. Geophys.*, 44(RG3001):1–18.

Hirose, K., Fei, Y., Ma, Y., and Mao, H. K. (1999). The Fate of Subducted Basaltic Crust in the Earth's Lower Mantle. *Nature*, 397:53–56.

Hirose, K., Sinmyo, R., Sata, N., and Ohishi, Y. (2006). Determination of post-perovskite phase transition boundary in $MgSiO_3$ using Au and MgO pressure standards. *Geophys. Res. Lett.*, 33:doi:10.1029/2005GL024468.

Hockney, R. W. and Eastwood, J. W. (1988). Computer simulation using particles. *Institute of Physics Publishing Ltd., Bristol*.

Hofmann, A. W. (1997). Mantle geochemistry: the message from oceanic volcanism. *Nature*, 385:219–229.

Hofmeister, A. M. and Criss, R. E. (2005). Earth's heat flux revised and linked to chemistry. *Tectonophysics*, 395:159–177.

Hughes, T. J. R. (1987). The Finite Element Method - Linear Static and Dynamic Finite Element Analysis. *Dover Publications Inc.*

Irifune, T. and Ringwood, A. E. (1993). Phase transformations in subducted oceanic crust and buoyancy relationships at depths of 600-800 km in the mantle. *Earth Planet. Sci. Lett.*, 117:101–110.

Ishii, M. and Tromp, J. (1999). Normal-Mode and Free-Air Gravity Constraints on Lateral Variations in Velocity and Density of Earth's Mantle. *Science*, 285:1231–1236.

Ishii, M. and Tromp, J. (2004). Constraining large-scale mantle heterogeneity using mantle and inner core sensitive normal modes. *Phys. Earth Planet. Int.*, 146:113–124.

Ita, J. and King, S. D. (1994). Sensitivity of convection with an endothermic phase change to the form of governing equations, initial conditions, boundary conditions, and equation of state. *J. Geophys. Res.*, 99:15919–15938.

Ito, E. and Takahashi, E. (1989). Postspinel transformations in the system Mg2SiO4 and some geophysical implications. *Journal of Geophysics*, 94 (B8):10637–10646.

Ito, G. and Mahony, J. J. (2005). Flow and melting of a heterogeneous mantle: 1. Method and importance to the geochemistry of ocean island and mid-ocean ridge basalts. *Earth Planet. Sci. Lett.*, 230:29–46.

Jackson, I. (1998). Elasticity, composition and temperature of the Earth's lower mantle: a reappraisal. *Geophys. J. Int.*, 134:291–311.

Jacobs, M. H. G. and de Jong, B. H. W. S. (2007). Placing constraints on phase equilibria and thermophysical properties in the system MgO-SiO2 by a thermodynamically consistent vibrational method. *Geochim. et Cosmochim. Acta*, 71:3630–3655.

Jarvis, G. T. (1995). Curvature, heat flow and

normal stresses in two-dimensional models of mantle convection. *Phys. Earth Planet. Int.*, 88:17–29.

Jeanloz, R. and Lay, T. (1993). The core-mantle boundary. *Scientific American*, 268(5):48–55.

Jeanloz, R. and Morris, S. (1987). Is the mantle geotherm sub-adiabatic? *Geophys. Res. Lett.*, 14:335–338.

Kanda, R. V. S. and Stevenson, D. J. (2006). Suction mechanism for iron entrainment into the lower mantle. *Geophys. Res. Lett.*, 33:L02310.

Karato, S. and Karki, B. B. (2001). Origin of lateral variation of seismic wave velocities and density in the deep mantle. *J. Geophys. Res.*, 106(B10):21771–21783.

Katsura, T., Yokoshi, S., Song, M. S., Kawabe, K., Tsujimura, T., Kubo, A., Ito, E., Tange, Y., Tomioka, N., Saito, K., Saito, K., Nozawa, A., and Funakoshi, K. (2004). Thermal expansion of Mg2SiO4 ringwoodite at high pressures. *J. Geophys. Res.*, 109(B12):B12209.

Kellogg, J. B., Jacobsen, S. B., and O'Connell, R. J. (2007). Modeling lead isotopic heterogeneity in mid-ocean ridge basalts. *Earth Planet. Sci. Lett.*, 262(3-4):328–342.

Kellogg, L. H. (1991). Interaction of plumes with a compositional boundary at 670 km. *Geophys. Res. Lett.*, 18:865–868.

Kellogg, L. H., Hager, B. H., and Van der Hilst, R. D. (1999). Compositional Stratification in the Deep Mantle. *Science*, 283:1881–1884.

Kennett, B. L. N., , Widiyantoro, S., and Van der Hilst, R. D. (1998). Joint seismic tomography for bulk sound and shear wave speed in the Earth's mantle. *J. Geophys. Res.*, 103(B6):12,469–12,493.

Kennett, B. L. N. and Gorbatov, A. (2004). Seismic heterogeneity in the mantle – strong shear wave signature of slabs from joint tomography. *Phys. Earth Planet. Int.*, 146:87–100.

Kiefer, W. S. and Hager, B. H. (1992). Geoid anomalies and dynamic topography from convection in cylindrical geometry - applications to mantle plumes on Earth and Venus. *Geophys. J. Int.*, 96(E4):198–214.

Kiefer, W. S. and Kellogg, L. H. (1997). Geoid anomalies and dynamic topography from time-dependent, spherical axisymmetric mantle convection. *Phys. Earth Planet. Int.*, 106:237–256.

King, S. D. (1995). Radial models of mantle viscosity: results from a genetic algorithm. *Geophys. J. Int.*, 122:725–736.

King, S. D. and Hager, B. (1994). Subducted slabs and the geoid 1. Numerical experiments with temperature-dependent viscosity. *J. Geophys. Res.*, 99(B10):19843–19852.

Knittle, E. and Jeanloz, R. (1991). Earth's core-mantle boundary: results of experiments at high pressures and temperatures. *Science*, 251:1438–1443.

Labrosse, S. and Macouin, M. (2003). The inner core and the geodynamo. *C. R. Geosci.*, 335:37–50.

Lambeck, K. (1988). Geophysical geodesy. *Claredon Press, Oxford.*

Lassak, T. M., McNamara, A. K., and Zhong, S. (2007). Influence of thermochemical piles on topography at Earth's core-mantle boundary. *Earth Planet. Sci. Lett.*, 261:443–455.

Lay, T., Hernlund, J., and Buffett, B. A. (2008). Core-mantle boundary heat flow. *Nature Geoscience*, 1:25–32.

Lay, T., Hernlund, J., Garnero, E. J., and Thorne, M. S. (2006). A Post-Perovskite Lens and D" Heat Flux Beneath the Central Pacific. *Science*, 314:1272–1276.

Leahy, G. M. and Bercovici, D. (2007). On the dynamics of a hydrous melt layer above the transition zone. *J. Geophys. Res.*, 112:B07401.

Lei, J. and Zhao, D. (2006). A new insight into the Hawaiian plume. *Earth Planet. Sci. Lett.*, 241:438–453.

Li, C., Van der Hilst, R. D., Engdahl, E. R., and Burdick, S. (2008). A new global model for P wave speed variations in Earth's mantle. *Geochem. Geophys. Geosyst.*, 9(5):Q05018.

Li, H., Xu, L., and Liu, C. (2005). Temperature dependence of the first pressure derivative of the isothermal bulk modulus for solid materials at zero pressure: Application to MgO. *J. Geophys. Res.*, 110:B05203.

Lin, S. C. and van Keken, P. E. (2006). Dynamics of thermo-chemical plumes: 1. Plume formation and entrainment of a dense layer. *Geochem. Geophys. Geosyst.*, 7:Q02006.

Lyubetskaya, T. and Korenaga, J. (2007). Chemical composition of Earth's primitive mantle and its variance: 2. Implications for global geodynamics. *J. Geophys. Res.*, 112(B032152):doi:10.1029/2005JB004224.

Machetel, P. and Weber, P. (1991). Intermittent layered convection in a model mantle with an endothermic phase-change at 670 km. *Nature*, 350:55–57.

Mambole, A. and Fleitout, L. (2002). Petrological layering induced by an endothermic phase transition in the Earth's mantle. *Geophys. Res. Lett.*, 29(22):2044.

Mao, W. L., Mao, H., Sturhahn, W., Zhao, J. Prakapenka, V. B., Meng, Y., Shu, J., Fei, Y., and Hemley, R. J. (2006). Iron-Rich Post-Perovskite and the Origin of Ultralow-Velocity Zones. *Science*, 312:564–565.

Mao, W. L., Meng, Y., Shen, G. Y. Prakapenka, V. B., Campbell, A. J., Heinz, D. L., Shu, J. F., Caracas, R., Cohen, R. E., Fei, Y. W., and Hemley, R. J. amd Mao, H. K. (2005). Iron-rich silicates in the Earth's D" layer. *Proc. Nat. Acad. Sci. U.S.A.*, 102(28):9751–9753.

Mao, W. L., Shen, G., Prakapenka, V. B., Campbell, A. J., Heinz, D. L., Shu, J., Hemley, R., and Mao, H. (2004). Ferromagnesium postperovskite silicates in the D" layer. *Proc. Nat. Acad. Sci. U.S.A.*, 101(45):15867–15869.

Masters, G., Laske, G., Bolton, H., and Dziewonski, A. (2000). The relative behavior of shear velocity, bulk sound speed and compressional velocity in the mantle: Implications for chemical and thermal structure. *AGU Geophysical Monograph*, 117:63–87.

Matas, J., Bass, J., Ricard, Y., Mattern, E., and Bukowinski, M. S. T. (2007). On the bulk composition of the lower mantle: predictions and limitations from generalized inversion of radial seismic profiles. *Geophys. J. Int.*, 170:764–780.

Matsui, M., Katsura, T., Kuwata, A., Hagiya, K., Tomioka, N., Sugita, M., Yokoshi, S., Nozawa, A., and Funakoshi, K. (2006). Equation of state of $(Mg_{0.8},Fe_{0.2})_2SiO_4$ ringwoodite from synchotron X-ray diffraction up to 20 GPa and 1700 K. *Eur. J. Mineral.*, 18:523–528.

Mattern, E., Matas, J., Ricard, Y., and Bass, J. (2005). Lower mantle composition and temperature from mineral physics and thermodynamic modelling. *Geophys. J. Int.*, 160:973–990.

McCammon, C. A. (2001). Deep diamond mysteries. *Science*, 293:813–814.

McDonough, W. F. and Sun, S. (1995). The composition of the Earth. *Chem. Geol.*, 120(223-253).

McKenzie, D. (1977). Surface deformation, gravity anomalies and convection. *Geophys. J. R. Astron. Soc.*, 48(211-238).

McKenzie, D. and Bickle, M. J. (1988). The Volume and Composition of Melt Generated by Extension of the Lithosphere. *J. Petrol.*, 29(3):625–679.

Mégnin, C. and Romanowicz, B. (2000). The three-dimensional shear velocity structure of the mantle from the inversion of body, surface and higher-mode waveforms. *Geophys. J. Int.*, 143:709–728.

Morgan, W. J. (1965). Gravity Anomalies and Convection Currents. *J. Geophys. Res.*,

70(24):6175–6187.

Morgan, W. J. (1971). Convecting Plumes in the Lower Mantle. *Nature*, 230:42.

Murakami, M., Hirose, K., Kawamura, K., Sata, N., and Ohishi, Y. (2004). Post-perovskite phase transition in $MgSiO_3$. *Science*, 304:855–858.

Murthy, V. R., Van Westrenen, W., and Fei, Y. (2003). Experimental evidence that potassium is a substantial radiactive heat source in planetary cores. *Nature*, 423:163–165.

Nakagawa, T. and Buffett, B. A. (2005). Mass transport mechanism between the upper and lower mantle in numerical simulations of thermochemical mantle convection with multicomponent phase changes. *Earth Planet. Sci. Lett.*, 230(1-2):11–27.

Nakagawa, T. and Tackley, P. J. (2004a). Effects of a perovskite-post perovskite phase change near core-mantle boundary in compressible mantle convection. *Geophys. Res. Lett.*, 31:11–27.

Nakagawa, T. and Tackley, P. J. (2004b). Effects of thermo-chemical mantle convection on the thermal evolution of the Earth's core. *Earth Planet. Sci. Lett.*, 220:107–119.

Nakagawa, T. and Tackley, P. J. (2004c). Thermo-chemical structure in the mantle arising from a three-component convective system and implications for geochemistry. *Phys. Earth Planet. Int.*, 146:125–138.

Nakagawa, T. and Tackley, P. J. (2006). Three-dimensional structures and dynamics in the deep mantle: Effects of post-perovskite phase change and deep mantle layering. *Geophys. Res. Lett.*, 33(L12S11):1–4.

Nakagawa, T. and Tackley, P. J. (2008). Lateral variations in CMB heat flux and deep mantle seismic velocity caused by a thermal-chemical-phase boundary layer in 3-D spherical convection. *Earth Planet. Sci. Lett.*, 271:348–358.

Nakakuki, T., Sato, H., and Fujimoto, H. (1994). Interaction of the upwelling with the phase and chemical boundary at the 670 km discontinuity: Effects of temperature-dependent viscosity. *Earth Planet. Sci. Lett.*, 121:369–384.

Nataf, H. (2000). Seismic Imaging of Mantle Plumes. *Annu. Rev. Earth. Planet. Sci.*, 28:391–417.

Ni, S., Tan, E., Gurnis, M., and Helmberger, D. (2002). Sharp sides to the African Super Plume. *Science*, 296:1850–1852.

Nolet, G., Allen, R., and Zhao, D. (2007). Mantle plume tomography. *Chem. Geol.*, 241:248–263.

Nolet, G., Karato, S., and Montelli, R. (2006). Plume fluxes from seismic tomography. *Earth Planet. Sci. Lett.*, 248:685–699.

Oganov, A. R. and Ono, S. (2004). Theoretical and experimental evidence for a post-perovskite phase of $MgSiO_3$ in Earth's D"-layer. *Nature*, 430:445–448.

Ohta, K., Hirose, K., Lay, T., Sata, N., and Ohishi, Y. (2008). Phase transitions in pyrolite and MORB at lowermost mantle conditions: Implications for a MORB-rich pile above the core-mantle boundary. *Earth Planet. Sci. Lett.*, 267:107–117.

Olson, P. and Yuen, D. A. (1982). Thermochemical Plumes and Mantle Phase Transitions. *J. Geophys. Res.*, 87(B5):3993–4002.

O'Neill, C., Moresi, L., Torsvik, T. H., and Lee, C.-T. A. (2007). Episodic Precambrian subduction. *Earth Planet. Sci. Lett.*, 262:552–562.

O'Nions, R. K. and Oxburgh, E. R. (1983). Heat and Helium in the Earth. *Nature*, 306:429–430.

Ono, S., Ito, E., and Katsura, T. (2001). Mineralogy of subducted basaltic crust (MORB) from 25 to 37 GPa, and chemical heterogeneity of the lower mantle. *Earth Planet. Sci. Lett.*, 190:57–63.

Ono, S., Ohishi, Y., Isshiki, M., and Watanuki, T. (2005). In situ X-ray observations of phase assemblages in peridotite and basalt compositions at lower man-

tle conditions: Implications for density of subducted oceanic plate. *J. Geophys. Res.*, 110:B02208, doi:10.1029/2004JB003196.

Panasyuk, S. and Hager, B. (2000a). Inversion for mantle viscosity profiles constrained by dynamic topography and the geoid, and their estimated errors. *Geophys. J. Int.*, 143:821–836.

Panasyuk, S. and Hager, B. (2000b). Models of isostatic and dynamic topography, geoid anomalies, and their uncertainties. *J. Geophys. Res.*, 105(B12):28199–28209.

Perrillat, J., Ricolleau, A., Daniel, I., Fiquet, G., Mezouar, M., Guignot, N., and Cardon, H. (2006). Phase transformations of subducted basaltic crust in the upmost mantle. *Phys. Earth Planet. Int.*, 157:139–149.

Piazzoni, A. S., Steinle-Neumann, G., Bunge, H.-P., and Dolejš, D. (2007). A mineralogical model for density and elasticity of the Earth's mantle. *Geochem. Geophys. Geosyst.*, 8(11):Q110101.

Poirier, J. P., Malavergne, V., and Le Mouel, J. L. (1998). Is there a thin electrically conducting layer at the base of the mantle? *The Core-Mantle Boundary Region, AGU Monograph*, 28:131–137.

Pollack, H. N., Hurter, S. J., and Johnson, J. R. (1993). Heat flow from the Earth's interior: Analysis of the global data set. *Rev. Geophys.*, 31, 3:267–280.

Putirka, K. D., Perfit, M., Ryerson, F. J., and Jackson, M. G. (2007). Ambient and excess mantle temperatures, olivine thermometry, and active vs. passive upwelling. *Chem. Geol.*, 241:177–206.

Ranalli, G. (2001). Mantle rheology: radial and lateral viscosity variations inferred from microphysical creep laws. *J. Geodyn.*, 32(4-5):425–444.

Redkal, T. and Doornbos, D. J. (1992). The times and amplitudes of core phases for a variable core-mantle boundary layer . *Geophys. J. Int.*, 108(2):546–556.

Replumaz, A., Karáson, H., Van der Hilst, R. D., Besse, J., and Tapponnier, P. (2004). 4-d evolution of se asia's mantle from geological reconstructions and seismic tomography. *Earth Planet. Sci. Lett.*, 221:103–115.

Reymer, A. and Schubert, G. (1984). Phanerozoic addition rates to the continental crust and crustal growth. *Tectonics*, 3(1):63–77.

Ribe, N. M., Stutzmann, E., Ren, Y., and van der Hilst, R. (2007). Buckling instabilities of subducted lithosphere beneath the transition zone. *Earth Planet. Sci. Lett.*, 254:173–179.

Ricard, Y., Chambat, F., and Lithgow-Bertelloni, C. (2006). Gravity observations and 3D structure of the Earth. *C. R. Geosci.*, 338(14-15):992–1001.

Richards, M. A. and Hager, B. H. (1984). Geoid Anomalies in a Dynamic Earth. *J. Geophys. Res.*, 89(B7):5987–6002.

Ritsema, J. and Van Heijst, H.-J. (2000). Seismic imaging of structural heterogeneity in Earth's mantle: Evidence for large-scale mantle flow. *Science Progress*, 83:243–259.

Romanowicz, B. (2003). Global mantle tomography: Progress status in the past 10 years. *Annu. Rev. Earth. Planet. Sci.*, 31:303–328.

Romanowicz, B. and Gung, Y. (2002). Superplumes from the Core-Mantle Boundary to the Lithosphere: Implications for Heat Fluz. *Science*, 296:513–516.

Saltzer, R. L., Stutzmann, E., and Van der Hilst, R. D. (2004). Poisson's ratio in the lower mantle beneath Alaska: Evidence for compositional heterogeneity. *J. Geophys. Res.*, 109:B06301.

Saltzer, R. L., van der Hilst, R. D., and Karáson, H. (2001). Comparing P and S wave heterogeneity in the mantle. *Geophys. Res. Lett.*, 28(7):1335–1338.

Samuel, H. and Farnetani, C. G. (2003). Thermochemical convection and helium concentrations in mantle plumes. *Earth Planet. Sci. Lett.*, 207:39–56.

Sandiford, M. (2007). The tilting continent: A new constraint on the dynamic topographic field from Australia. *Earth Planet. Sci. Lett.*, 261(1-2):152–163.

Schilling, J. (1991). Fluxes and excess temperatures of mantle plumes inferred from their interaction with migrating mid-ocean ridges. *Nature*, 352:397–403.

Schmeling, H., Marquart, G., and Ruedas, T. (2003). Pressure- and temperature-dependent thermal expansivity and the effect on mantle convection and surface observables. *Geophys. J. Int.*, 154:224–229.

Segal, A. (1993). Finite element methods for advection-diffusion equations. In: Numerical Methods for Advection-Diffusion Problems. 45.

Segal, A. and Praagman, N. P. (2000). The SEPRAN package, Technical report. *http://ta.twi.tudelft.nl/sepran/sepran.html*.

Simmons, N. A., Forte, A. M., and Grand, S. P. (2007). Thermochemical structure and dynamics of the African superplume. *Geophys. Res. Lett.*, 34:L02301.

Sleep, N. H. and Fujita, K. (1997). Principles of Geophysics. *Blackwell Science*.

Smith, A. D. and Ludden, J. N. (1989). Nd isotopic evolution of the Precambrian. *Earth Planet. Sci. Lett.*, 93:14–22.

Solheim, L. P. and Peltier, W. R. (1993). Mantle phase transitions and layered convection. *Canadian Journal of Earth Sciences*, 30(5):881–892.

Solheim, L. P. and Peltier, W. R. (1994). Avalanche effects in phase transition modulated thermal convection: A model of Earth's mantle. *J. Geophys. Res.*, 99(B4):6997–7018.

Spengler, D., Van Roermund, L. M., Drury, M. R., Ottolini, L., Mason, P. R. D., and Davies, G. R. (2006). Deep origin and hot melting of an Archaean orogenic peridotie massif in Norway. *Nature*, 440:913–917.

Stacey, F. D. (1992). Physics of the Earth, Third edition. *Brookfield Press, Brisbane*.

Stacey, F. D. (2005). High pressure equations of state and planetary interiors. *Rep. Prog. Phys.*, 68:341–383.

Standish, J. J., Dick, H. J. B., Michael, P. J., Melson, W. G., and O'Hearn, T. (2008). MORB generation beneath the ultraslow spreading Southwest Indican Ridge (9-25^{o}F): Major element chemistry and the importance of process versus source. *Geochem. Geophys. Geosyst.*, 9(5):Q05004: doi:10.1029/2008GC001959.

Steinbach, V., Hansen, U., and Ebel, A. (1989). Compressible convection in the Earth's mantle: a comparison of different approaches. *Geophys. Res. Lett.*, 16(7):633–636.

Steinbach, V. and Yuen, D. A. (1994). Effects of depth-dependent properties on the thermal anomalies produced in flush instabilities from phase-transitions. *Phys. Earth Planet. Int.*, 86(1-3):185–203.

Steinbach, V. and Yuen, D. A. (1995). The effects of temperature-dependent viscosity on mantle convection with the two major phase transitions. *Phys. Earth Planet. Int.*, 90:13–36.

Steinbach, V., Yuen, D. A., and Zhao, W. (1993). Instabilities from phase transistions and the timescales of mantle thermal evolution. *Geophys. Res. Lett.*, 20(12):1119–1122.

Stixrude, L. and Lithgow-Bertelloni, C. (2007). Influence of phase transformations on lateral heterogeneity and dynamics in Earth's mantle. *Earth Planet. Sci. Lett.*, 263:45–55.

Su, W. and Dziewonski, A. M. (1997). Simultaneous inversion for 3-D variations in shear and bulk velocity in the mantle. *Phys. Earth Planet. Int.*, 100:135–156.

Sze, E. K. M. and van der Hilst, R. D. (2003). Core mantle boundary topography from short period PcP, PKP, and PKKP data. *Phys. Earth Planet. Int.*, 135:27–46.

Tackley, P. J. (1995). On the penetration of an endothermic phase transition by up-

wellings and downwellings. *J. Geophys. Res.-Solid Earth*, 100(B8):15477–15488.

Tackley, P. J. (1998). Three-Dimensional Simulations of Mantle Convection with a Thermo-Chemical Basal Boundary Layer: D"? In: Gurnis, M., M. E. Wysession, E. Knittle, and B. A. Buffett (Eds). *The Core-Mantle Boundary Region, AGU Monograph*, 28:231–253.

Tackley, P. J. (2002). Strong heterogeneity caused by deep mantle layering. *Geochem. Geophys. Geosyst.*, 3(4):10.1029/2001GC000167.

Tackley, P. J., Stevenson, D. J., Glatzmaier, G. A., and Schubert, G. (1993). Effects of an endothermic phase transition at 670 km depth in a spherical model of convection in the Earth's mantle. *Nature*, 361:699–704.

Tan, E. and Gurnis, M. (2007). Compressible thermochemical convection and application to lower mantle structures. *J. Geophys. Res.*, 112:B06304.

Ten, A., Yuen, D. A., Podladchikov, Y. Y., Larsen, T. B., Pachepsky, E., and Malevsky, A. V. (1997). Fractal features in mixing of non-Newtonian and Newtonian mantle convection. *Earth Planet. Sci. Lett.*, 146:401–414.

Thoraval, C., Machetel, P., and Cazenave, A. (1995). Locally layered convection from dynamic models of the Earth's mantle . *Nature*, 375:777–780.

Tolstikhin, I. N. and Hofmann, A. W. (2005). Early crust on top of the Earth's core. *Phys. Earth Planet. Int.*, 148:109–130.

Tolstikhin, I. N., Kramers, J. D., and Hofmann, A. W. (2006). A chemical Earth model with whole mantle convection: The importance of a core-mantle boundary layer (D") and its early formation. *Chem. Geol.*, 226:79–99.

Torsvik, T. H., Smethurst, M. A., Burke, K., and Steinberger, B. (2006). Large igneous provinces generated from the margins of the large low-velocity provinces in the deep mantle. *Geophys. J. Int.*, 167:1447–1460.

Trampert, J., Deschamps, F., Resovsky, J., and Yuen, D. (2004). Probabilistic tomography maps chemical heterogeneities throughout the lower mantle. *Science*, 306:853–856.

Trampert, J., Vacher, P., and Vlaar, N. (2001). Sensitivities of seismic velocities to temperature, pressure and composition in the lower mantle. *Phys. Earth Planet. Int.*, 124:255–267.

Trampert, J. and van der Hilst, R. D. (2005). Towards a quantitative interpretation of global seismic tomography. In: Van der Hilst R.D., Bass, J., Trampert, J. (Eds). *Earth's Deep Mantle: Structure, Composition, and Evolution, AGU Geophysical Monograph*, 160:47–62.

Turcotte, D. L. and Schubert, G. (2002). Mantle Dynamics. *Cambridge University Press*.

Van den Berg, A. P., Rainey, E. S. G., and Yuen, D. A. (2005). The combined influences of variable thermal conductivity, temperature- and pressure-dependent viscosity and core-mantle coupling on thermal evolution. *Phys. Earth Planet. Int.*, 149:259–278.

Van den Berg, A. P., Van Keken, P. E., and Yuen, D. A. (1993). The effects of a composite non-newtonian and newtonian rheology on mantle convection. *Geophys. J. Int.*, 115:62–78.

Van den Berg, A. P. and Yuen, D. A. (1996). Is the Lower-Mantle Rheology Newtonian Today? *Geophys. Res. Lett.*, 23(16):2033–2036.

Van der Hilst, R., Engdahl, R., Spakman, W., and Nolet, G. (1991). Tomographic imaging of subducted lithosphere below Pacific island arcs. *Nature*, 353:37–43.

Van der Hilst, R. D., De Hoop, M. V., Wang, P. Shim, S.-H., Tenorio, L., and Ma, P. (2007). Seismo-stratigraphy and thermal structure of Earth's core-mantle boundary region. *Science*, 315:1813–1817.

Van der Hilst, R. D. and Kárason, K. (1999). Compositional heterogeneity in the bottom 1000 kilometers of the Earth's mantle: Toward a Hybrid Convection Model. *Science*, 283:1885–1888.

Van der Hilst, R. D. and Seno, T. (1993). Effects of relative plate motion on the deep structure and penetration depth of slabs below the Izu-Bonin and Mariana island arcs. *Earth Planet. Sci. Lett.*, 120:375–407.

Van der Hilst, R. D., Widiyantoro, S., and Engdahl, E. R. (1997). Evidence for deep mantle circulation from global tomography. *Nature*, 386:578–584.

Van Keken, P. (2001). Cylindrical scaling for dynamical cooling models of the Earth. *Phys. Earth Planet. Int.*, 124:119–130.

Van Keken, P. E., Karato, S., and Yuen, D. A. (1996). Rheological control of oceanic crust separation in the transition zone. *Geophys. Res. Lett.*, 23(14):1821–1824.

Van Keken, P. E., King, S. D., Schmeling, H., Christensen, U. R., Neumeister, D., and Doin, M. P. (1997). A comparison of methods for the modeling of thermochemical convection. *J. Geophys. Res.*, 102(B10):22,477–22,495.

Van Summeren, J. R. G., Van den Berg, A. P., and Van der Hilst, R. D. (2008). Upwellings from a deep mantle reservoir filtered at the 660 km phase transition in thermo-chemical convection models and implications for intra-plate volcanism. *Phys. Earth Planet. Int.*, (doi:10.1016/j.pepi.2008.09.011).

Van Thienen, P., Van den Berg, A. P., and Vlaar, N. J. (2004). Production and recycling of oceanic crust in the early Earth. *Tectonophysics*, 386:41–65.

Van Thienen, P., Van Summeren, J., Van der Hilst, R. D., Van den Berg, A. P., and Vlaar, N. J. (2005). Numerical study of the origin and stability of chemically distinct reservoirs deep in Earth's mantle. In: Van der Hilst R.D., Bass, J., Trampert, J. (Eds). *Earth's Deep Mantle: Structure, Composition, and Evolution, AGU Geophysical Monograph*, 160:117–136.

Vinnik, L. and Farra, V. (2007). Low S velocity atop the 410-km discontinuity and mantle plumes. *Earth Planet. Sci. Lett.*, 262:398–412.

Vlaar, N. J., Van Keken, P. E., and Van den Berg, A. P. (1994). Cooling of the Earth in the Archaean: Consequences of pressure-release melting in a hotter mantle. *Earth Planet. Sci. Lett.*, 121:1–18.

Vreugdenhil, C. B. and Koren, B. (1993). Numerical Methods for Advection - Diffusion Problems. *Notes on Numerical Fluid Mechanics*, 45.

Walter, M. J., Nakamura, E., Tronnes, R. G., and Frost, D. J. (2004). Experimental constraints on crystallization differentiation in a deep mantle ocean. *Geochim. et Cosmochim. Acta*, 68(20):4267–4284.

Wang, Y., Weidner, D. J., Liebermann, R. C., and Zhao, Y. (1994). P-V-T equation of state of (Mg,Fe)SiO_3 perovskite: constraints on composition of the lower mantle. *Phys. Earth Planet. Int.*, 83(1):13–40.

Wang, Y., Wen, L., and Weidner, D. (2008). Upper mantle SH- and P-velocity structures and composition models beneath southern Africa. *Earth Planet. Sci. Lett.*, 267:596–608.

Wang, Y., Wen, L., Weidner, D. J., and He, Y. (2006). SH velocity and compositional models near the 660-km discontuity beneath South America and northeast Asia. *J. Geophys. Res.*, 111:B07305.

Weidner, D. J. and Wang, Y. (1998). Chemical- and Clapeyron-induced buoyancy at the 660 km discontinuity. *J. Geophys. Res.*, 103(B4):7431–7441.

Weinstein, S. A. (1992). Induced compositional layering in a convecting fluid layer by an endothermic phase transition. *Earth Planet. Sci. Lett.*, 113(1-2):23–39.

Wen, L. and Anderson, D. L. (1997). Layered mantle convection: A model for geoid

and topography. *Earth Planet. Sci. Lett.*, 146:367–377.

Wheeler, P. and White, N. (2000). Quest for dynamic topography: Observations from Southeast Asia. *Geology*, 28(11):963–966.

Williams, Q. and Knittle, E. (2005). The Uncertain Major Element Bulk Composition of Earth's Mantle. In: Van der Hilst R. D., Bass, J., Trampert, J. (Eds). *Earth's Deep Mantle: Structure, Composition, and Evolution, AGU Geophysical Monograph*, 160:165–186.

Wilson, J. T. (1966). Did the Atlantic close and then Re-open? *Nature*, 211:676.

Xie, S. and Tackley, P. J. (2004a). Evolution of helium and argon isotopes in a convecting mantle. *Phys. Earth Planet. Int.*, 146(3-4):417–439.

Xie, S. and Tackley, P. J. (2004b). Evolution of U-Pb and Sm-Nd systems in numerical models of mantle convection and plate tectonics. *J. Geophys. Res.*, 109(B11204).

Yoshida, M. (2004). Possible effects of lateral viscosity variations induced by plate-tectonic mechanism on geoid inferred from numerical models of mantle convection. *Phys. Earth Planet. Int.*, 147:67–85.

Zebib, A., Schubert, G., Dein, J., and Paliwal, R. C. (1983). Character and stability of axisymmetric thermal convection in spheres and spherical shells. *Geophys. Astrophys. Fluid Dyn.*, 23:1–42.

Zhao, D. (2007). Seismic images under 60 hotspots: Search for mantle plumes. *Gondwana Research*, 12:335–355.

Zhong, S. (2006). Constraints on thermochemical convection of the mantle from plume heat flux, plume excess temperature, and upper mantle temperature. *J. Geophys. Res.*, 111:B04409.

Acknowledgments

Looking back on my PhD project I see a period with of course plenty of tough challenges and winding roads but also many exciting moments and satisfactory achievements. Altogether, I consider it a very pleasant and rewarding period. Here I would like to thank the people that helped to make this possible.

My promotor Rob van der Hilst made it possible to indulge in a scientifically very interesting project. Your comments were always to the point and helped me to focus my research and tackle problems with the right frame of mind. I appreciate the time you devoted to my manuscripts that were sometimes 'tough reads' or sent rather close to ultimate deadlines. My writing skills definitively benefited from your corrections.

A lot of thanks I owe to my co-promotor and daily supervisor Arie van den Berg. The word 'daily' can be taken literally here: your interest and enthousiasm for my work and your time and energy committed are very much appreciated. In-depth scientific discussions helped to make this thesis more substantial and 'consistent'. At times when I felt somewhat lost or undecisive, your advises often helped with finding back the right direction.

For careful proofreading of my thesis I wish to acknowledge the members of the dissertation committee: Dr. Hana Čížková, Prof. dr. Wim Spakman, Prof. dr. Jeannot Trampert, Dr. Wim van Westrenen, and Prof. dr. Dave Yuen.

Thorough and constructive reviews from Takashi Nakagawa (Kyushu University), Teresa Lassak (Arizona State University) and an anonymous reviewer greatly helped to improve Chapter 3. Discussions on seismology with Jeannot Trampert and Jeroen Tromp (Princeton University) improved Chapter 5. I also thank Jeannot Trampert for providing seismic sensitivity data, and Brian Kennett (Australian National University) for making available his bulk sound velocity model. My knowlegde on petrology and mineral physics definitely improved by inspiring discussions with Wim van Westrenen (Vrije Universiteit), Michel Jacobs (Clausthal University), Martyn Drury, and many others. I am grateful to the geophysics group of Charles University for multiple pleasant visits to Prague and useful discussions on gravity and mantle dynamics. In particular, I wish to thank Hana Čížková, Ctirad Matyska, and Ondřej Čadek. I also appreciated to be witness of several Rostoky Mountain events.

Jacqueline Landsheer, Ildiko Csikos, and Margreet Evertman are thanked for their

careful help with administrative matters. Joop Hoofd and Theo van Zessen efficiently solved many computer-related issues. Computational resources for this work were provided by the Netherlands Research Center for Integrated Solid Earth Science (ISES 3.2.5 High End Scientific Computation Resources).

During the past years, I remember lively conversations with my collegues on science, as well as on how to survive in academia, the counting rules of the tie-break, or who should pay the next round. For this I thank Roberta, Céline, Bahjat, Pasha, Peter, Jellie, Jeroen, Ali, Steven, Karin, Maisha, Marzieh, Gabriela, Rob, Rinus, and Wim. Thomas, thanks for being a pleasant roommate during a large part of my project. Thanks goes out also to Stefan, Ueli, Ebru, Ilaria, Frédéric, Robbert, Sergei, Mei, Wouter, Karin, Hanneke, Arie, Paul, Manfred, Kabir, Simona, Mariène, Ruud, Siska, Laurie, Xavier, Bart, Dirk, Côme, Auke, and Maurits.

Friends that I want to thank are Rory, Christa, Iris, Gerben, Pieter, Eefje, Thijs, Linda, and Sebastiaan for many fun evenings, concert visiting and skiing (or something close to it). Peter and Frank, thanks for staying in touch and reminding me of my southern roots.

A last word in Dutch is reserved for my family. Tenslotte wil ik mijn familie bedanken voor hun onvoorwaardelijke steun. Lieve, Teun, en Pip, bedankt voor jullie rücksichtlose wake-up calls in de vroege ochtend: ze hebben me serieus geholpen om ook door de week wat eerder op te staan en voor tien uur op de faculteit te verschijnen. Erik en Annemiek, Roel en Nicole, en bovenal mijn ouders, bedankt voor de vele leuke dagen, maar ook voor jullie hulp en inzichten gedurende dit project en lang daarvoor.

Figure 6.1: ”Pouring milk in tea: Modelling 4.5 billion years of mantle evolution in 45 seconds.” Photography by S. Valcke.

Curriculum Vitae

2004-2008	**PhD student in Theoretical Geophysics/Mantle Dynamics** Utrecht University The Netherlands
2003	**Teacher Secondary School Institute** Studiekring Utrecht, The Netherlands
2001	**Research Trainee Geothermal Energy Team** Shell International Exploration and Production Rijswijk, The Netherlands
1996-2003	**Study of Geophysics** Utrecht University The Netherlands
1990-1996	**Pre-university Education** Titus Brandsma Lyceum Oss, The Netherlands